Taylor, B., Huchon, P., Klaus, A., et al., 1999
Proceedings of the Ocean Drilling Program, Initial Reports Volume 180

10. SITE 1116[1]

Shipboard Scientific Party[2]

SITE 1116

Hole 1116A (RCB):
9°51.934′S, 151°34.508′E; 1851.3 mbsl
0–158.90 mbsf cored; 32.61 m recovered (21%)

Site 1116 is on the southern flank of Moresby Seamount, 8 km south of Site 1114, within a tilted block bounded by two normal faults that each offset the basement by >1 km to the south-southwest. The objectives for this site were to characterize the early rift sediments and the seamount basement (which was not reached).

Very low surface porosity (~30%), and high bulk density (~2.15 g·cm^{-3}), sonic velocity (2.2–2.8 km·s^{-1}), and thermal conductivity (1.0–2.2 W·m^{-1}·°C^{-1}) values, suggest that 700–1000 m of the section has been removed by faulting and/or erosion. This is consistent with the lack of a Quaternary and uppermost Pliocene section, as well as the seismic stratigraphy.

The recovered section is dominated by Pliocene indurated sandstones alternating with siltstones/claystones. The sandstones are fine to medium, and occasionally coarse grained, and display parallel, wavy, and convolute laminations, which indicate they originated from turbidity currents in a near-source slope setting. A paraconglomerate is present at 34–63 mbsf. The sandstones below this are subarkosic with a calcareous matrix. Measured $CaCO_3$ contents are <5 wt%. Some thick-bedded, reverse-graded sandstones with occasional intraformational rip-up clasts were deposited from high-density turbidity currents. However, normal grading and lamination in some siltstones/sandstones also indicate deposition by low-concentration turbidity or bottom currents. The matrix-supported conglomerates, interbedded with sandstones and siltstones, comprise relatively unaltered, mainly angular clasts and are interpreted as debris-flow deposits.

[1]Examples of how to reference the whole or part of this volume.
[2]Shipboard Scientific Party addresses.

Ms 180IR-110

Benthic foraminifers indicate middle bathyal paleowater depths (500–2000 m), with inner neritic (<50 m) benthic foraminifers redeposited within turbidite beds. The N20/N21 boundary (3.35 Ma) occurs between 104 and 128 mbsf, and the minimum age of 1.95 Ma at the surface yields a minimum sedimentation rate of 70 m/m.y. Burrows are either abundant or relatively depleted, suggesting alternating poorly and well-oxygenated subseafloor conditions with, in both cases, abundant detrital organic matter input and a mostly terrigenous source, as indicated by C/N ratios.

The orientations of the subhorizontal maximum axes of the ellipsoids of magnetic susceptibility (corrected for bedding dip and core orientation) below 100 mbsf indicate northeast-southwest or northwest-southeast–directed paleocurrents during sedimentation.

The sources of clastics are little-altered basic extrusive rocks of mainly calc-alkaline affinities, probably derived from the Miocene Trobriand Arc, but also include acidic extrusives, shallow-water bioclasts, metamorphics, and serpentinite. The serpentinite, rare chromite, and some of the gabbro and dolerite grains probably have an ophiolitic origin (Paleocene–Eocene Papuan Ultramafic Belt?).

The upper 100 m of the section shows abundant evidence of synsedimentary deformations, including folding and low-angle extensional faulting typical of gravity-driven processes. The bedding dips <10°, except for fold limbs where it is up to 50°. Common dewatering and fluidization features were possibly seismically triggered. Faults and scaly fabrics are within a narrow zone between 100 and 120 mbsf. They include steep strike-slip and 25°- to 55°-dipping pure normal faults. Below the fault zone beds dip ~15° consistent with the dip of seismic reflectors.

OPERATIONS

Transit to Site 1116 (ACE-16A)

During the transit to Site 1116, the drill crew prepared the rotary core barrel (RCB) coring and bottom hole assembly (BHA) with a new C-4 core bit and mechanical bit release (MBR). At 0330 hr on 23 July 1998, the seafloor positioning beacon was deployed, beginning Hole 1116A.

Hole 1116A

After lowering the BHA to 1819.0 meters below sea level (mbsl) and picking up the top drive in preparation for spudding, the driller began the normal process of slowly circulating seawater ("slow circulating rates," [SCR]) to establish baseline rig floor pressures for various flow rates before spudding. The pump pressure immediately rose to 600 psi (at 40 strokes per minute [spm]). Because this was abnormally high, the sinker bars were run in the hole to recover the core barrel. There was no sign of any sediment nor were any mechanical problems noted with the core barrel or its retrieval. Another core barrel was pumped to bottom, and the driller started circulating the seawater. This time the pump pressure rose immediately to 1400 psi and continued to climb until the driller shut down the pumps. It appeared that all of the bit nozzles were completely plugged. We decided not to make any more attempts to clear the blockage because in this relatively shallow water it would not take too long to retrieve the BHA to physically investigate the problem.

The bit reached the rig floor after a 4.5 hr pipe trip and a thorough inspection of all the BHA components failed to identify any mechanical problem or blockage. The bit, bit jets, support bearing, float valve, MBR, and core barrel latch sleeve were all found to be unobstructed and in normal condition. Furthermore, there were no indications that any of these components had been below the seafloor or that the drillers had seen any reduction in drill string weight to indicate that the bit had contacted the seafloor during the pipe trip.

While the drill crew were reassembling the original core barrel components for a rig floor flow test, the coring technician inspected another bit release assembly that was being rebuilt in the core technicians shop. The technician noticed that when the lower support bearing was installed in the pocket of the bit disconnect there appeared to be no flow path remaining for the circulating fluid. Upon checking the machine drawing of the bit disconnect, it became apparent that this component had a manufacturing flaw. A 60° taper at the base of the pocket was missing, which prevented nearly all of the flow around the bearing. The only flow area remaining was between the inside diameter of the support bearing and the outside diameter of the core barrel landing sub. The difference in pump pressure between the first and second core barrel deployed may have resulted from different amount of wear on the respective landing subs, which resulted in a more or less internal flow area.

The rig crew reassembled the original outer core barrel components. When the circulating pumps were activated, the pump pressure was significantly higher than normal (600 psi at 15 spm). This confirmed that a mechanical blockage was somewhere in the coring assembly. Upon removing the suspect MBR for the second time, it too was missing the critical taper. After installing a new MBR with the correct taper, a rig floor flow test indicated normal pump pressures. The rest of the BHA was prepared and lowered to the seafloor.

Hole 1116A was spudded at 1915 hr on 23 July and based on a reduction in drill string weight, seafloor depth was determined to be 1851.3 mbsl (Table T1). Because of the indurated nature of the seafloor sediments, the first few cores progressed slowly. After a few drill collars were buried beneath the seafloor, the drillers were able to increase the weight on bit (WOB) and the top drive rpm. The first 48 meters below seafloor (mbsf) cut at an average rate of 2.5 m/hr with 5000–10,000 lb WOB and 40–50 rpm. Cores 1R through 18R were taken from 0 to 158.9 mbsf. Core recovery in Hole 1116A was generally poor, ranging from 2% to 33% (average 21%) and the overall penetration rate was 3.8 m/hr (Table T2).

T1. Site 1116 coring summary, p. 64.

T2. Site 1116 coring summary by section, p. 65.

When the drill string was being raised after cutting Core 18R (0215 hr on 26 July), the drill string started experiencing torque. The driller continued to raise the drill string up to 153.0 mbsf where rotation was lost and the pipe became stuck. For the next 1.75 hr, the driller attempted to free the drill string. He was able to maintain circulation in the hole, but could not rotate or raise/lower the pipe. Initial attempts to actuate the drilling jars were unsuccessful, leading the drill crew to believe that the drill string may have been stuck above the jars. Overpulls of up to 200,000 lb were unable to free the drill string.

After recovering Core 18R, we resumed efforts to free the drill string. At 0600 hr, after working the pipe for another 1.25 hr, the drilling jars were successfully actuated with ~40,000 lb of overpull. Drill string rotation and vertical movement were immediately re-established; however, pump pressures remained slightly higher than normal.

A short wiper trip of the hole was made up to 91.0 mbsf and all drilling parameters returned to normal. At 0630 hr on 26 July, a core barrel was deployed, and the driller prepared to run it back to bottom to resume coring. When pump pressures did not rise as normally happens when the core barrel has landed, the driller began to suspect that the bit may have released during the efforts to free the drill string. Another explanation is that a drill string component may have been bent and was keeping the core barrel from landing properly. The sinker bars were run in the hole to determine if the core barrel had landed properly, but the sinker bars passed below the depth where the top of the core barrel should have been and then passed even slightly below where the bit should have been. This confirmed that the bit had indeed released; therefore, we retrieved the drill string and abandoned the hole. The positioning beacon was recovered at 1030 hr and the pipe trip was completed at 1100 hr ending Hole 1116A.

At the rig floor the MBR was inspected. It was determined that the release sleeve had not shifted and the latch segments ("dogs") remained in place. Brinelling (deformation of metal) on the upper surface of the segments, indicated that the bit disconnect portion of the MBR had failed and been stripped over the latch segments. It is not clear whether the bit disconnect mechanically failed because of the jarring action or the overpull used in freeing the drill string. It is speculated that the bit was stuck in the hole and that the overpull had weakened or cracked the bit disconnect above the latch dog windows. Subsequent jarring with the mechanical drilling jars likely caused the disconnect to fail completely and release the bit, thereby freeing the drill string.

LITHOSTRATIGRAPHY

The succession cored at Site 1116 recovered mainly clastic sediments and sedimentary rocks, comprising an inferred Pliocene rift succession. The recovery was very poor (21%) and downhole logs were not available. Three lithostratigraphic units are recognized on the basis of sediment or rock type, grain size, sedimentary structures, color, smear slides, thin sections, bulk mineralogy (X-ray diffraction [XRD]), and carbonate content (Fig. F1).

F1. Lithologic log of succession at Site 1116, p. 22.

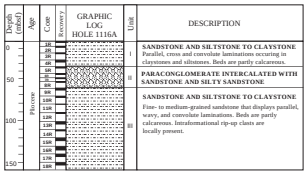

Lithostratigraphic Unit I

Description: sandstone and siltstone to claystone
Interval: Cores 180-1116A-1R through 4R
Depth: 0.0–33.8 mbsf
Age: Pliocene

Lithostratigraphic Unit I comprises two parts: (1) a number of isolated clasts of sedimentary rocks of different composition recovered in Core 1R and Section 2R-1; and (2) more coherent intervals of mainly sandstones recovered in Section 2R-CC through Core 4R. The nature of the clasts is summarized first to allow comparison with the more intact intervals beneath.

The following lithologies were recovered as clasts: gray and grayish brown claystone, silty claystone, sandy siltstone, coarse-grained sandstone (with common red grains), and coarse- to very coarse-grained sandstone. The sandstone is well sorted with a calcite cement. Many of the sandstones and siltstones are strongly bioturbated (with *Chondrites*

burrows) obscuring sedimentary structures. Calcite veining is rarely observed. Disseminated organic matter is locally visible in the sandstone and siltstone. Some of the siltstones contain planktonic foraminifers and bioclasts occur in some sandstones.

In addition, the following sedimentary structures were observed within the clasts: inclined lamination, parallel lamination, cross lamination, or convolute lamination of siltstone, and sharp lower and upper bed contacts in siltstone.

Petrographic examination of the sandstones (see Figs. F2, F3, F4, F5; "Site 1116 Thin Sections") show that typically, the grains are angular to subangular, but a small proportion is subrounded to well rounded. Sandstone contains abundant fresh basalt (locally glassy), chloritized basalt, acidic volcanics (with quartz and feldspar phenocrysts), rare dolerite (with pyroxene and plagioclase), and acidic volcanics with brown hornblende phenocrysts. Mineral grains are plagioclase (commonly zoned), biotite, pyroxene, and rare hornblende. Lithic fragments include commonly polycrystalline quartz, calc-schist (with some well-rounded grains), biotite schist, rounded serpentinite grains, and micritic clasts. In addition, bioclasts include bivalve shell fragments and benthic foraminifers. The sandstone typically has a sparry calcite cement. A thin section showed the siltstone to be well sorted with abundant quartz, feldspar, biotite, opaque mineral grains, pyrite, chloritized basalt, planktonic foraminifers, rare muscovite, and chlorite (green and blue types), set in a silty matrix.

In addition, the following lithologies were recovered in the more coherent sedimentary intervals.

Sandstone/Siltstone

Well-sorted, well-cemented sandstone/siltstone is present as normal-graded couplets with sharp bases and graded tops (interval 180-1116A-4R-2, 4–9 cm; Fig. F6). The sandstones are mainly greenish gray to gray, but are locally dusky red in color (Section 4R-CC). Thin sections revealed a composition very similar to that from the clasts described above, including a range of basic and acidic volcanic rocks, together with shallow-water derived bioclasts and fine-grained metamorphic rock (see "Site 1116 Thin Sections").

Siltstone and very fine sandstone is ripple laminated (interval 180-1116A-2R-CC, 4–7 cm), parallel or wavy laminated (e.g., intervals 180-1116A-2R-CC, 7–9 cm; 2R-CC, 13–16 cm; and 4R-1, 10–13 cm) in layers each ~0.5 m thick. Exceptionally, fine-grained silt has an irregular base and appears to be loaded into underlying coarse-grained siltstone. In addition, a synsedimentary injection dike of medium-grained sandstone is present in Section 4R-2.

Silty Claystone

This facies is burrowed, with sharp upper and lower bed contacts (e.g., interval 180-1116A-2R-CC, 0–4 cm), and commonly contains disseminated organic matter (see Fig. F7). The XRD of fine-grained sediment indicates the presence of quartz and plagioclase as major constituents, and calcite, chlorite, smectite, amphibole, and pyroxene as minor constituents (see Table T3). Calcium carbonate values range from 1.9–4.8 wt% (see "$CaCO_3$, Sulfur, Organic Carbon, and Nitrogen," p. 17).

F2. Basaltic clast with plagioclase laths in glassy matrix, p. 23.

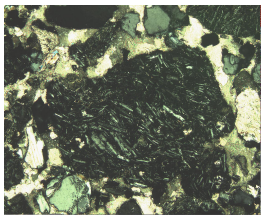

F3. Acidic volcanic clast with feldspar phenocrysts, p. 24.

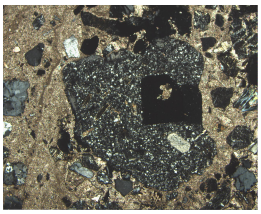

F4. Grain of serpentinite with adjacent acidic and basic grains, p. 25.

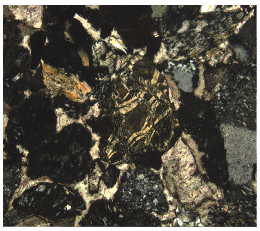

F5. Plutonic rock with intergrown quartz, feldspar, and biotite, p. 26.

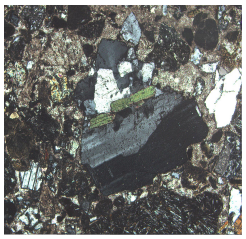

F6. Graded laminae of siltstone and sandstone offset by faults, p. 27.

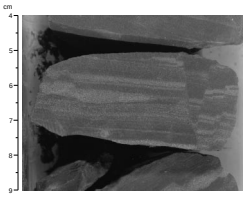

In addition, a dewatering structure was observed in which a subvertical conduit is infilled with medium-grained sandstone (Fig. F8).

Interpretation

Two possible origins of the clasts in the upper part of Unit I can be considered: (1) it is possible that the clasts were entirely created by drilling disturbance, compounded by the difficulty of spudding into a relatively lithified seafloor; and (2) the clasts could represent gravitational talus. The site is located on the southern flank of Moresby Seamount in an area where seafloor is locally steeply sloping. It is, therefore, possible that the isolated clasts represent talus that was shed down steep slopes on the side of the seamount. However, in either case, because no exotic lithologies (e.g., igneous or metamorphic) are present, both the clasts and intact intervals are correlated as originally parts of essentially the same succession. Around 30 mbsf (Core 4R) the succession is deformed; fault planes cut cleanly across the sedimentary succession, indicating that the faulting postdates consolidation (see "Domain II," p. 12).

Taken together, the clasts and more intact intervals are interpreted to represent a succession of sandstone, siltstone, and claystone. The presence of normal grading and other structures, including more small-scale cross lamination, suggests that the clastic sedimentary rocks accumulated from low-concentration turbidity currents, the tail of high-concentration turbidity currents, or bottom currents. Similar structures, including small-scale cross lamination, are better developed in Unit III and are discussed more fully under that heading. Dewatering structures are also discussed in that section (see "Lithostratigraphic Unit III," p. 8). The paucity of bioturbation and subdued color suggests that subseafloor conditions were relatively depleted in oxygen (i.e., suboxic). On the other hand, some more strongly burrowed intervals were presumably well oxygenated. Water depths were estimated to be from 500 to 2000 m (see "Benthic Foraminifers," p. 15).

The petrographic evidence indicates that the main source was relatively unaltered basic volcanic rocks, plus acidic volcanics, coupled with a contribution from metamorphic lithologies and serpentinite. The textural maturity of some clasts, and the presence of shallow-water bioclasts, suggest that some of the material was derived from a shallow-water setting before being redeposited by turbidity currents or debris flows into a deep-water setting undergoing hemipelagic accumulation.

Lithostratigraphic Unit II

Description: paraconglomerate intercalated with sandstone and siltstone
Interval: Cores 180-1116A-5R through 8R
Depth: 33.8–62.6 mbsf
Age: Pliocene

Lithostratigraphic Unit II is distinguished by the occurrence of paraconglomerate associated with sandstone and siltstone. The following lithologies are present:

Paraconglomerate

Conglomerate was recovered in two forms: (1) occasional intact pieces ranging in size from 5 to 15 cm (e.g., Fig. F9). This conglomerate

F7. Strongly bioturbated silty claystone, p. 28.

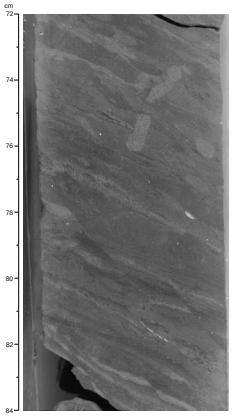

T3. XRD analysis of sediments, Site 1116, p. 67.

F8. Clayey siltstone with fluid injection structure, p. 29.

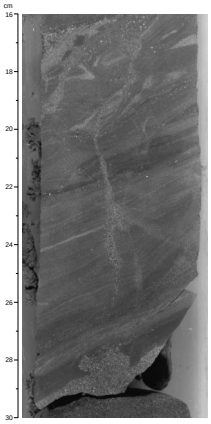

F9. Poorly sorted, matrix-supported paraconglomerate, p. 30.

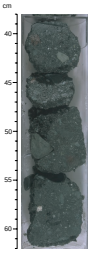

is matrix supported and is composed of subangular to subrounded clasts (mostly >1.5 cm in size) of mainly volcanic rocks. The matrix is poorly sorted clayey silty sandstone; and (2) mainly isolated pebbles and cobbles (e.g., Core 5R). The clasts recovered without matrix tend to be more rounded than those with matrix. From core observations, these clasts include red altered basalt, vesicular aphyric basalt, aphyric basalt with green alteration (chlorite?), amygdaloidal basalt (calcite and quartz), feldspar phyric basalt, andesite?, dolerite, and porphyritic acidic volcanic rock. Vesicles and vugs in one basalt clast are infilled with pyrite.

A small number of the igneous clasts were studied in thin section (see "Site 1116 Thin Sections"). These are generally little altered and mainly comprise several different types of basic extrusive rock as follows: (1) basic volcanic with phenocrysts of plagioclase, microphenocrysts of yellowish green amphibole in a flow-textured groundmass of feldspar laths and glass (Fig. F10); (2) basic volcanic with large phenocrysts of plagioclase and microphenocrysts of augite set in a flow-textured groundmass, including plagioclase laths (Fig. F11); (3) basic volcanic with large brown hornblende phenocrysts, plagioclase, and augite in a flow-textured groundmass; (4) mafic volcanic with altered plagioclase and chlorite; and (5) mafic cumulate, with fresh and altered pyroxene.

F10. Basic volcanic rock with hornblende phenocrysts, p. 31.

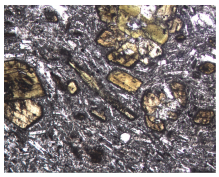

F11. Basic volcanic rock with various phenocrysts, p. 32.

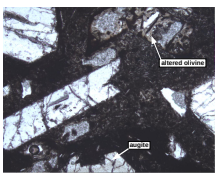

F12. Clast of glassy basalt with phenocrysts in a silty matrix, p. 33.

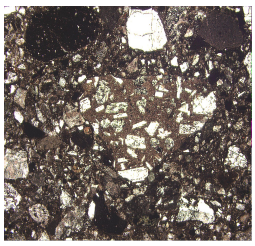

F13. Porphyritic basalt clast with glassy matrix and phenocrysts, p. 34.

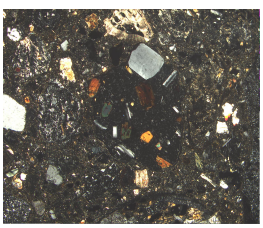

Sandstone and Siltstone

Some intact sandstone beds are relatively well sorted, have sharp bases and tops and include sand-filled burrows (e.g., interval 180-1116A-5R-1, 108–130 cm). Rare foraminifers are present. Carbonaceous detritus and red altered grains of volcanic rock are very common. In addition, poorly sorted silty sandstone is found adhering to some of the individual clasts. Siltstone was recovered partly as isolated fragments in which it is interlaminated with fine-grained sandstone. XRD analysis of fine-grained sediment indicated the presence of quartz, plagioclase, chlorite, smectite?, calcite, and pyroxene (Table T3).

In addition, data from two thin sections of sandstones document a very poorly sorted texture (see Figs. F10, F12; also "Site 1116 Thin Sections"). Despite this, many grains are subrounded to rounded, especially the basic volcanic grains (Fig. F13). The sandstone contains abundant fresh basalt (locally glassy), chloritized basalt, variolitic basalt, palagonite, acidic volcanics, and plutonic rocks (dolerite and gabbro). Mineral grains are plagioclase (commonly zoned), biotite, pyroxene, and rare hornblende. Lithic fragments are polycrystalline quartz and schist (including chloritic schist). Pyrite is common. In addition, bioclasts include echinoderm plates and both benthic and planktonic foraminifers. The sandstone has a poorly sorted silty matrix.

Interpretation

The paraconglomerates are interpreted as debris-flow deposits, based on the presence of the poorly sorted silty matrix, matrix support, and the relatively angular shape of some of the clasts. The minimal recovery of pebbles and granules in some intervals (e.g., Section 6R-CC) probably represents remnants of thick beds of paraconglomerate of which only a few pebbles and cobbles were recovered. The paraconglomerate was originally interbedded with sandstone and siltstone. Clasts of laminated siltstone are interpreted as fragments of originally coherent beds

created by drilling rather than as primary clasts. The associated silty sandstone and minor siltstone are thus interpreted as original interbeds deposited by turbidity currents, based on the sharp bases of beds and normal grading. They might represent either discrete interbeds of low-density turbidity currents or the upper parts of high-density turbidity currents.

In addition, much of Unit II is represented by isolated well-rounded pebbles and granules of igneous rocks and rare micritic carbonate. For example, in Section 5R-1, small pebbles within sandstone are overlain by isolated well-rounded pebbles; this interval is interpreted as an original >1-m-thick conglomerate bed. The well-rounded pebbles and granules clearly underwent previous reworking, probably related to wave or current action in a shallow-water setting, before being deposited within debris flows into a deep-water setting. Notably, shallow-water-derived benthic foraminifers (inner neritic) are recorded within some clasts in Unit II (Core 5R; see **"Benthic Foraminifers,"** p. 15).

This sequence of sandstone and conglomerate suggests differing sediment gravity-flow events in which the matrix-supported conglomerates were deposited by debris flows, whereas the sandstones and siltstones were deposited from high- and low-density turbidity currents. Such composite depositional units are characteristic of relatively steep, proximal settings (e.g., see Miall, 1984).

Petrographic study of a small number of clasts suggests that the main source was an arc-type terrane including basalt, dolerite, and andesite. One interesting aspect is the variety of basic volcanic rock types present. Several of these could have alkaline affinities (although titanoaugites are not present). These extrusives could be shoshonitic (e.g., similar to the high-K lavas from Lusancay and Woodlark Islands; see Smith, 1976; Johnson et al., 1978). Study of thin sections indicates the provenance was varied and included acidic volcanic, metamorphic, and ophiolitic rocks in addition to the mainly basic volcanic rocks that formed clasts. Also, the textural maturity, especially of the basaltic grains, and admixing with bioclasts, indicates derivation from a high-energy shallow-water setting.

Lithostratigraphic Unit III

Description: sandstone and siltstone
Interval: Cores 180-1116A-9R through 18R
Depth: 62.6–158.9 mbsf
Age: Pliocene

This unit is marked by a return to a finer grained succession of sandstone and siltstone without conglomerate. The upper part of this unit was recovered only as drilling breccia, whereas the lower part (below Core 13R; 110.6 mbsf) is better preserved and includes evidence of dewatering and sediment instability. Lithologies are calcareous. A small number of calcium carbonate analyses of claystones and siltstones indicate low values of 2.4–3.8 wt% (see **"$CaCO_3$, Sulfur, Organic Carbon, and Nitrogen,"** p. 17).

Sandstone

The sandstone is fine to medium grained, to locally coarse grained, and calcite cemented. The succession is tectonically tilted at up to 45° (see **"Structural Geology,"** p. 12). In the upper part of the unit the sed-

iment is mainly greenish gray, but below 110 mbsf this changes to reddish brown (e.g., Core 17R).

Most beds exhibit sharp, locally scoured bases (e.g., interval 180-1116A-15R-3, 16–84 cm) and are normal graded. Some sandstones are nearly structureless (see Fig. F14). In places, sandstone/mudstone couplets are present, which exhibit normal grading from fine sand to clay. Slight inverse grading was rarely noted at the base of sandstone beds (interval 180-1116A-16R-2, 10–22 cm). Planktonic foraminifers are locally concentrated at the tops of individual beds (e.g., interval 180-1116A-15R-2, 11–11.5 cm). Near the base of the recovered succession a single bed (>2.5 m thick) grades from coarse- to fine-grained sandstone. The sandstones are moderately to locally strongly bioturbated with both *Zoophycos* (interval 180-1116A-17R-1, 41–53 cm) and *Chondrites*.

Intraformational rip-up clasts are locally present in coarse-grained sandstone. Occasionally, these are large (up to 5 cm) and irregular in shape. In one case, large mud clasts have disintegrated, giving rise to a network of small cracks into which sand was injected (see **"Interpretation,"** p. 10). Elsewhere, small well-rounded granule-sized rip-up clasts are seen locally near the top of a bed (e.g., interval 180-1116A-16R-1, 0–42.5 cm).

The sandstones include unusually well developed sedimentary structures. A number of sandstone beds exhibit well-developed climbing-ripple lamination (e.g., Section 9R-1, and interval 180-1116A-17R-2, 14–24 cm; Fig. F15). Some individual cross-laminated intervals are truncated upward by overlying cross lamination, or common planar lamination (e.g., interval 180-1116A-14R-1, 21–28 cm; Section 16R-2; Fig. F16). Cross lamination in places dips in contrasting directions within a single bed. In addition, wavy or convolute lamination (e.g., see Fig. F15) is locally present (Fig. F17). Individual laminae are commonly composed of carbonaceous detritus (e.g., Section 14R-1). Some intervals show alternations of ripple lamination and wavy lamination without clear, sharp basal contacts.

Sand injection structures are well developed in the lower part of the unit (Figs. F18, F19). These structures are of both high angle (i.e., sandstone dikes) and low angle (i.e., sandstone sills) with respect to primary bedding. Most of the injection structures are composed of subhorizontal, fine- to medium-grained sandstone sills (up to 1 cm thick) within finer grained sandstone or siltstone. However, local injection of coarse-grained sandstone into underlying siltstone was observed in one case (e.g., interval 180-1116-15R-3, 0–8 cm). In most cases the origin of the injected coarser grained sediments is not apparent (i.e., whether local or far removed).

Study of seven thin sections of sandstone from Unit III revealed that the sandstones are feldspathic and rich in rock fragments, corresponding to lithic sandstones or subarkoses (see **"Site 1116 Thin Sections"**). Typically, grains are angular to subangular and poorly sorted, but a small proportion is subrounded to well rounded, especially the basalt grains. Sandstone contains fresh basalt (locally glassy), chloritized basalt, palagonite, felsic volcanics, rare dolerite, and gabbro. Mineral grains are plagioclase (commonly zoned), biotite, pyroxene, and rare hornblende. Lithic fragments are common polycrystalline quartz, schist (including commonly biotite schist; Fig. F20), serpentinite, and micritic and rare sandstone clasts. In addition, bioclasts include bivalve shell fragments, echinoderm plates, benthic foraminifers, and bryozoans. The sandstone typically has a fine-grained calcareous matrix.

F14. Faintly laminated sandstone, **p. 35.**

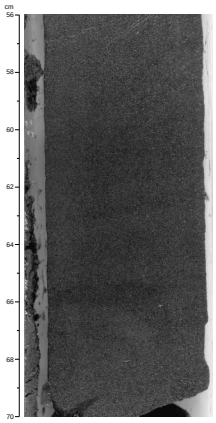

F15. Climbing-ripple-laminated sandstone, **p. 36.**

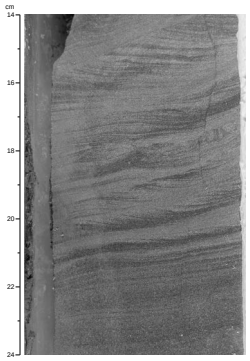

F16. Silty claystone sharply overlain by laminated sandstone, **p. 37.**

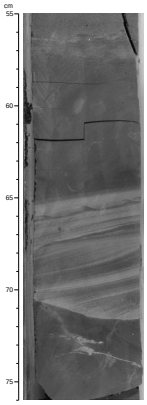

Siltstone, Silty Claystone, and Claystone

These sediments occur as two types of beds: (1) thin interbeds of siltstones and silty claystones. These beds are sharp based, mainly structureless, and are commonly graded from silty clay to clay. Parallel lamination is observed locally (interval 180-1116A-16R-1, 54–56 cm). The upper parts of individual thin beds are bioturbated, and small foraminifers are common. Several thin claystone beds show both sharp top and bottom contacts. (2) Thicker intervals of silty claystone are present near the base of the drilled succession. For example, one thick (>90 cm thick) silty claystone is graded with laminated siltstone restricted to the basal 5 cm (interval 180-1116A-16R-4, 90–95 cm). In addition, small-scale injection of sand into claystone was noted (interval 180-1116A-16R-3, 53–60 cm; Fig. **F21**), and small irregular fluid-escape structures are also present (Section 16R-CC).

The XRD analysis of the fine-grained sediment indicates the presence of plagioclase and quartz as major constituents, and chlorite, smectite?, calcite, illite, pyroxene, and amphibole as minor components (Table **T3**).

Interpretation

Unit III accumulated during the Pliocene at middle bathyal depths (500–2000 m; see **"Benthic Foraminifers,"** p. 15). Deposition took place in a suboxic setting characterized by abundant detrital organic matter input. Based on the occurrence of bioturbation, the sediments range from well-oxygenated to poorly oxygenated. The reddish color of the sandstones lower in the succession was possibly influenced by diagenesis.

The thick-bedded sandstones with inverse grading at the base are interpreted as deposits from high-density turbidity currents. The parallel lamination and ripple lamination in the upper part of these beds is suggestive of reworking by the tail of a turbidity current (see Allen, 1982). In addition, some of the sandstones can be interpreted mainly as classical turbidites. Beds exhibiting grading, and climbing-ripple and planar lamination can be inferred to be Ta, Tb, and Tc, Td divisions of the Bouma sequence (Bouma, 1962). Notably, the climbing-ripple lamination indicates high sediment fallout from suspension. However, complete Bouma-type sequences are not developed. The rare thick-bedded, graded claystones with graded siltstone bases are interpreted as deposits from large-volume, low-density turbidity currents. In addition, numerous sand/silt/clay couplets are interpreted as low-density turbidity current deposits (Piper et al., 1978). Units that show alternations of ripple lamination and wavy lamination are interpreted to suggest deposition from pulsating currents and perhaps bottom currents (Pickering et al., 1989).

The sand-injection structures are seen as the result of injection of coarse-grained sand into finer-grained sediment at varying angles. Such sand-injection structures may result from a high sedimentation rate that in turn causes entrapment of fluid. Elevated pore-water pressure then results, leading to sudden liquefaction and injection of fluidized sand into adjacent more coherent muddy sediments (Lowe, 1975). Such fluidization may simply relate to high sedimentation rate, but may also be tectonically triggered.

The petrographic evidence indicates essentially the same provenance as indicated by samples from Units I and II, with a mixture of clasts and

F17. Wavy, inclined, and convolute laminated sandstone, **p. 38.**

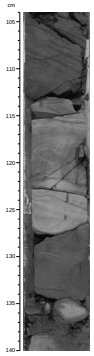

F18. Bioturbated silty claystone with sandstone above, **p. 39.**

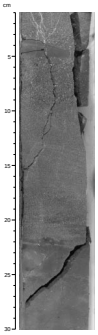

F19. Sand injection into clayey siltstone, **p. 40.**

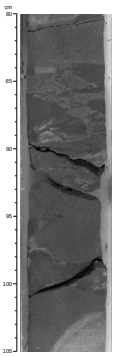

F20. Fragment of calc-schist in calcite cement, **p. 41.**

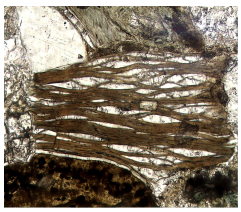

mineral grains from basic and acidic volcanic rocks, plutonic rocks, and some metamorphic rocks. Input of subordinate shallow-water-derived carbonate persists to the bottom the hole.

Depositional History

Site 1116 drilling was aimed to penetrate the deeper parts of a synrift sedimentary succession, based on seismic stratigraphic interpretation. The whole of the drilled interval accumulated at middle bathyal depths (500–2000 m) depths during Pliocene time. An early? to middle Pliocene age is inferred down through Core 17R, below which the age is undetermined. The average sedimentation rate was >70 m/m.y. for the entire succession. Several factors indicate that Quaternary sediments are absent from Site 1116. (1) Site 1116 sediments were dated as middle Pliocene or older (see **"Biostratigraphy,"** p. 14); (2) all the material is well lithified, suggesting that superficial sediments were removed; and (3) physical properties data show relatively high near-surface velocities and low porosities. These data are consistent with the removal of a Pleistocene to upper Pliocene section (see **"Physical Properties,"** p. 17). A possible explanation is that younger sediments were deposited, but then removed, perhaps related to tectonic uplift of the Moresby Seamount.

The recovered section is interpreted as a single deep-water succession dominated by gravity flow and interbedded fine-grained sediments. The gravity deposits range from debris-flow deposits and possible high-density turbidites in the case of the paraconglomerates (Unit II), to classical turbidites with partial Bouma divisions, to mud turbidites (Units I and III). In addition, minor redeposition by the tail of high-concentration turbidity currents or by bottom currents may have occurred. The well-rounded clasts in the conglomerate, including sporadic shallow-water benthic foraminifers, were redeposited from an inferred high-energy beach or fluvial setting and were finally redeposited within debris flows and possible high-density gravity flows (Unit II). Bottom-water conditions were at least relatively oxidizing in view of the common bioturbation. However, subsurface anoxia was probably developed as indicated by the presence of disseminated organic matter. Slightly elevated levels of sulfur (see **"$CaCO_3$, Sulfur, Organic Carbon, and Nitrogen,"** p. 17) correlate with the common occurrence of pyrite. The presence of dewatering structures and sand-injection structures (small dikes and sills) indicate the development of elevated pore pressure. Dewatering and fluidization was possibly seismically triggered, and indeed, there is much evidence of faulting at this site (see **"Structural Geology,"** p. 12).

The petrographic evidence indicates the clasts were derived from a dominantly calc-alkaline arc setting. The voluminous basaltic and acidic volcanic rocks are assumed to have been derived from the Miocene Trobriand Arc (including Amphelts Island and Egum Atoll). The former axis of this arc is believed to be located close to the present day location of Moresby Seamount and thus, a relatively proximal origin is possible. The basic volcanics may include unusual relatively alkaline basalts related to arc rifting. The serpentinite, rare chromite, and some at least of the dolerite and gabbro grains, may have an ophiolitic origin, related to derivation from deeper levels of the Papuan Ultramafic Belt, which is believed to have been emplaced over a region including the D'Entrecasteaux Islands and Moresby Seamount in Paleocene to Eocene time (prior to inception of the Trobriand Arc; Davies and Jaques,

F21. Sand-injection structure within silty claystone, **p. 42.**

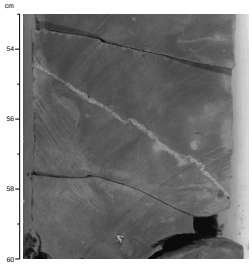

1984). In addition, the common schist can possibly be correlated with the Owen Stanley or Kaga Metamorphics, interpreted as an early Tertiary accretionary complex that regionally underlies the Papuan Ophiolitic Belt (Rogerson et al., 1987). Thus, material was apparently derived from all parts of the regional tectonostratigraphy.

In conclusion, the overall sedimentary regime is consistent with heterogeneous proximal sources feeding a subsiding rift basin in the Pliocene.

STRUCTURAL GEOLOGY

The 158.9-m-thick section cored at Site 1116 is subdivided into four structural domains (Fig. F22). The top and bottom of the section are undeformed (Domain I) and little deformed (Domain IV), respectively. In between, Domain II shows soft-sediment deformation whereas Domain III is affected by brittle faulting. However, the boundaries between the three upper structural domains are not precisely defined because of low recovery.

Bedding dips range from 0° to 50° throughout Hole 1116A with an average at 20° (Figs. F22, F23). High values, mostly related to soft-sediment deformations, are scattered throughout the section, except within Domain IV at the bottom of Hole, where they do not exceed 30°.

Domain I (0–24.2 mbsf)

Domain I extends from the seafloor to 24.2 mbsf (Cores 180-1116A-1R to 3R), and involves sandstones, siltstones, and claystones of all but Core 4R of Lithostratigraphic Unit I (see "Lithostratigraphic Unit I," p. 4).

Its overall structure is poorly imaged because of very low recovery in Cores 180-1116A-1R (0–6.6 mbsf) and 3R (16.2–24.2 mbsf) where only pebbles were recovered. The nearly continuous section lying from 6.6 to 7.9 mbsf (Section 180-1116A-2R-1) exhibits beds dipping from 0° to 10° (Fig. F22). Rare evidence for brittle deformation is present, consisting mainly of mm-sized veins filled with either calcite (interval 180-1116A-1R-CC, 55–60 cm) or quartz (interval 180-1116A-2R-1, 13–15 cm).

Domain II (24.2–101.0 mbsf)

Domain II includes the interval from 24.2 to 101.0 mbsf (Cores 180-1116A-4R to 12R), and is composed of the lowermost core of lithostratigraphic Unit I, all of Unit II, and the upper half of Unit III (see "Lithostratigraphy," p. 4). The few (7) measurements of bedding dips show relatively high values, between 5° and 50° (Fig. F22), that are confidently assigned to soft-sediment deformation. Additional soft-sediment deformation is observed at intervals 180-1116A-4R-1, 90–130 cm, and 9R-1, 115–120 cm.

The most significant structure (interval 180-1116A-4R-1, 90–130 cm; Fig. F24) consists of a steeply dipping (50°), finely laminated silt/clay lying along the normal limb of an isoclinal and overturned fold whose hinge zone occurs at 100–110 cm. The asymmetry of the subsidiary S-shaped folds developed along the normal flank of the structure typifies a west-verging structure with respect to the core reference frame. The fold limb is disrupted by two sets of low-angle extensional microfaults with opposite senses of displacement, involving either thicker sandy

F22. Summary of structural features, Site 1116, p. 43.

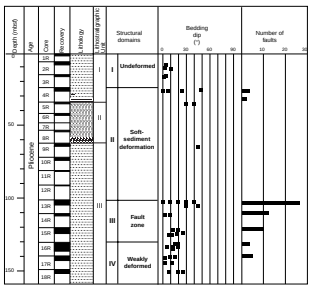

F23. Bedding dip measurements, Hole 1116A, p. 44.

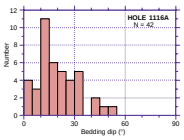

F24. Gravitational deformation in a well-laminated sequence, p. 45.

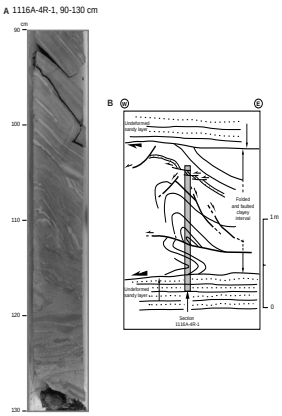

layers or more silty material. The base of the fold is sharply truncated at 113 cm by a shallow-dipping plane, which in turn lies on top of a 10-cm-thick horizontal recumbent folded zone, probably detached from underlying and undeformed sandstones along a second flat-lying sliding surface.

The association of such folding and low-angle extensional faulting is typical of gravity-driven structures that may have preferentially developed within clay-rich intervals detached from bounding sandy levels along shallow-dipping shear planes. These deformations are likely to have taken place shortly after deposition of the synrift sediments during compaction, so that dominantly-clayey sequences could still be deformed by folding, because more competent material accommodated strain by faulting.

Evidence for later faulting is observed in interval 180-1116A-4R-2, 5–7 cm, where a flat-lying and dominantly sandy succession is affected by a small-scale asymmetric graben-like structure bounded by steeply dipping (60°–70°) normal microfaults (Fig. F25). The steep attitude of the faults may indicate that they developed through relatively indurated sandy material, probably at a later stage than the low-angle structures described above.

At 62.6–63.6 mbsf (interval 180-1116A-9R-1, 0–100 cm) and 72.2–73.3 mbsf (interval 180-1116A-10R-1, 0–110 cm), fine-grained siltstones and claystones are intensely broken into mm- to cm-sized angular fragments with polished surfaces. Whether the origin of this scaly-like fabric is coring induced or tectonic is questionable because only one slickensided surface has been observed in interval 180-1116A-10R-1, 95–97 cm. Core 180-1116A-10R is, therefore, placed into Domain II, and the top of the underlying fault zone (Domain III) is located below the poorly recovered Cores 11R and 12R (e.g., at 101.0 mbsf).

Domain III (101.0–130.0 mbsf)

Domain III corresponds to a fault zone lying from 101.0 to 130.0 mbsf (Sections 180-1116A-13R-1 to 15R-2). Its upper limit is clearly marked on Figure F22 by an abrupt increase of fault frequency. On the histogram of Figure F26A, the fault dip population displays a bimodal distribution with two peaks at 35°–45° and 75°–90°.

Steep faults are mainly confined to the upper part of Domain III (Sections 180-1116A-13R-1 and 2; 101.0–102.7 mbsf), and mostly show strike-slip displacements. On the other hand, dip-slip faults preferentially occur in the lower part of the fault zone, in Sections 180-1116A-14R-1 (110.6–111.9 mbsf) and 15R-1 and 2 (120.3–122.7 mbsf). The fault dip vs. slickenside plunge diagram (Fig. F26B) shows that dip-slip and strike-slip faults are predominant with respect to oblique-slip faults. At interval 180-1116A-15R-2, 90–106 cm, normal offsets a few mm long are well documented along a steep and sigmoidal fault. Calcite-filled veins occur in an extensional relay zone along the curved fault (Fig. F27). In intervals 180-1116A-14R-1, 0–10 cm, and 85–95 cm, scaly-type fabrics associated with steep dip-slip normal faults likely result from fragmentation of fine-grained silts during brittle extensional faulting.

Domain IV (130.0–158.9 mbsf)

Domain IV lies from Section 180-1116A-16R-1 to the base of the hole (130.0–158.9 mbsf). Its upper boundary corresponds to a rapid decrease in fault frequency (Fig. F22). However, a few dip-slip normal faults and

F25. Steep normal microfaults bounding a graben-like structure, p. 46.

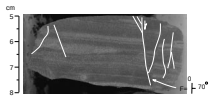

F26. Fault measurements in Domain III, p. 47.

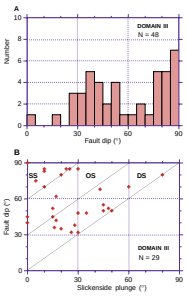

F27. Sigmoidal normal fault with calcite in a curved relay zone, p. 48.

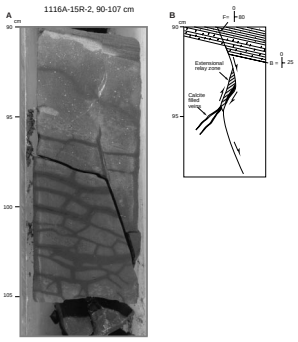

strike-slip faults occur throughout Domain IV, especially in intervals 180-1116A-17R-1, 65–75 cm (dip-slip faults), and 140–145 cm (strike-slip faults). In interval 180-1116A-17R-1, 100–115 cm, nearly vertical fault planes, ~10 cm long, are typically sigmoidal and show both apparent normal and reverse offsets a few mm long. These faults are likely to have been generated as early compaction-related features, as also evidenced in interval 180-1116A-17R-2, 15–25 cm (141.35–141.45 mbsf), where a similar vertical fault fades away downward. Arrays of mm-sized calcite-filled veins are present in the uppermost part of Domain IV in intervals 180-1116A-16R-1, 3–6 and 100–110 cm, and 16R-2, 0–7 and 22–30 cm. Domain IV generally contains long unbroken pieces of siltstones a few dm long, which are locally disrupted by sharp coring-induced (?) conjugate fractures (intervals 180-1116A-16R-5, 40–50 cm; 18R-2, 5–35 and 85–115 cm). Throughout Domain IV, bedding dip distribution is similar to that for the complete Hole 1116A with a well-marked peak at 15°, but with fewer high values (Fig. F28).

F28. Bedding dips in Domain IV, p. 49.

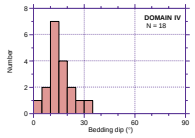

BIOSTRATIGRAPHY

Calcareous Nannofossils

Sample 180-1116A-1R-1, 106–112 cm, contains common, moderately preserved nannofossils. Samples 180-1116A-1R-CC through 18R-CC contain rare to few nannofossils with some almost barren intervals. Preservation ranges from poor to moderate (mostly poor).

Sediment contained in Sample 180-1116A-1R-1, 106–112 cm, is in Zone NN18 or older, based on the presence of *Discoaster brouweri*. We found rare *D. brouweri* in Sample 180-1116A-1R-CC, also indicating Zone NN18 or older (Fig. F29).

F29. Biostratigraphic units and ages, Hole 1116A, p. 50.

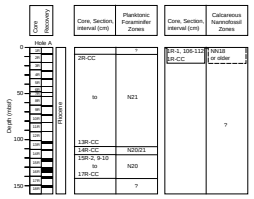

Planktonic Foraminifers

Abundance and Preservation

The occurrence of planktonic foraminifers was highly variable in Hole 1116A and where found, their preservation was moderate to poor. Specimens were abundant to common in Samples 180-1116A-2R-CC, 4R-CC, 9R-CC, 13R-CC, and 15R-CC; they were few to rare in Samples 180-1116A-1R-1, 106–112 cm, 5R-CC, 7R-CC, 10R-CC, 12R-CC, 14R-CC, 16R-CC, and 17R-CC. Samples 180-1116A-1R-CC, 3R-CC, 4R-2, 17–18 cm, and 18R-CC were barren of planktonic foraminifers. No paleontological samples were recovered from Samples 180-1116A-6R-CC and 8R-CC, and Sample 180-1116A-11R-CC was too small for the recovery of foraminifers.

Zonation

The zonal scheme for planktonic foraminifers at the site is indicated in Figure F29 and the distribution of species is shown on Table T4. Zone N21 was determined for Samples 180-1116A-2R-CC through 13R-CC, based on the occurrence of *Globigerinoides fistulosus* in Samples 2R-CC and 13R-CC and the absence of *Globorotalia truncatulinoides*. Sample 180-1116A-14R-CC is in either Zone N21 or Zone N20. It contains questionable *G. fistulosus* along with *Globorotalia crassaformis*. Sample 180-1116A-15R-2, 9–10 cm, contains *Globorotalia margaritae* (last appearance

T4. Planktonic foraminifers, Hole 1116A, p. 68.

datum [LAD] in Zone N20). Samples 180-1116A-15R-CC and 17R-CC are also placed in Zone N20, based on the occurrence of *Globorotalia crassaformis ronda* in the absence of *G. fistulosus* and *Globorotalia tosaensis*.

Benthic Foraminifers

Hole 1116A, in 1851 m water depth, had a benthic foraminiferal assemblage indicative of a middle bathyal (500–2000 m) depth throughout, characterized by *Cibicidoides rugosus, Hoeglundina elegans,* and *Oridorsalis umbonatus,* as well as *Ceratobulimina pacifica* (in Sample 180-1116A-2R-CC), *Osangularia culter* (in Sample 180-1116A-13R-CC), and *Pullenia bulloides* as well as *Sphaeroidina bulloides* (in Sample 180-1116A-15R-CC). *Globobulimina* sp. is found with relatively high frequency in Samples 180-1116A-2R-CC, 7R-CC, 13R-CC, 15R-CC, and 16R-CC, suggesting a substrate rich in organic matter at the time of deposition. The presence of inner neritic (<50 m water depth) benthic species of *Amphistegina, Calcarina,* and *Elphidium* in Samples 180-1116A-5R-CC, 9R-CC, and 17R-CC indicates turbiditic horizons.

Sediment Accumulation Rate

At Site 1116 we estimated sedimentation rate on the basis of nannofossil and foraminifer datum events (Fig. **F30**). The average sedimentation rate for the horizon 1.06 to 104.12 mbsf is calculated to be at least 70 m/m.y.

PALEOMAGNETISM

The investigation of magnetic properties at Site 1116 included (1) the measurement of bulk susceptibility of whole core sections, (2) point susceptibility and remanent magnetization of archive half core sections, and (3) susceptibility and its anisotropy and remanent magnetization of discrete samples.

Magnetic Susceptibility

Magnetic susceptibility measurements were made on whole core sections as part of the multisensor track (MST) analysis (see **"Magnetic Susceptibility,"** p. 19), and on half core sections as part of the archive multisensor track (AMST) analysis. The MST and AMST susceptibilities (uncorrected for volume) values ranged between the order of 10^{-3} and 10^{-2} SI (Fig. **F31**).

The mean susceptibility, the degree of anisotropy (P_j), and the shape parameter (T) of the susceptibility ellipsoid (Jelinek, 1981) of discrete samples are shown in Figure **F32A**. The inclinations of the maximum (K_{max}) and minimum (K_{min}) susceptibility axes of the ellipsoid before and after tilt correction are also shown, along with the dips used for the bedding correction.

Mean volume susceptibilities ranged between ~5×10^{-3} and 2×10^{-3} SI. These values were similar to or slightly higher than those at Hole 1114A. The P_j values ranged between ~1.05 and 1.15. The T values were dominantly higher than 0.5, indicating the predominance of oblate magnetic fabrics. Below ~100 mbsf, tilt-corrected inclinations of K_{max} axes had inclinations shallower than 30° and K_{min} axes steeper than ~60°. The

F30. Age-depth relationship, Site 1116, **p. 51.**

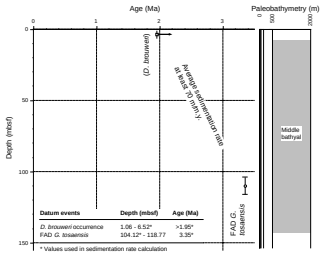

F31. Susceptibility data from MST and AMST measurements, Site 1116, **p. 52.**

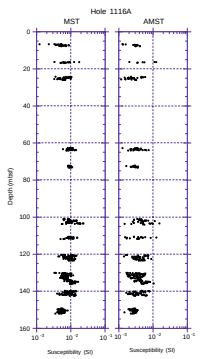

F32. AMS data from discrete sample measurements, **p. 53.**

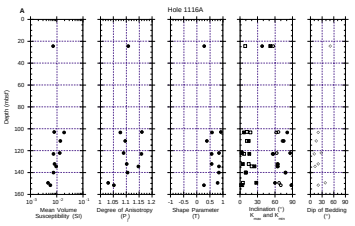

shape and direction of the magnetic fabrics may reflect the degree of sediment compaction.

Magnetic fabrics were corrected for bedding tilt and for core orientation estimated from the declinations of the stable remanence from discrete samples (Fig. F32B). This correction assumes a geocentric axial dipole field in which the declination was 0° during normal polarity states and 180° during reversed polarity states. The polarity for each sample was determined from the sign of the tilt-corrected inclination after AF demagnetization at 25 mT. After corrections for bedding tilt and core orientation, K_{max} axes below 100 mbsf were aligned roughly northeast-southwest (Fig. F32B). K_{min} axes were slightly aligned to the northeast. In general, K_{max} axes in sedimentary rocks indicate a direction that may be either parallel or perpendicular to the paleocurrent direction (Tarling and Hrouda, 1993); therefore, the orientation of the magnetic fabrics below 100 mbsf may reflect a northeast-southwest or northwest-southeast paleocurrent during sedimentation. The alignment of K_{min} axes to the northeast, with a clear separation of K_{int} (K intermediate) aligned roughly perpendicular to both K_{max} and K_{int} axes, suggests an imbrication of the magnetic fabric. These observations suggest a paleocurrent direction to the southwest. Alternatively, K_{min} axes appear somewhat spread across a northwest-southeast girdle that includes K_{int} axes, which suggests a northwest-southeast paleocurrent direction. Additional data may help to resolve which paleocurrent direction is correct.

Remanent Magnetization

Measurements of remanent magnetization were made on relatively undisturbed sections from archive half cores and on discrete samples taken from working half core sections. Results are shown in Figures F33 and F34 and are listed in Table T5.

A total of 11 discrete samples were measured. Initial natural remanent magnetization (NRM) intensities were on the order of 10^{-2} A·m^{-1}. Demagnetization behavior of discrete samples showed the presence of two or more magnetic components. A soft component removed between 0 and 5 mT generally showed a downward direction. After removal of the soft component, all samples showed a stable component that decayed approximately linearly toward the origin of the vector demagnetization plot between 15 and 25 mT (Fig. F33); this component is referred to as the characteristic remanent magnetization (ChRM).

Intensity of remanent magnetization of long cores after AF demagnetization at 25 mT was on the order of 10^{-3} to 10^{-2} A·m^{-1} (Fig. F34A, F34B). Inclinations corrected for bedding tilt showed normal and reversed polarities. Declinations were highly scattered as a result of the RCB drilling process. Discrete sample results were generally consistent with the long core data.

Because of poor recovery and discontinuous data sets, no attempt was made to interpret the data in terms of the magnetic polarity time scale.

F33. Demagnetization behavior of discrete samples, p. 55.

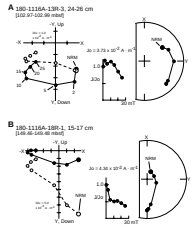

F34. Downhole plots of declination, inclination, and intensity, p. 56.

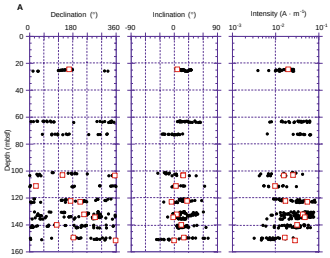

T5. Measurements of remanent magnetization, Site 1116, p. 69.

INORGANIC GEOCHEMISTRY

Only a single whole-round sample, Sample 180-1116A-13R-2, 81–91 cm, was collected from Hole 1116A. No interstitial water was recovered, even upon extended squeezing at maximum pressure.

ORGANIC GEOCHEMISTRY

At Site 1116, the shipboard organic geochemistry consisted of determinations of TOC, inorganic carbon, total carbon, total nitrogen, and total sulfur in sediments, in addition to the routine hydrocarbon gas safety monitoring procedure.

Volatile Hydrocarbons

Headspace methane concentrations for Site 1116 remained low (<10 ppmv) throughout the hole (Table T6). The only other hydrocarbon that was detected was *n*-pentane. This compound was found at an extremely unusual, high concentration (459 ppmv) at 35.2 mbsf (Table T6). Because this concentration does not coincide with an increase in any other hydrocarbons, it is likely an artifact.

T6. Headspace gas in sediments, Site 1116, p. 70.

$CaCO_3$, Sulfur, Organic Carbon, and Nitrogen

The $CaCO_3$ contents of sediments at Site 1116 were low, ranging between 1.93 and 4.84 wt% (Table T7). Organic carbon and sulfur concentrations were both low, averaging 0.57 and 0.30 wt%, respectively (Table T7). The available C/N ratios show that the organic carbon has a probable terrigenous source; however, a marine source (C/N = 9) is indicated at 17.02 mbsf (Table T7).

T7. $CaCO_3$, carbon, nitrogen, and sulfur contents, Site 1116, p. 71.

PHYSICAL PROPERTIES

Introduction

Physical properties measurements at Site 1116 were limited by low core recovery, and consequently, the physical properties data set for the site is sparse. Physical properties evaluation included nondestructive measurements of bulk density, bulk magnetic susceptibility, and natural gamma ray on unsplit core using the MST. Discrete measurements of longitudinal and transverse *P*-wave velocities and index properties were collected on split cores. Depending on the level of sediment induration, thermal conductivity was measured from unconsolidated whole cores, discrete rock slices, or conglomerate clasts. Poor recovery and fragmented sections in Cores 180-1116A-1R, 5R through 8R, and 11R through 12R precluded use of the MST at these locations. Further, it was not possible to measure compressive strength and undrained shear strength because of the well-lithified nature of the recovered sediment.

Density and Porosity

Bulk densities at Site 1116 were derived from both gamma-ray attenuation porosity evaluator (GRAPE) measurements conducted on unsplit cores and discrete density measurements on sediment and rock samples

(Table T8; also in ASCII format in the TABLES directory). A full compilation of GRAPE data is presented in ASCII format with the MST measurement data set on the accompanying LDEO CD-ROM. Composite profiles of these independently derived bulk densities indicate a fair agreement between the two, with the discrete measurements tending to define an upper boundary of the GRAPE densities (Fig. F35A).

One exception occurs for Core 180-1116A-3R, in which the index properties estimate is ~3.1 g·cm^{-3}. This density, checked and remeasured, corresponds to an isolated sample of calcite-cemented (checked with XRD analysis), low porosity, high grain density, fine-grained sandstone and is not representative of lithostratigraphic Unit I (see "Lithostratigraphic Unit I," p. 4). There is no obvious explanation for this outlier value. GRAPE underestimation of bulk density may be related to small core diameters produced by RCB drilling. Corrections were attempted at a previous site (see "Density and Porosity," p. 62, in the "Site 1109" chapter), but could not fully account for the discrepancy. Because of these discrepancies and the large scatter in the GRAPE data, our discussion will focus primarily on the discrete bulk density measurements.

In contrast to bulk densities obtained from other Leg 180 sites, the near-surface bulk density at Site 1116 is relatively high, having a value of ~2.15 g·cm^{-3} at depths of 7–8 mbsf (Fig. F35A). Bulk densities remain approximately constant over the length of the borehole with the average at 2.30 g·cm^{-3}, and show no obvious correlation with either the lithostratigraphic units or their boundaries. The relatively high near-surface densities imply removal of the uppermost sediment, an implication supported by the absence of Pleistocene deposits (see "Biostratigraphy," p. 14).

Grain densities average 2.73 g·cm^{-3} from the seafloor to 152 mbsf (Fig. F35B). An explanation for the scatter associated with estimates at 16 and 25 mbsf is unclear, but may relate to experimental or instrument-related errors. As with bulk densities, the grain densities are approximately constant irrespective of the lithology recovered (Fig. F35B).

At Site 1116, porosities show a large degree of scatter, ranging from 10% to 41%, with an average of ~26.5% (Fig. F36A). Porosity values throughout the entire profile are low, as illustrated by near-seafloor values of 33% and 11%, and do not show the usual negative exponential variation of porosity with depth often seen in normally compacting sediments (Athy, 1930). As indicated in Figure F36A, porosities lower than 15% generally correlate with isolated samples of carbonate-cemented sediments (see "Depositional History," p. 11). The anomalous near-seafloor porosities may reflect an environment in which sediment deposited on what is now the top of Moresby Seamount has since been eroded. This hypothesis is consistent with (1) the absence of calcareous nannofossil Subzones NN21B to NN19A at the top of the borehole, which indicates a hiatus in the sedimentary record of at least 1.95 Ma (see "Biostratigraphy," p. 14); and (2) the interpretation of reflection seismic data suggesting the truncation of reflectors.

To estimate the thickness of sediment that may have been eroded, a least squares exponential curve was fit to porosity data with the extreme low values removed (Fig. F36B). The curve fitting predicts a surface porosity of 31.6% and a compaction decay constant of 0.0009 m^{-1}. Significant data scatter and the small number of observations result in a poor correlation coefficient of 0.3 (Fig. F36B). Extrapolating the exponential porosity-depth relationship to the presumed paleosurface, assuming initial surface porosities of 75% (i.e., seafloor porosities from

T8. Index properties measured in cores, Site 1116, p. 72.

F35. Site 1116 bulk and grain densities, p. 58.

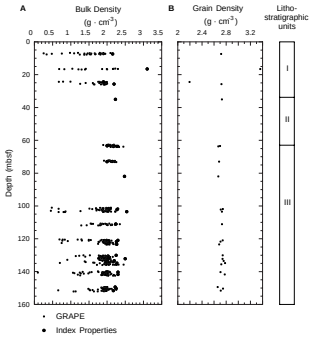

F36. Site 1116 porosity data, p. 59.

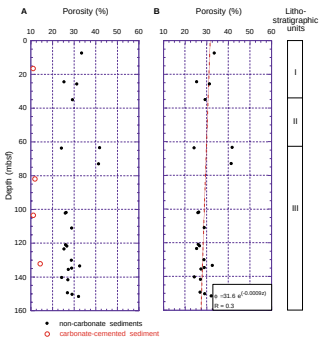

previous Leg 180 sites), implies that ~960 m of sediment has been removed from the upper stratigraphic units at this site. This estimate is in broad agreement with a comparison of porosity-depth relationships from other Leg 180 sites (e.g., Sites 1109 and 1115). It is important to stress that because of the limited data set and the low correlation coefficient, the erosion estimate is poorly constrained.

Compressional Wave Velocity

Compressional wave, or *P*-wave, velocity was measured on split cores using the PWS3 contact probe system. All cores were sufficiently indurated to prepare ~10-cm^3 cubes, thereby allowing for velocity measurement in the transverse (x and y) and longitudinal (z) directions. The PWS data are presented in Table T9 (also in ASCII format in the TABLES directory). Most of the Hole 1116A cores consisted of indurated sediment, with the exception of Cores 180-1116A-5R through 8R, which consisted primarily of conglomerate clasts removed from the matrix material. The recovery of conglomerate clasts provided an opportunity to characterize the transverse (x) direction for a variety of igneous rock types. It should be noted, however, that the original orientation of the clasts is unknown because of possible rotation within the core barrel. Clasts consisted of vesicular, porphyritic, and amygdaloidal basalts, along with andesites and dolerite (see "Lithostratigraphy," p. 4).

The velocities show a large degree of scatter ranging from 2400 to 5500 m·s^{-1} (Fig. F37). Some of this scatter relates to calcite-cemented sandstone and siltstones of lithostratigraphic Units I and III (see "Lithostratigraphic Unit I," p. 4, and "Lithostratigraphic Unit III," p. 8) and the selected sampling of conglomerate clasts from lithostratigraphic Unit II (see "Lithostratigraphic Unit II," p. 6). Near-surface velocities obtained in the upper 10 m of the borehole range from ~2200 to ~2800 m·s^{-1}, which are significantly higher than expected for shallow-marine sediments. However, these higher velocities are consistent with the low near-surface porosities. Evaluation of the triaxial velocity measurements indicates that transverse velocities are systematically faster than longitudinal velocities (Fig. F38A), with velocity anisotropies ranging from 0.5% to ~9% (Fig. F38B).

Thermal Conductivity

Thermal conductivity measurements were conducted on split cores from Site 1116 using the half-space method. The thermal conductivity values presented in Figure F39 are averages of repeat measurements in the same interval. A full compilation of the data is presented in Table T10 (also in ASCII format in the TABLES directory).

Thermal conductivity values in sediments at Site 1116 are likely governed by pore space and composition of clasts. Thermal conductivity measurements for Site 1116 show considerable variation, ranging between 1.0 and 2.2 W·m^{-1}·°C^{-1} (Fig. F39). Generally, low-porosity calcareous sandstones from lithostratigraphic Units I and III are associated with conductivities higher than 1.8 W·m^{-1}·°C^{-1}. Otherwise, no direct correlation exists between lithostratigraphic units and thermal conductivities.

Magnetic Susceptibility

At Site 1116, estimates of magnetic susceptibility were routinely obtained as part of the MST measurements. The quality of magnetic

T9. Longitudinal and transverse velocities, Site 1116, p. 73.

F37. Site 1116 transverse and longitudinal velocities, p. 60.

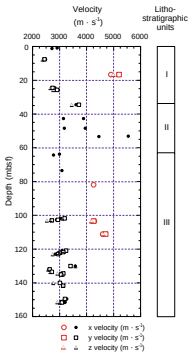

F38. Site 1116 longitudinal velocity vs. transverse velocity, and anisotropy, p. 61.

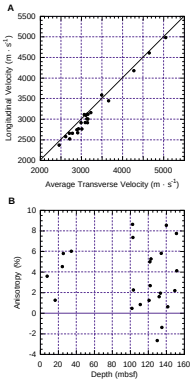

F39. Site 1116 thermal conductivity, p. 62.

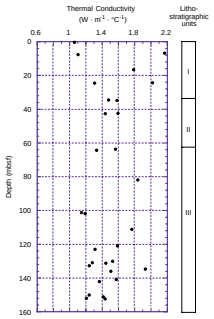

T10. Thermal conductivity values, Site 1116, p. 74.

susceptibility data is often poor in RCB-cored boreholes, commonly because of a reduced core diameter and drilling induced fracturing. At Site 1116, the low recovery throughout the succession also limits the degree of interpretation that can be placed on the magnetic susceptibility data. The full data set can be found as part of the MST compilation in ASCII format on the accompanying LDEO CD-ROM.

Because of poor recovery magnetic susceptibility data were obtained only from 5–25, 65–75, and 100–152 mbsf (Fig. **F40A**). Given that lithostratigraphic Units I and III consist of a monotonous assemblage of sandstone and siltstone couplets (see **"Lithostratigraphic Unit I,"** p. 4, and **"Lithostratigraphic Unit III,"** p. 8), there is no obvious relationship between the general susceptibility trends and either the lithology and/or the grain-size distribution. However, isolated susceptibility peaks often correlate with volcaniclastic sandstone layers (see **"Lithostratigraphy,"** p. 4).

F40. Site 1116 magnetic susceptibility and NGR data, **p. 63.**

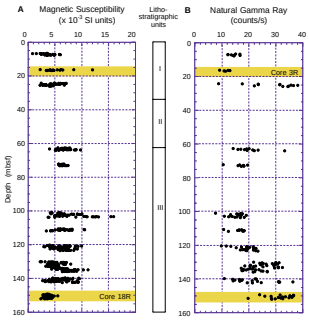

Natural Gamma Ray

Natural gamma-ray (NGR) emissions were recorded on cores from Site 1116 as part of continuous MST measurements. A full compilation of NGR values is presented with the MST measurement data set in ASCII format on the accompanying LDEO CD-ROM.

Irregular core recovery makes it difficult to define trends within the NGR data (Fig. **F40B**). Nevertheless, comparing the magnetic susceptibility with NGR on a core-by-core basis suggests that there is a general inverse relationship between the two. For example, a relatively high amplitude magnetic susceptibility associated with Core 180-1116A-3R (16.20–17.09 mbsf) correlates with a low-amplitude NGR count (Fig. **F40B**). In contrast, the low magnetic susceptibility for Core 180-1116A-18R (149.30–152.43 mbsf) correlates with a NGR high. This inverse relationship suggests that the clastics containing the magnetic mineralogy are distinct from those clastic units containing radiogenic components. As with the magnetic susceptibility, the general NGR trends do not correlate with either the lithology or the grain-size distribution.

REFERENCES

Allen, J.R.L., 1982. *Sedimentary Structures: Their Character and Physical Basis* (Vols. 1 and 2): Amsterdam (Elsevier).

Athy, L.F., 1930. Density, porosity, and compaction of sedimentary rocks. *AAPG Bull.*, 14:1–24.

Bouma, A.H., 1962. *Sedimentology of Some Flysch Deposits: A Graphic Approach to Facies Interpretation:* Amsterdam (Elsevier).

Davies, H.L., and Jaques, A.L., 1984. *Emplacement of ophiolite in Papua New Guinea*. Spec. Publ.—Geol. Soc. London, 13:341–350.

Jelinek, V., 1981. Characterization of the magnetic fabric of rocks. *Tectonophysics,* 79:63–67.

Johnson, R.W., Mackenzie, D.E., and Smith, I.E.M., 1978. Volcanic rock associations at volcanic plate boundaries: re-appraisal of the concept using case histories from Papua New Guinea. Tectonophysics, 46:197–216.

Lowe, D.R., 1975. Water escape structures in coarse-grained sediments. *Sedimentology,* 22:157–204.

Miall, A.D., 1984. *Principles of Sedimentary Basin Analysis* (2nd ed.): New York (Springer-Verlag).

Pickering, K.T., Hiscott, R., and Hein, F.J., 1989. *Deep-marine Environments: Clastic Sedimentation and Tectonics:* London (Unwin Hyman).

Piper, D.J.W., 1978. Turbidite muds and silts on deepsea fans and abyssal plains. *In* Stanley, D.J., and Kelling, G. (Eds.), *Sedimentation in Submarine Canyons, Fans and Trenches:* Stroudsburg, PA (Dowden, Hutchinson and Ross), 163–175.

Rogerson, R., Hilyard, D., Francis, G., and Finlayson, E., 1987. The foreland thrust belt of Papua New Guinea. *Proc. Pac. Rim Congr.,* 87:579–583.

Smith, I.E.M., 1976. Peralkaline rhyolites from the D'Entrecasteaux Islands, Papua New Guinea. In Johnson, R.W. (Ed.), *Volcanism in Australasia:* Amsterdam (Elsevier), 275–285.

Tarling, D.H., and Hrouda, F., 1993. *The Magnetic Anisotropy of Rocks:* London (Chapman and Hall).

Figure F1. Lithologic log of the succession recovered at Site 1116. (For key to symbols, see Fig. F2, p. 52, in the "Explanatory Notes" chapter.)

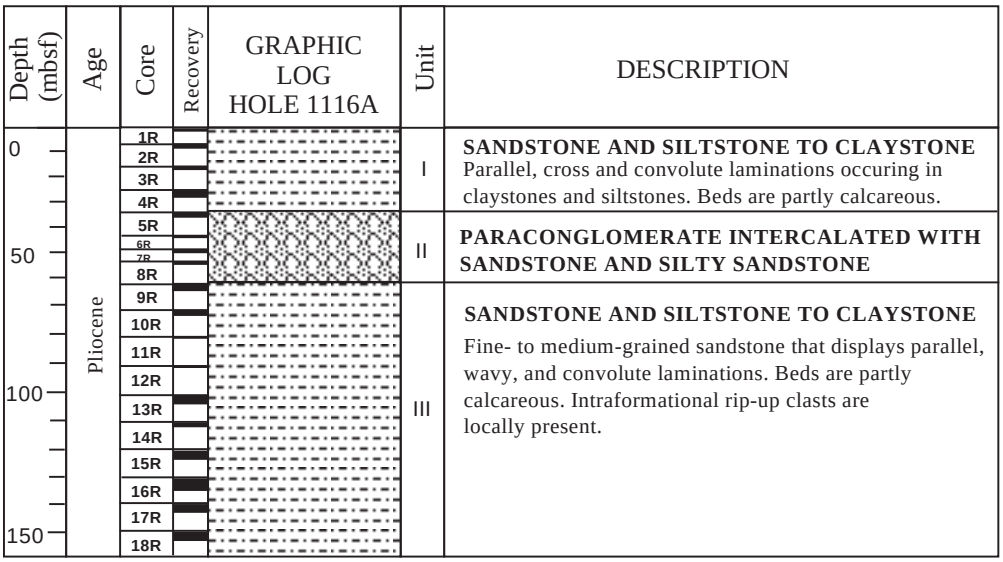

Figure F2. Digital photomicrograph (crossed nicols) of a basaltic clast with plagioclase laths in a glassy matrix, surrounded by feldspar and quartz grains and other basic volcanic clasts; cement is calcite spar (interval 180-1116A-1R-1, 58–60 cm).

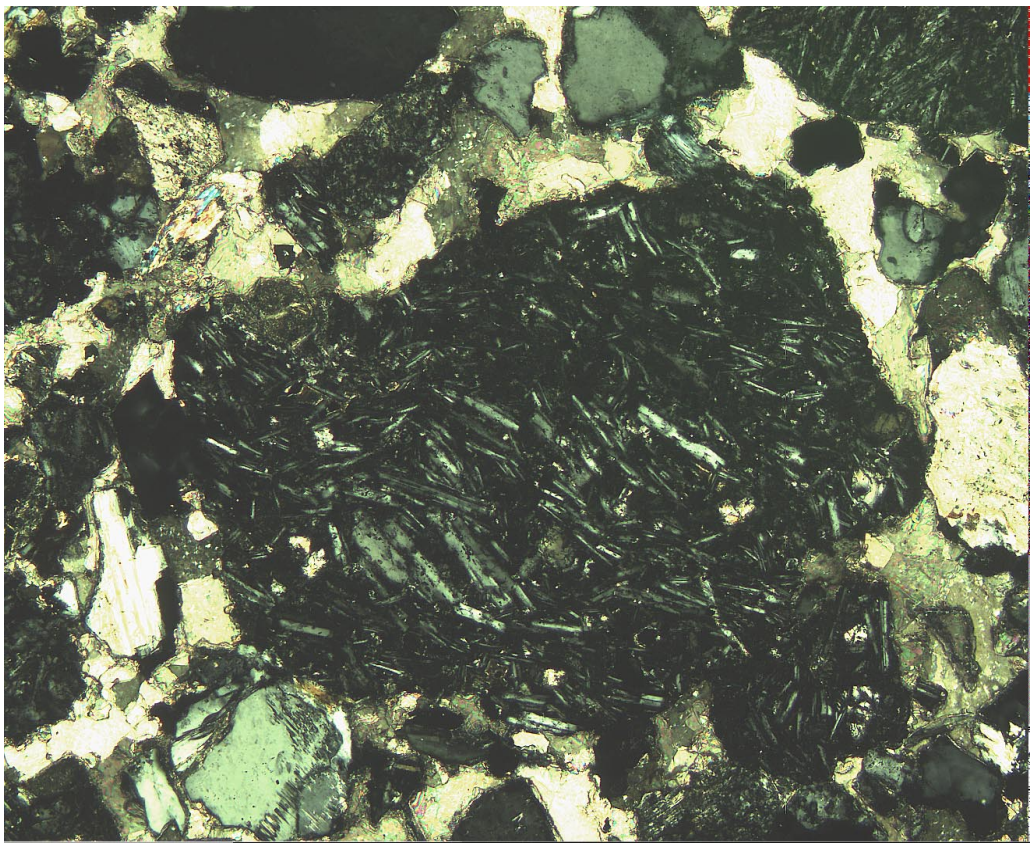

Figure F3. Digital photomicrograph (crossed nicols) of a subrounded acidic volcanic clast with feldspar phenocrysts set in a siliceous matrix; feldspar is sericitized and the rock includes secondary calcite. Surrounding grains are feldspar, quartz, and additional basaltic fragments. The matrix is micritic (interval 180-1116A-1R-1, 58–60 cm).

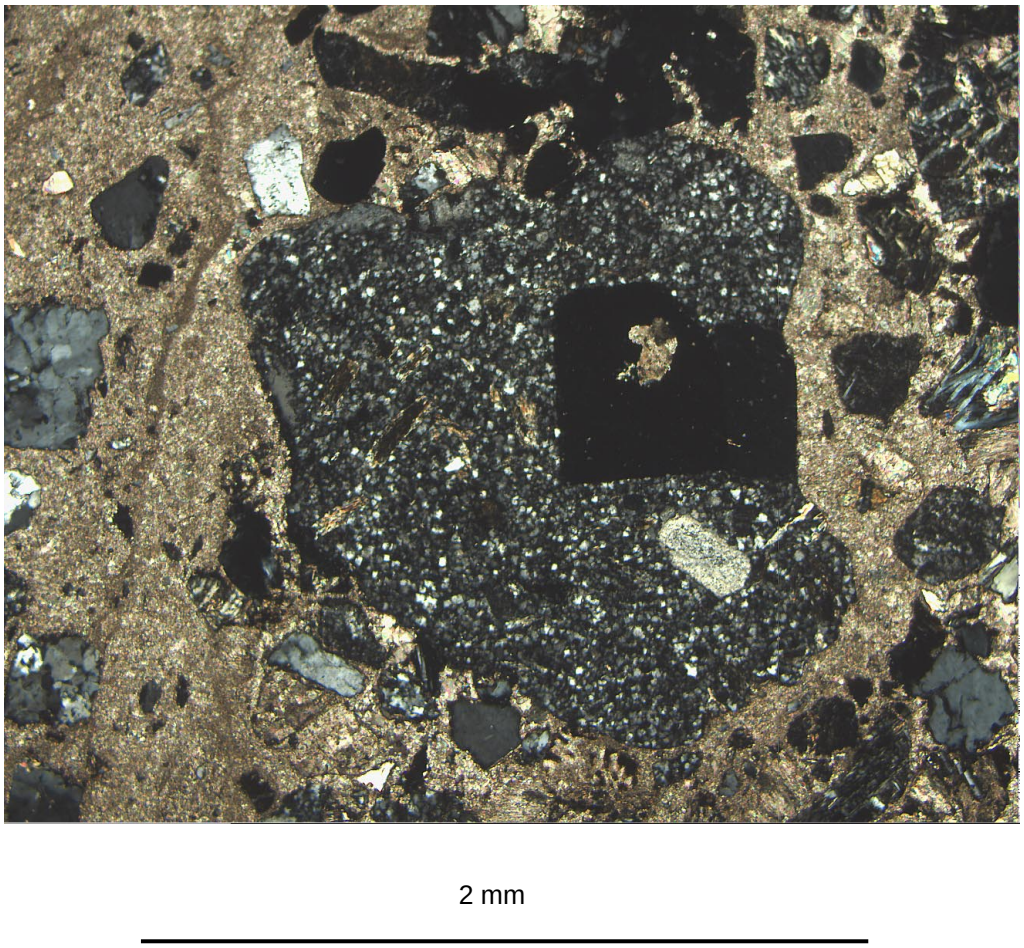

Figure F4. Digital photomicrograph (crossed nicols) of a rounded grain of serpentinite with adjacent acidic and basic extrusive grains, feldspar, and quartz. In addition, a small schist clast is present in the upper left quadrant. The cement is calcite spar (interval 180-1116A-1R-1, 58–60 cm).

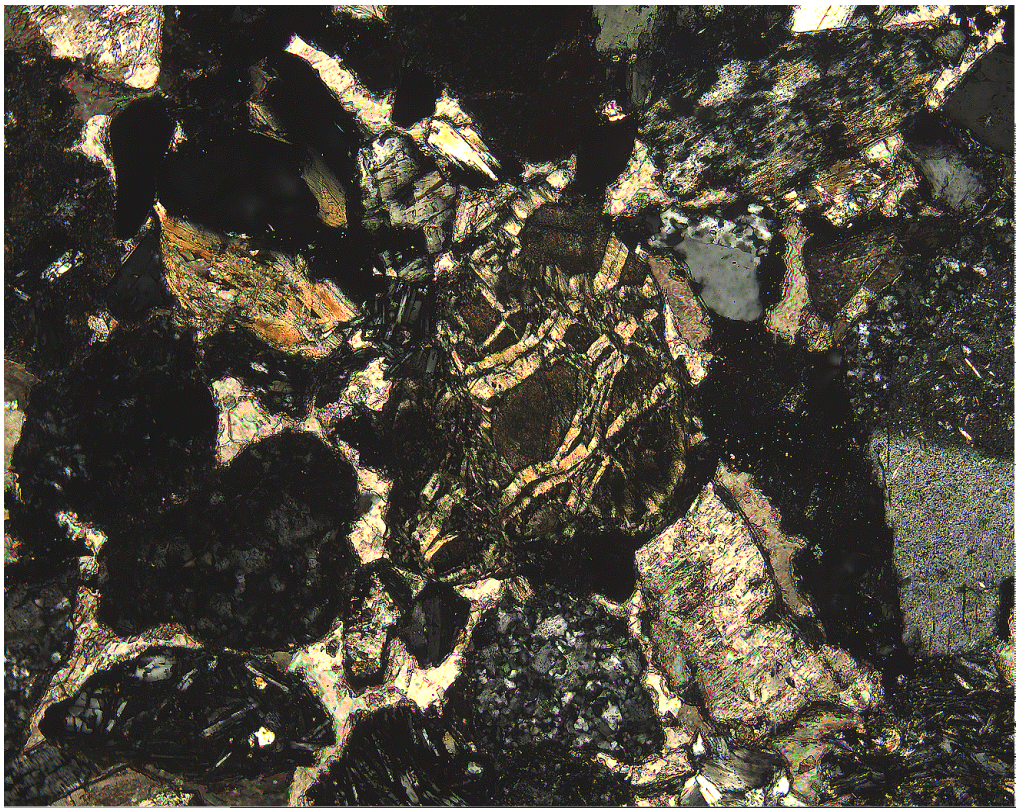

Figure F5. Digital photomicrograph (crossed nicols) of a subangular fragment of plutonic rock with intergrown quartz, feldspar, and biotite suggestive of a granitic source rock. Surrounding grains are subrounded to rounded grains of glassy basalt, quartz, and feldspar. There is a micritic matrix (interval 180-1116A-1R-1, 58–60 cm).

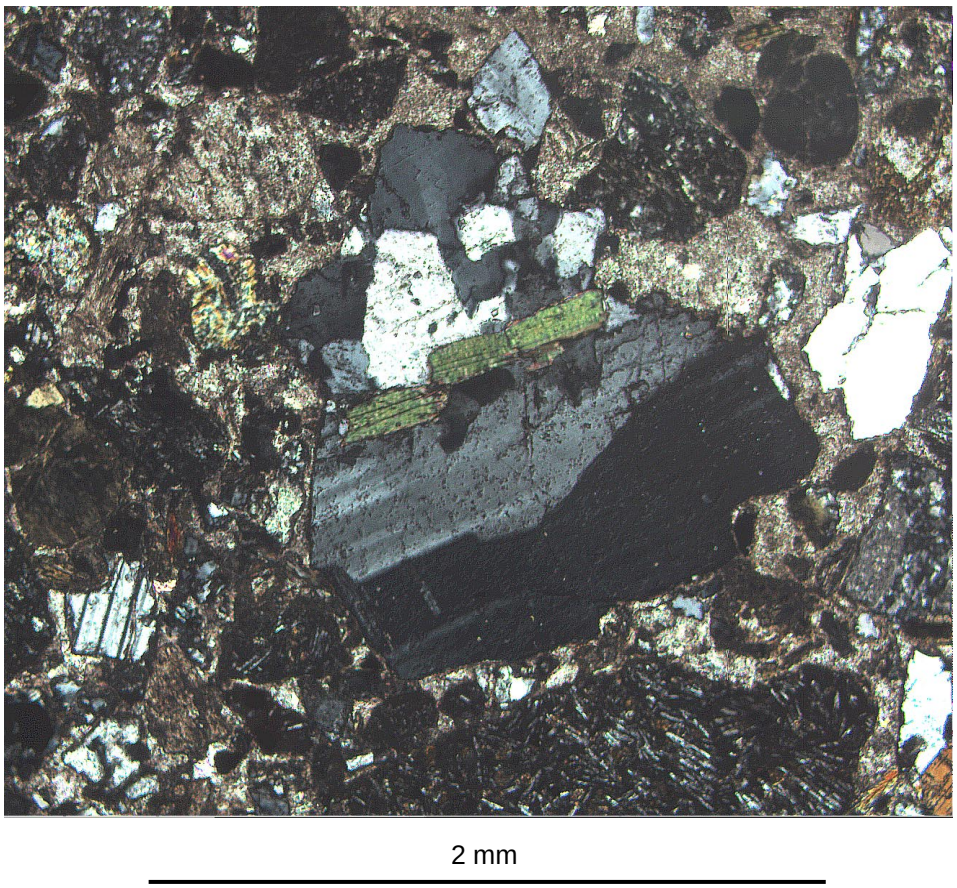

Figure F6. Graded laminae and thin beds of siltstone and very fine grained sandstone offset by small normal faults (interval 180-1116A-4R-2, 4–9 cm).

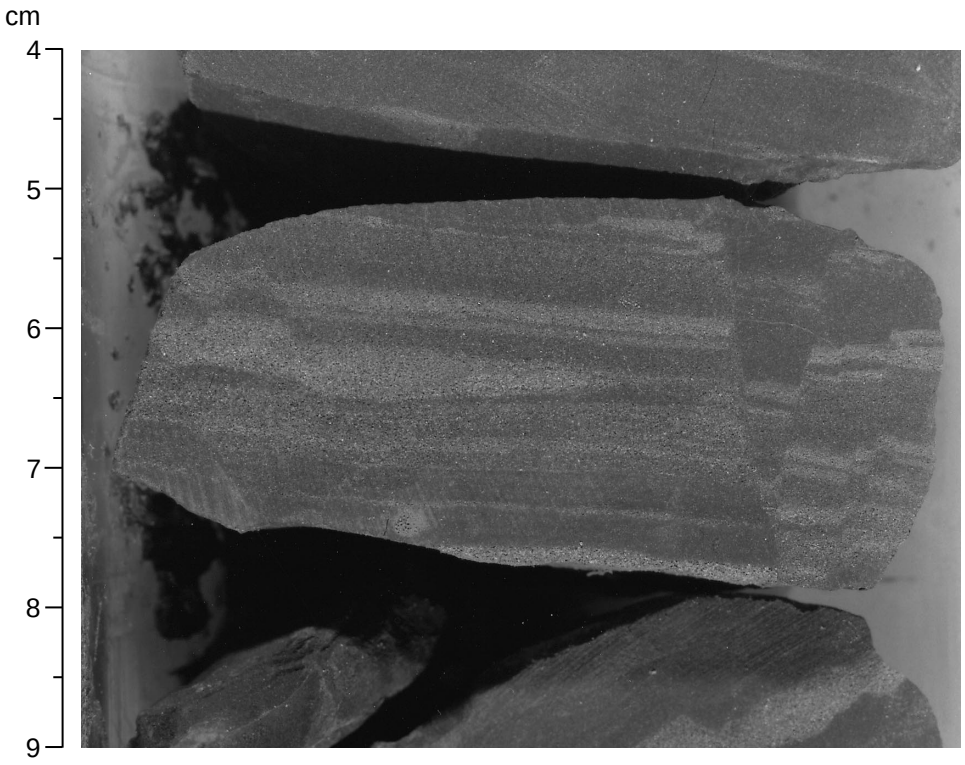

Figure F7. Strongly bioturbated silty claystone typical of the background hemipelagic sediment of interval 180-1116A-4R-1, 72–84 cm. Note the tectonically induced tilt of bedding.

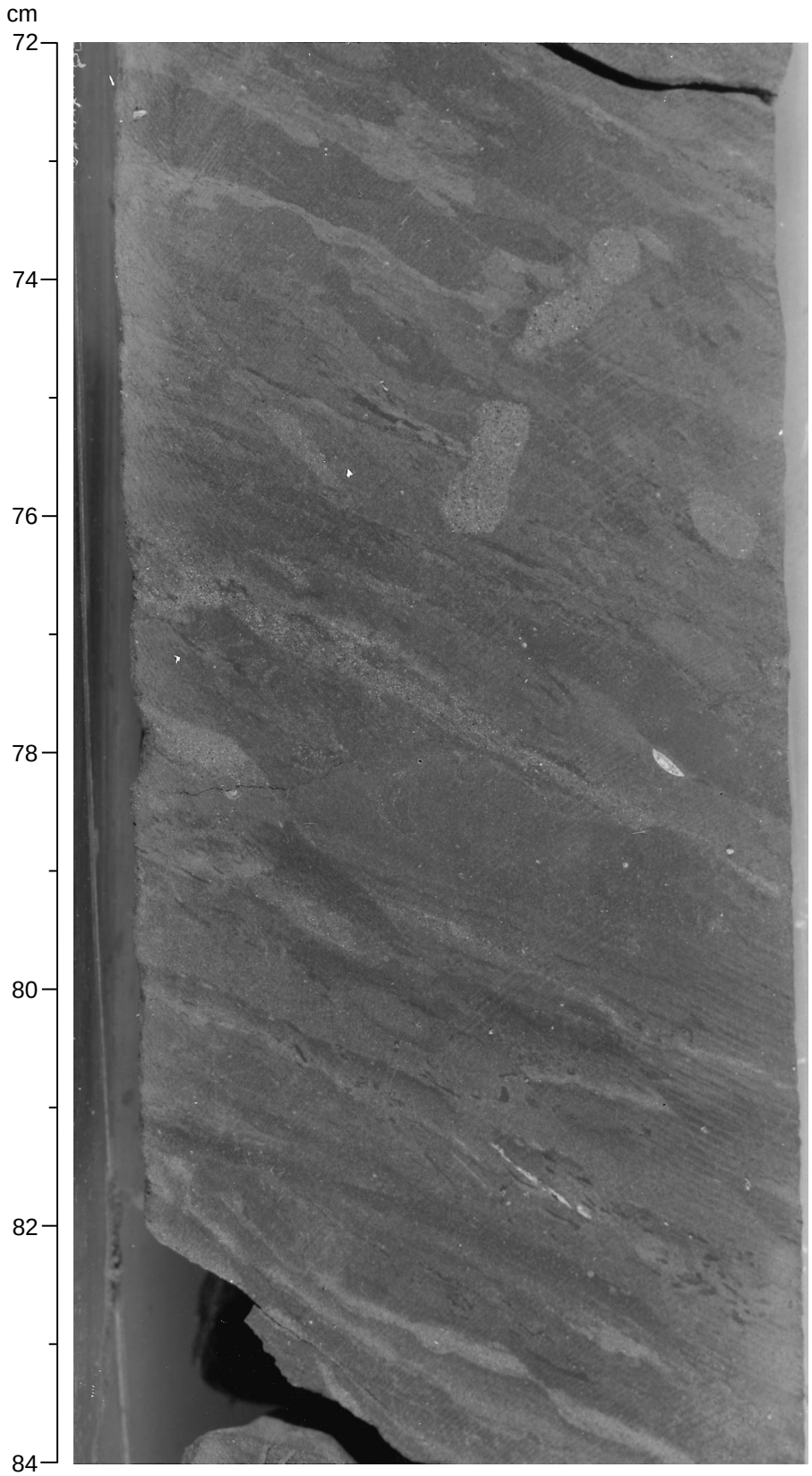

Figure F8. Dipping clayey siltstone with subvertical fluid injection structure filled with medium- to coarse-grained sandstone (interval 180-1116A-4R-2, 16–30 cm).

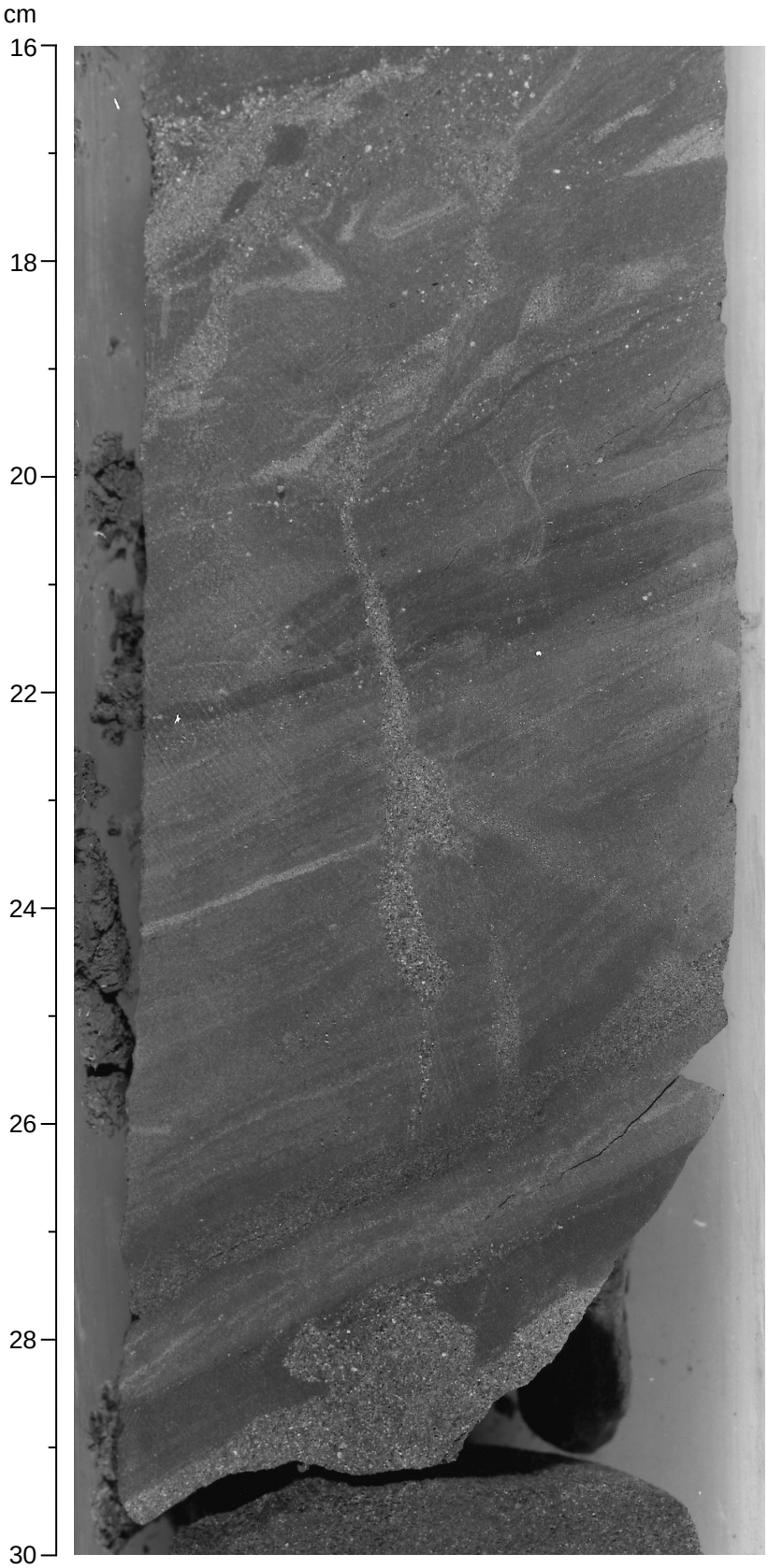

Figure F9. Poorly sorted, matrix-supported paraconglomerate, including angular to subangular clasts of various volcanic rocks (interval 180-1116A-7R-1, 38–62 cm).

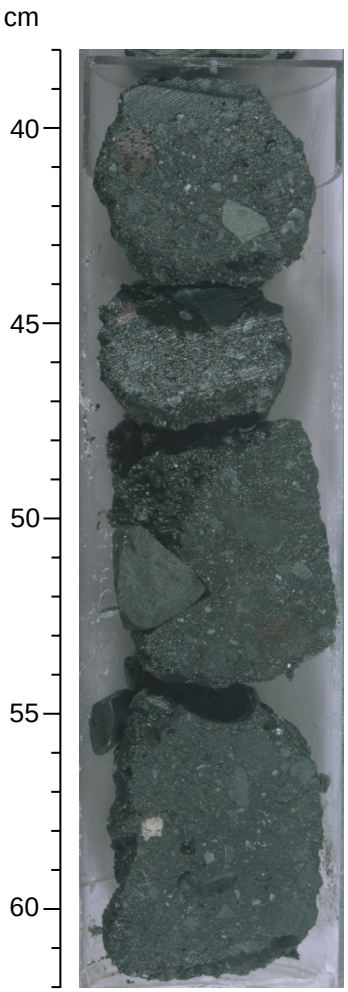

Figure F10. Digital photomicrograph (plane-polarized light) of a basic volcanic rock with abundant greenish yellow hornblende phenocrysts in a fine-grained groundmass of plagioclase laths, arranged in a trachytoidal texture, iron-ore, and glass—probably a hornblende andesite (interval 180-1116A-8R-1, 42–45 cm).

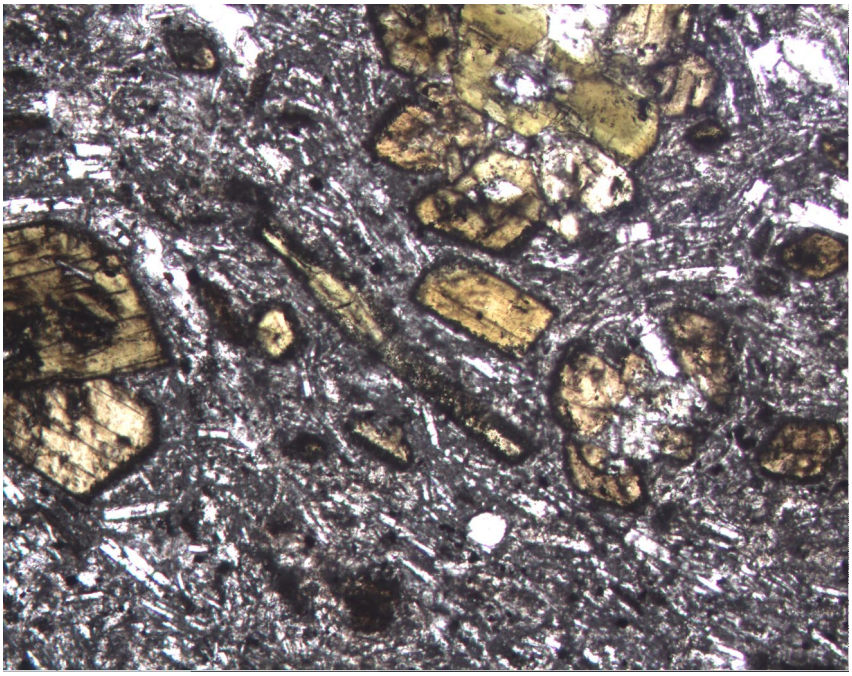

Figure F11. Digital photomicrograph (crossed nicols) of a basic volcanic rock with large phenocrysts of plagioclase, augite, and olivine (altered) in a fine-grained groundmass of plagioclase needles, ore, and glass (?) (interval 180-1116A-8R-1, 37–40 cm).

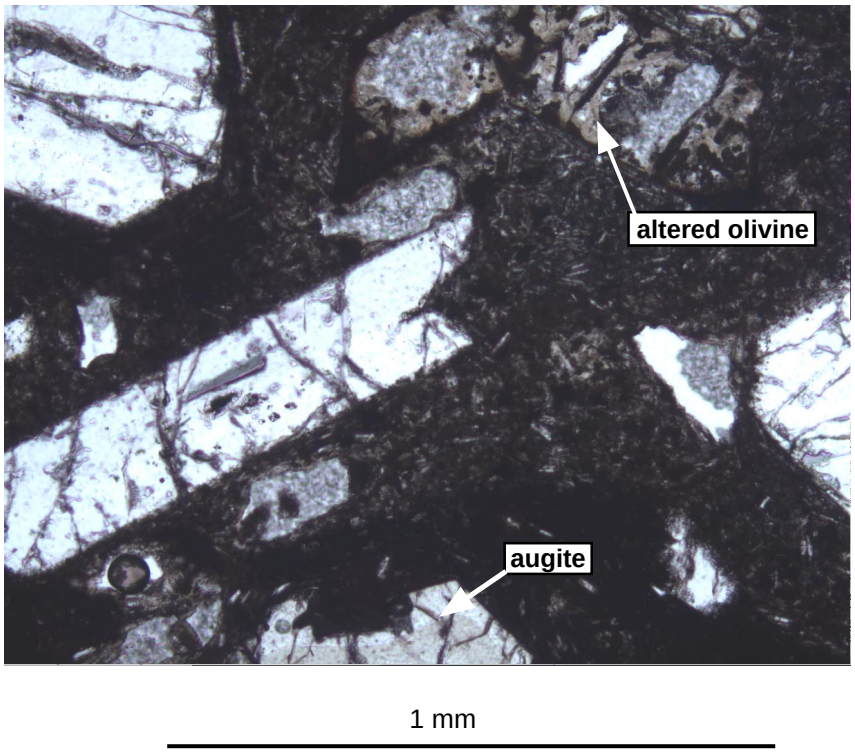

Figure F12. Digital photomicrograph (plane-polarized light) of a subrounded clast of glassy basalt with plagioclase and pyroxene phenocrysts set in a poorly sorted silty matrix with other basaltic fragments, quartz, and feldspar (interval 180-1116A-7R-1, 58–60 cm).

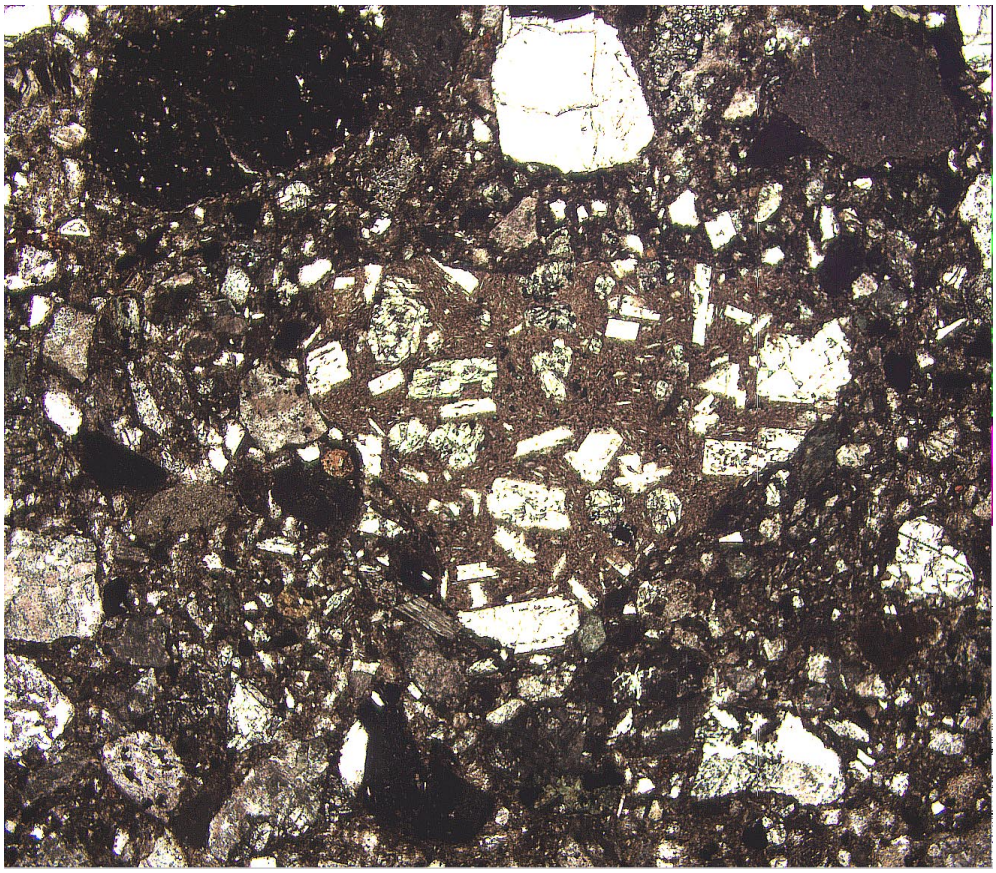

Figure F13. Digital photomicrograph (plane-polarized light) of a well-rounded clast of porphyritic basalt with a glassy matrix and phenocrysts of plagioclase and hornblende surrounded by rounded basic volcanic clasts, feldspar, quartz, and calcite; note benthic foraminifer near the top of the field of view (interval 180-1116A-8R-1, 37–40 cm).

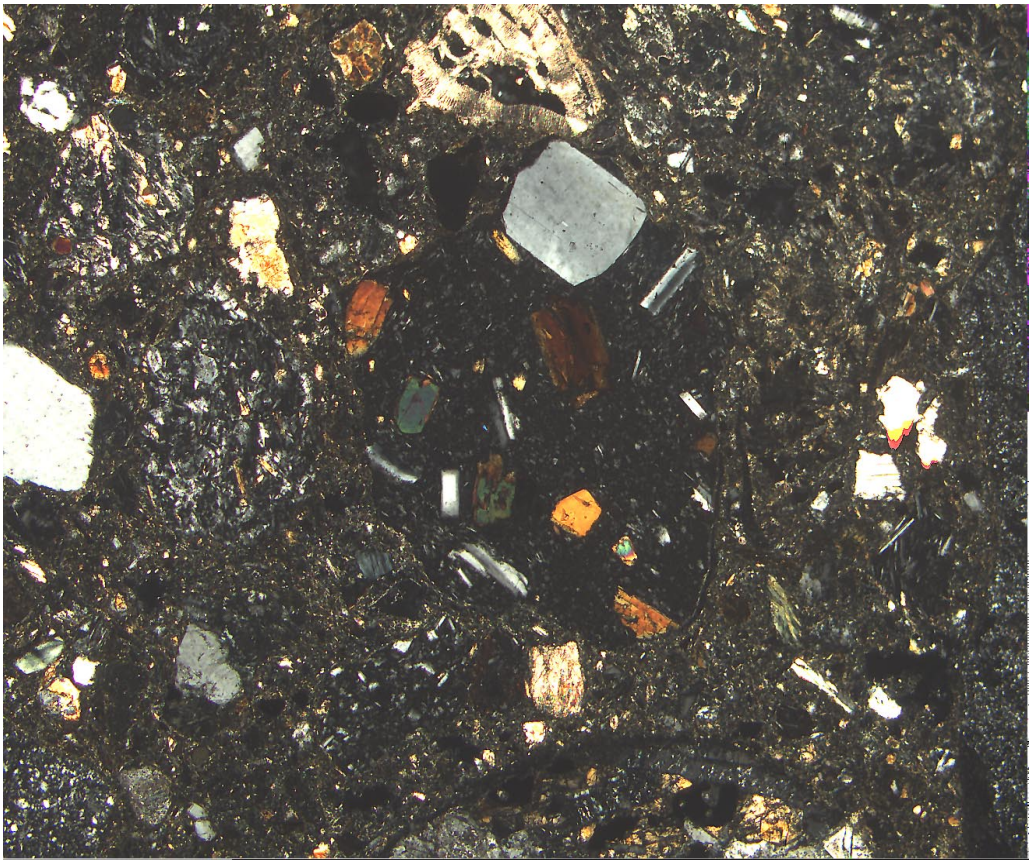

Figure F14. Faintly laminated coarse- to medium-grained sandstone (interval 180-1116A-15R-1, 56–70 cm).

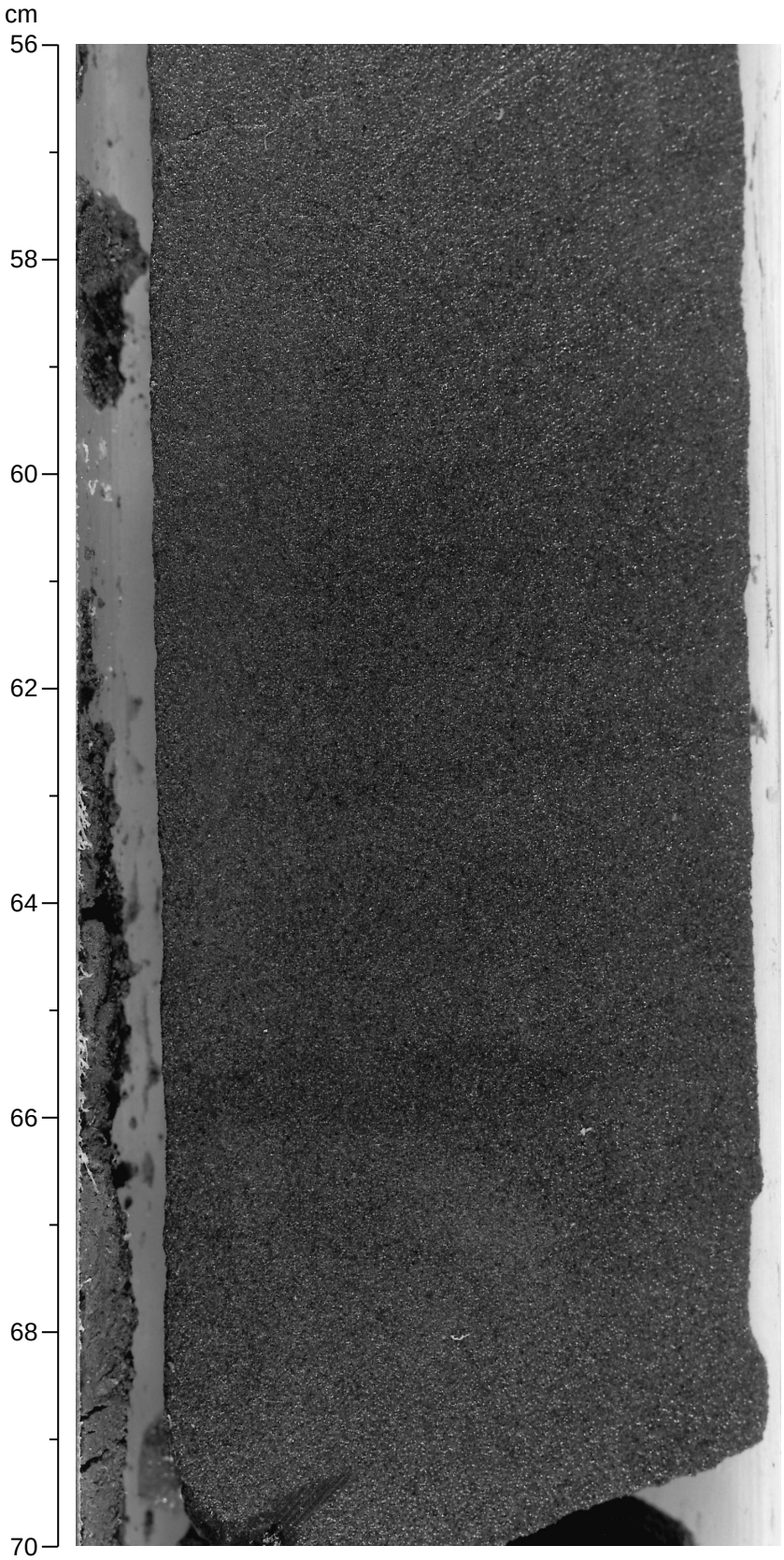

Figure F15. Well-developed climbing-ripple-laminated fine-grained sandstone, overlying wavy-laminated fine-grained sandstone (interval 180-1116A-17R-2,14–24 cm).

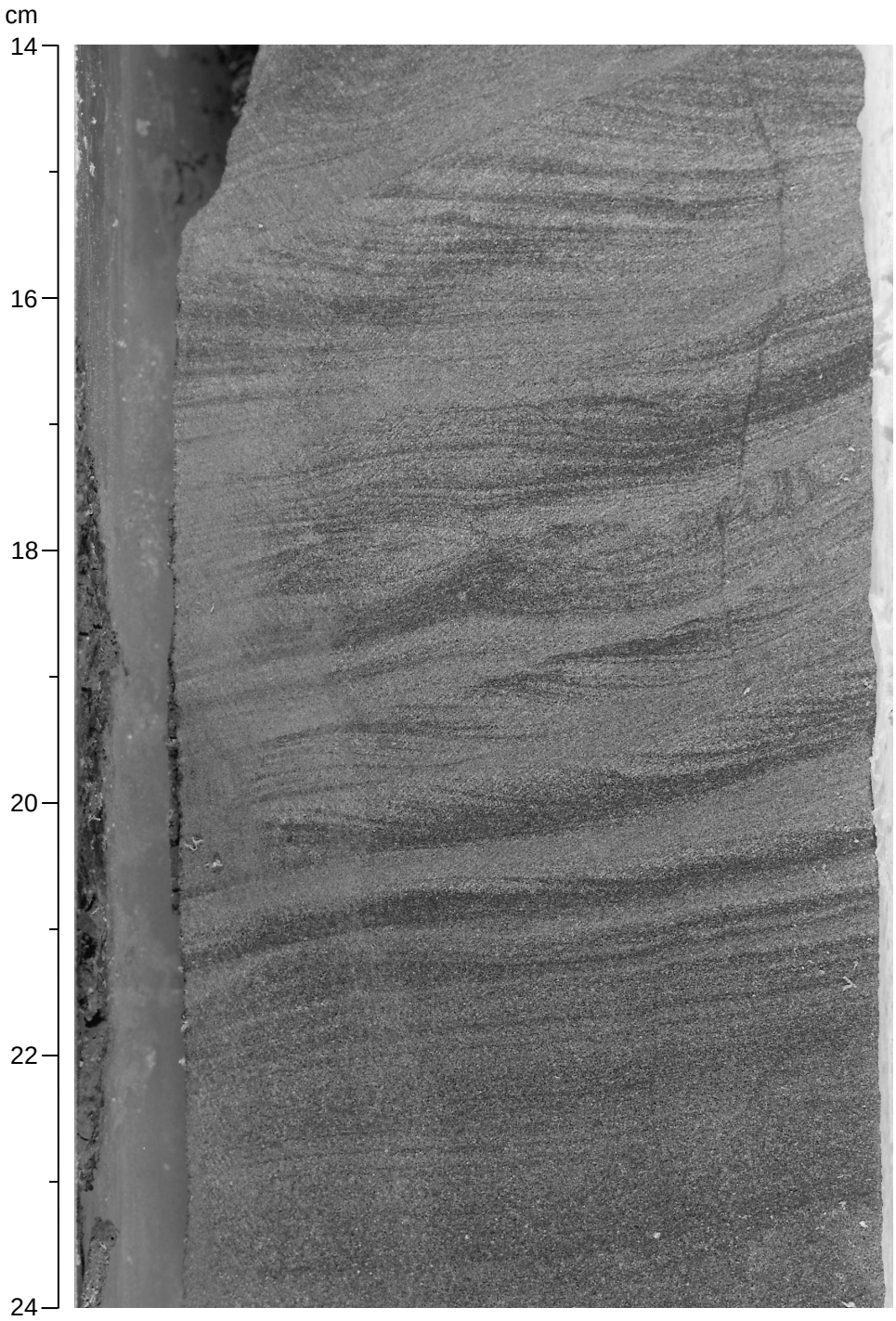

Figure F16. Silty claystone sharply overlain by ripple- and wavy-laminated fine-grained sandstone the upper part of which comprises several graded laminae with local well-developed flame structures. Above the sandstone is faintly laminated silty claystone (dark) (interval 180-1116A-16R-2, 55–76 cm).

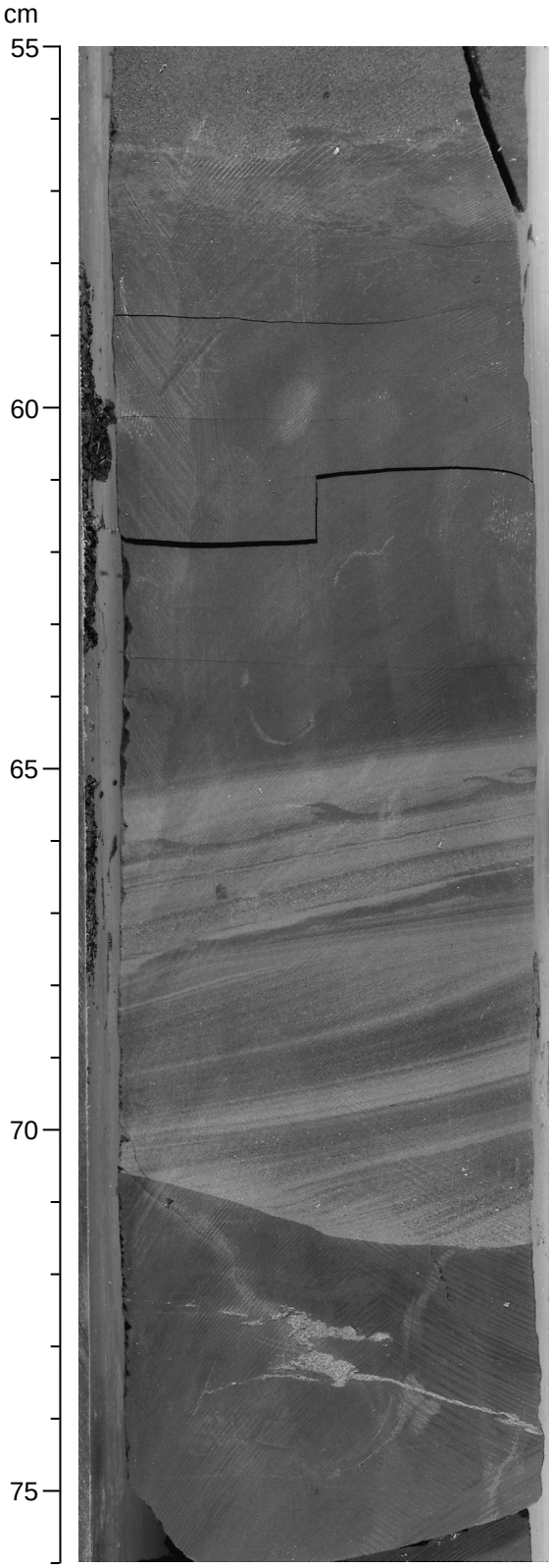

Figure F17. Wavy and inclined laminae of fine sandstone and convolute lamination grading upward into wavy lamination (interval 180-1116A-9R-1, 104–140 cm).

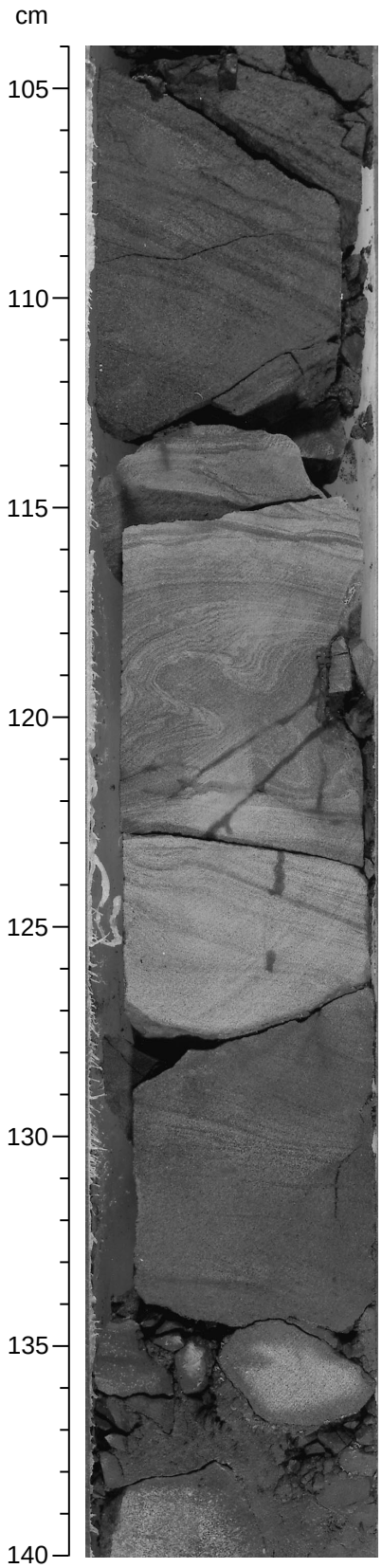

Figure F18. Core Photograph. Three beds: (lower) bioturbated silty claystone; (middle) sharply overlying fine- to medium-grained sandstone with cross lamination near the base and wavy/inclined lamination above this; (upper) poorly sorted coarse-grained sand with a mudstone rip-up clast. Tectonic calcite-filled veins are also present (interval 180-1116A-16R-2, 1–30 cm).

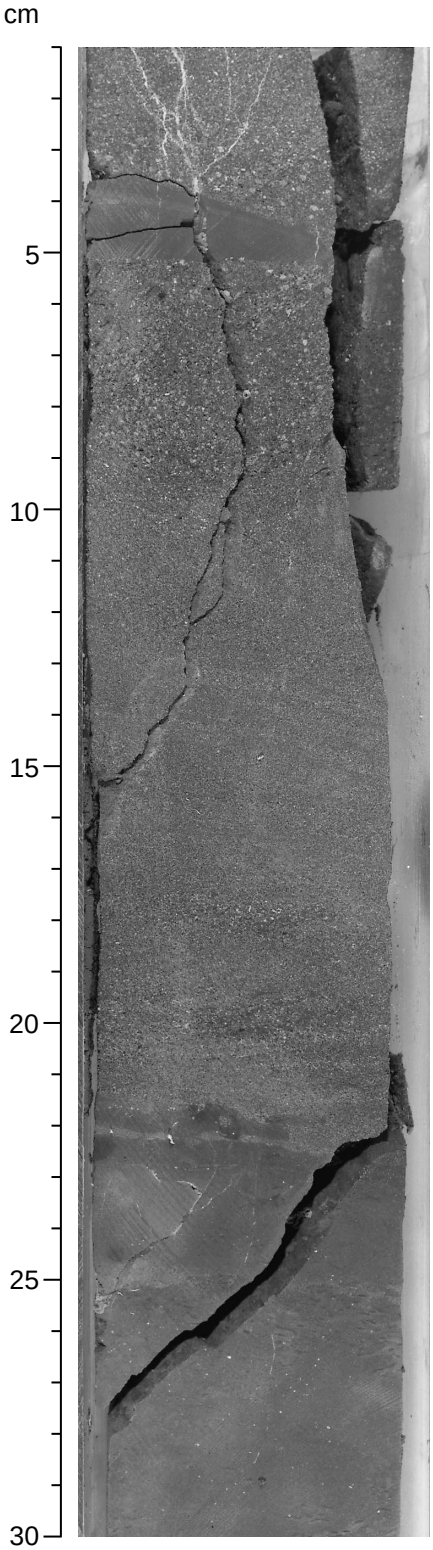

Figure F19. Complex sand injection into clayey siltstone. See "Lithostratigraphic Unit III," p. 8, for discussion of the processes involved (interval 180-1116A-16R-2, 80–105 cm).

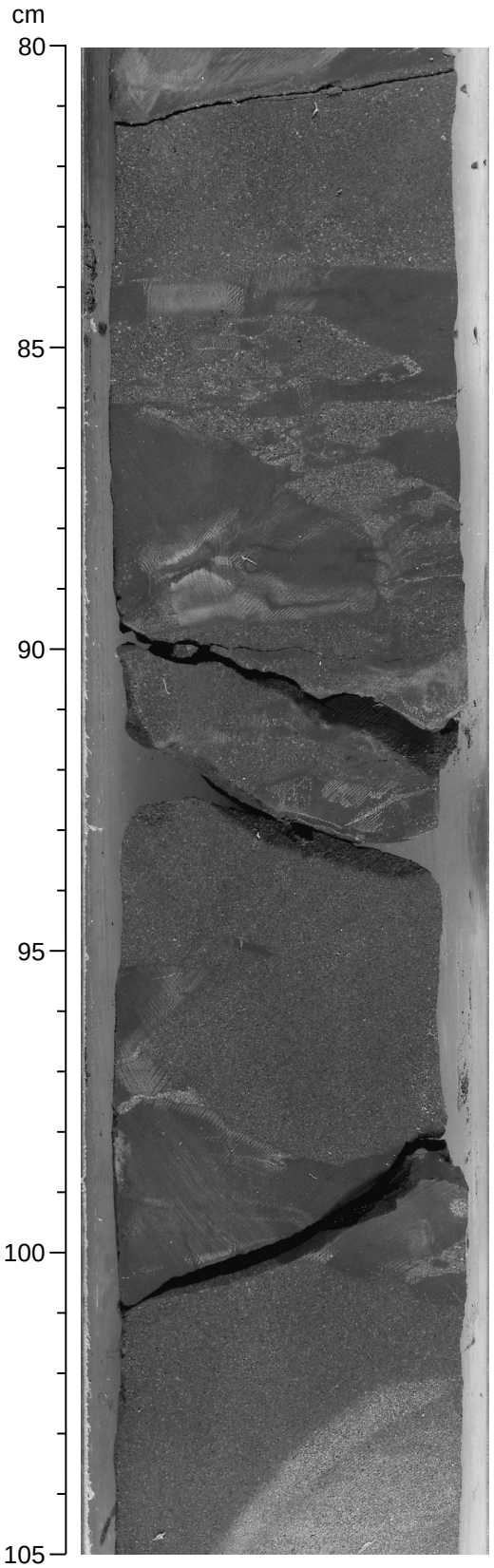

Figure F20. Digital photomicrograph (crossed nicols) of an angular fragment of calc-schist surrounded by glassy basalt and acidic volcanic fragments set in a sparry calcite cement (interval 180-1116A-13R-2, 25–27 cm).

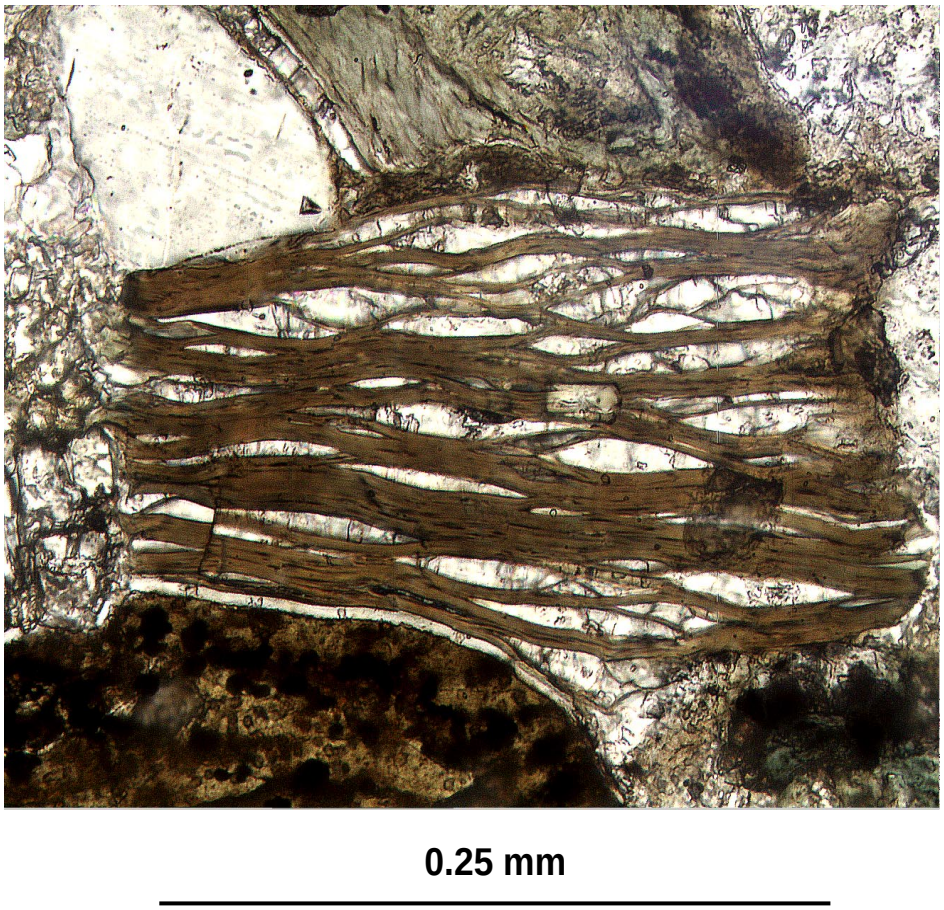

Figure F21. Thin, inclined sand-injection structure within silty claystone. See "Lithostratigraphic Unit III," p. 8, for discussion of the processes involved (interval 180-1116A-16R-3, 53–60 cm).

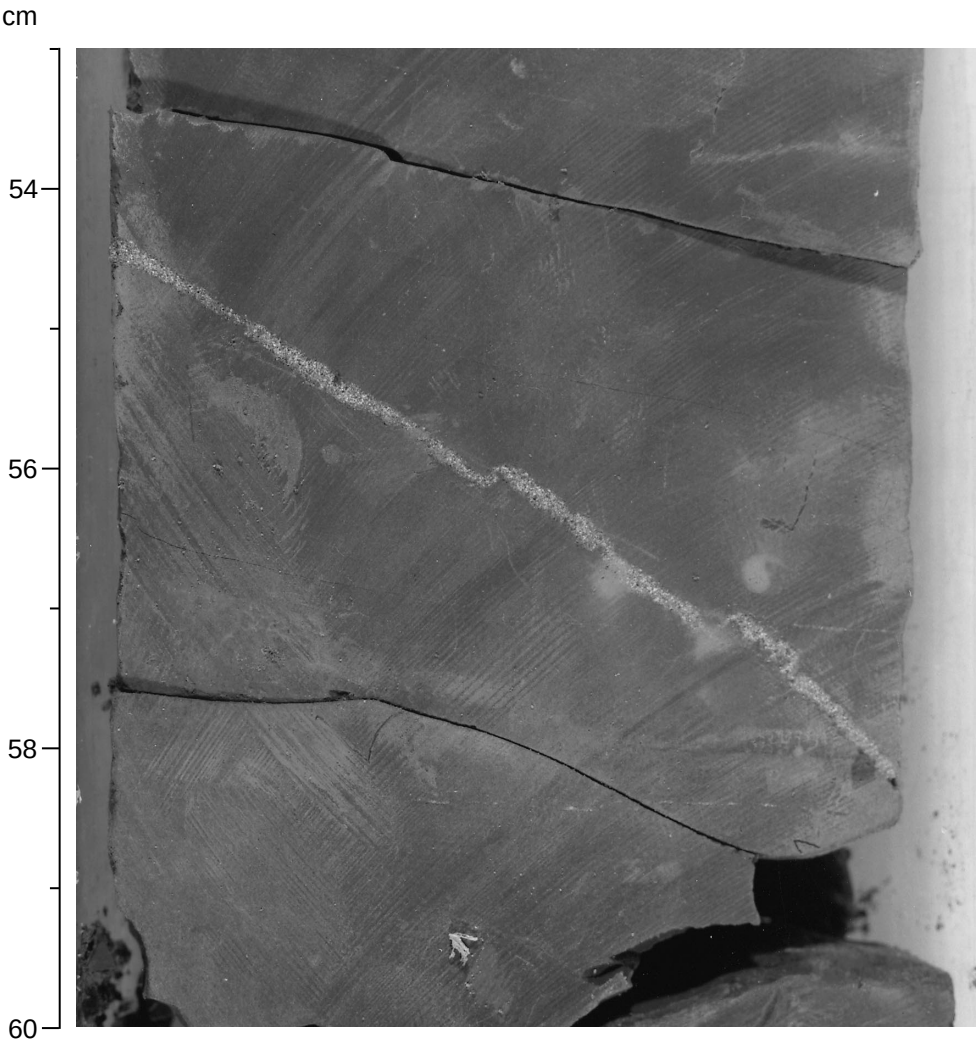

Figure F22. Summary of the main structural features observed at Site 1116. (For key to symbols, see Fig. F2, p. 52, in the "Explanatory Notes" chapter.)

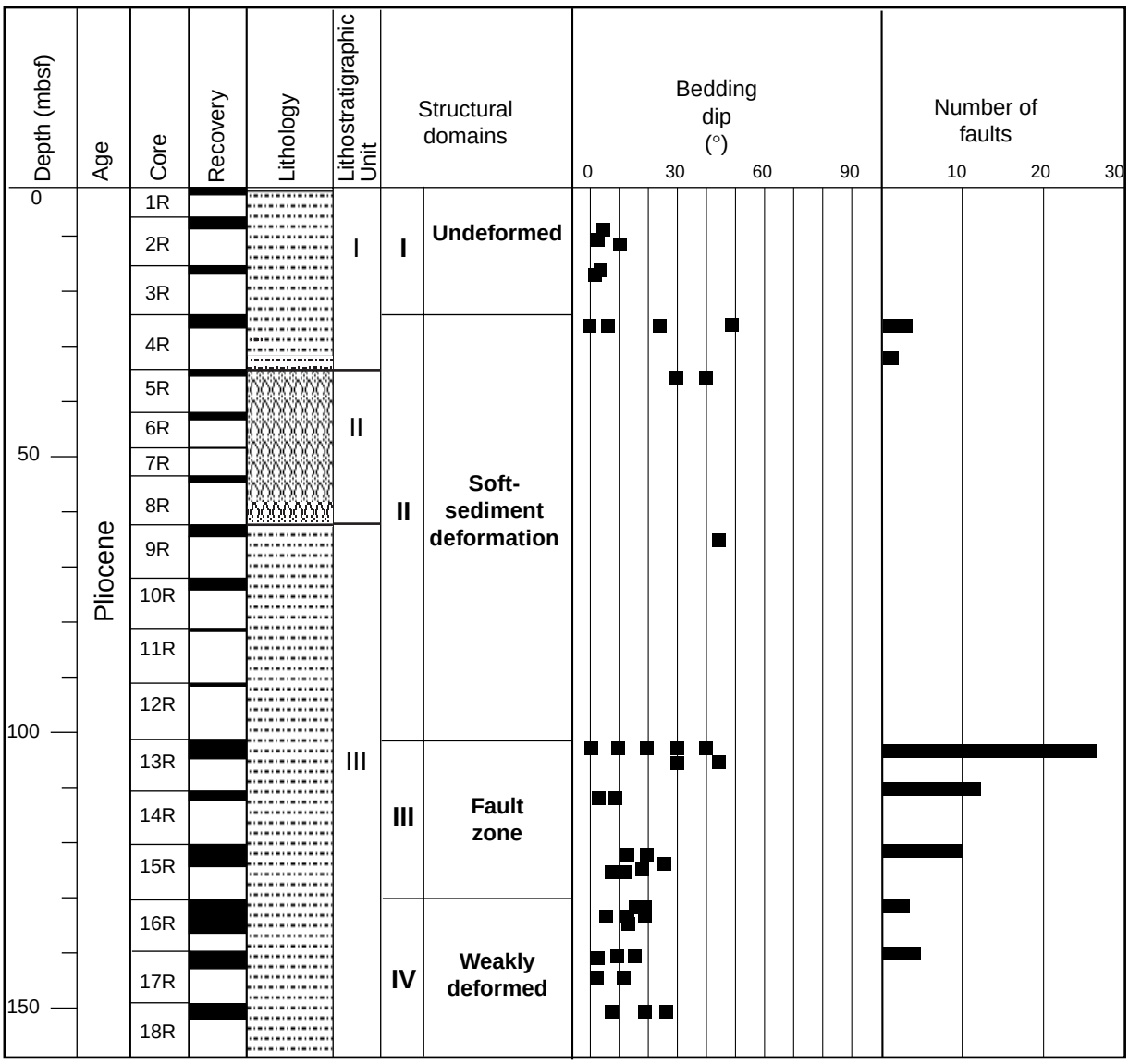

Figure F23. Histogram of bedding dip measurements in Hole 1116A. N = number of measurements.

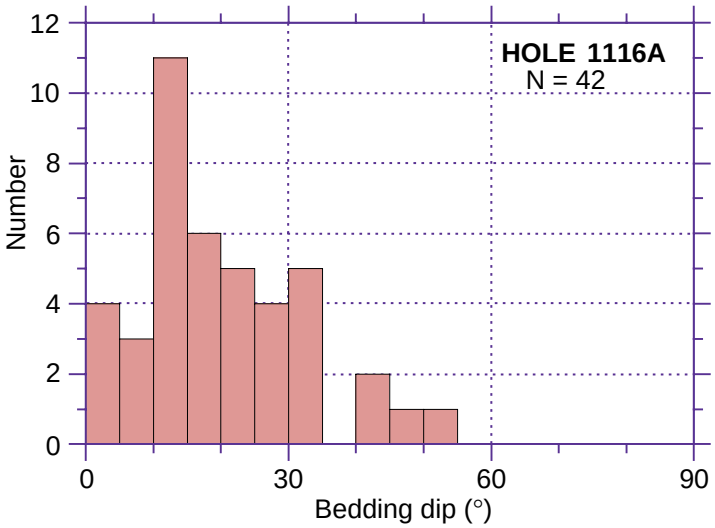

Figure F24. A. Example of early gravitational deformation in a well-laminated sequence (interval 180-1116A-4R-1, 90–130 cm [25.1–25.5 mbsf]). **B.** Interpretative sketch. W = west; E = east. Note that the base of the slump fold structure is sharply truncated by low-angle sliding surfaces.

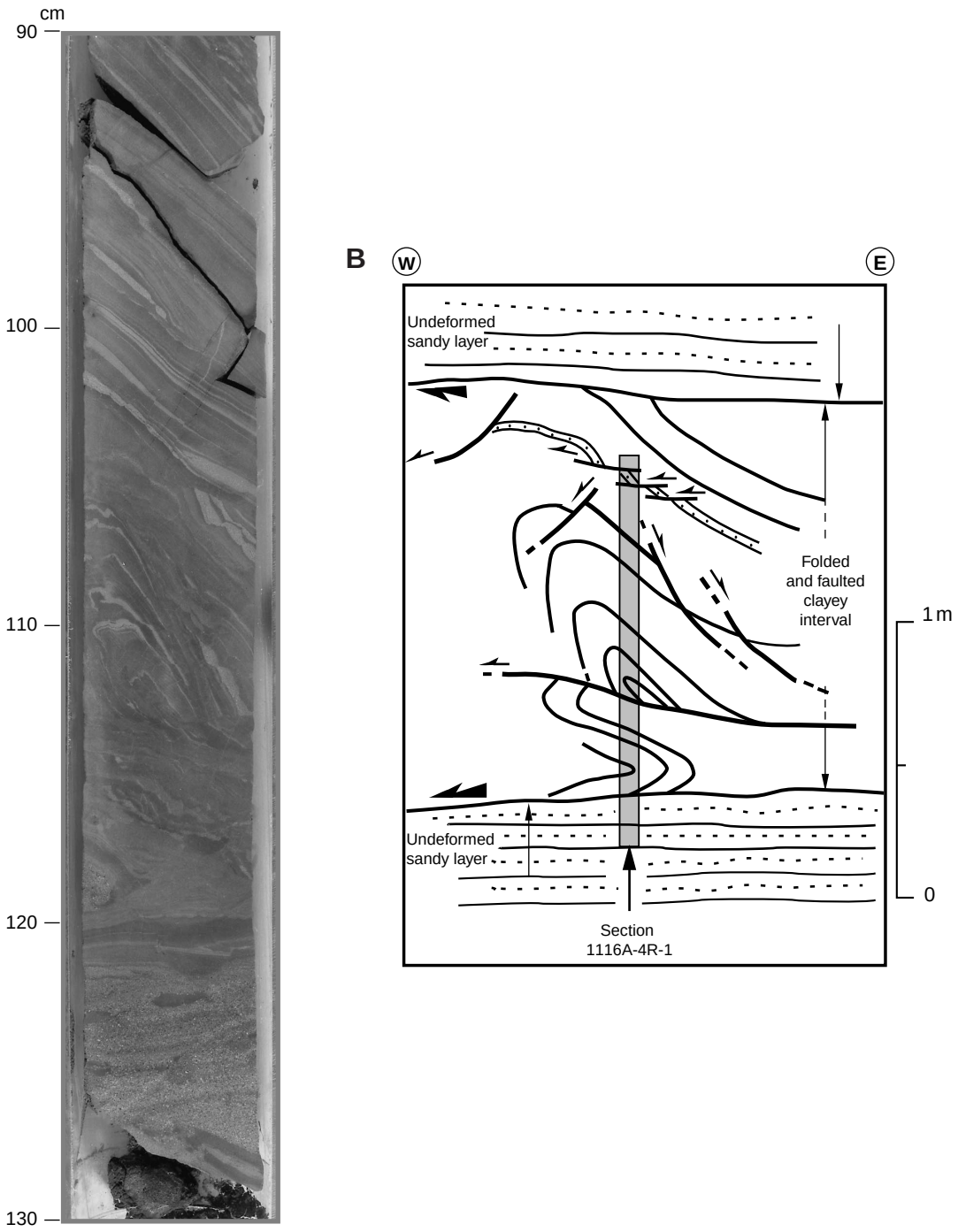

Figure F25. Example of steep normal microfaults at interval 180-1116A-4R-2, 5–8 cm (25.74–25.80 mbsf). F = strike and dip of fault in core reference frame.

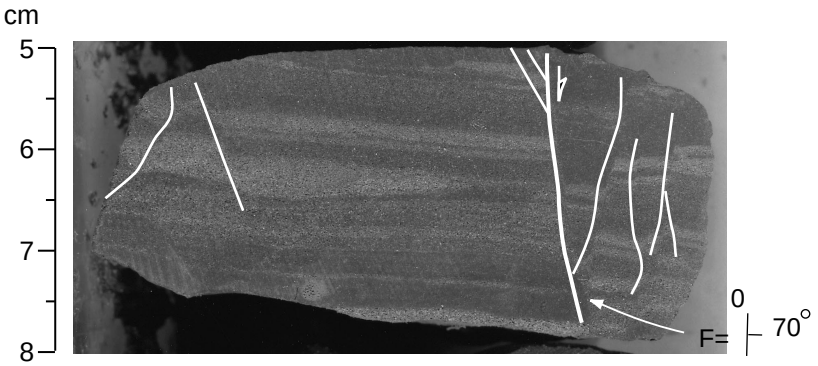

Figure F26. Fault measurements in Domain III (101.0–130.0 mbsf, Sections 180-1116A-13R-1 to 15R-2). **A.** Fault dip histogram. **B.** Plot of fault dip vs. slickenside plunge. SS = strike slip; OS = oblique slip; DS = dip slip; N = number of measurements.

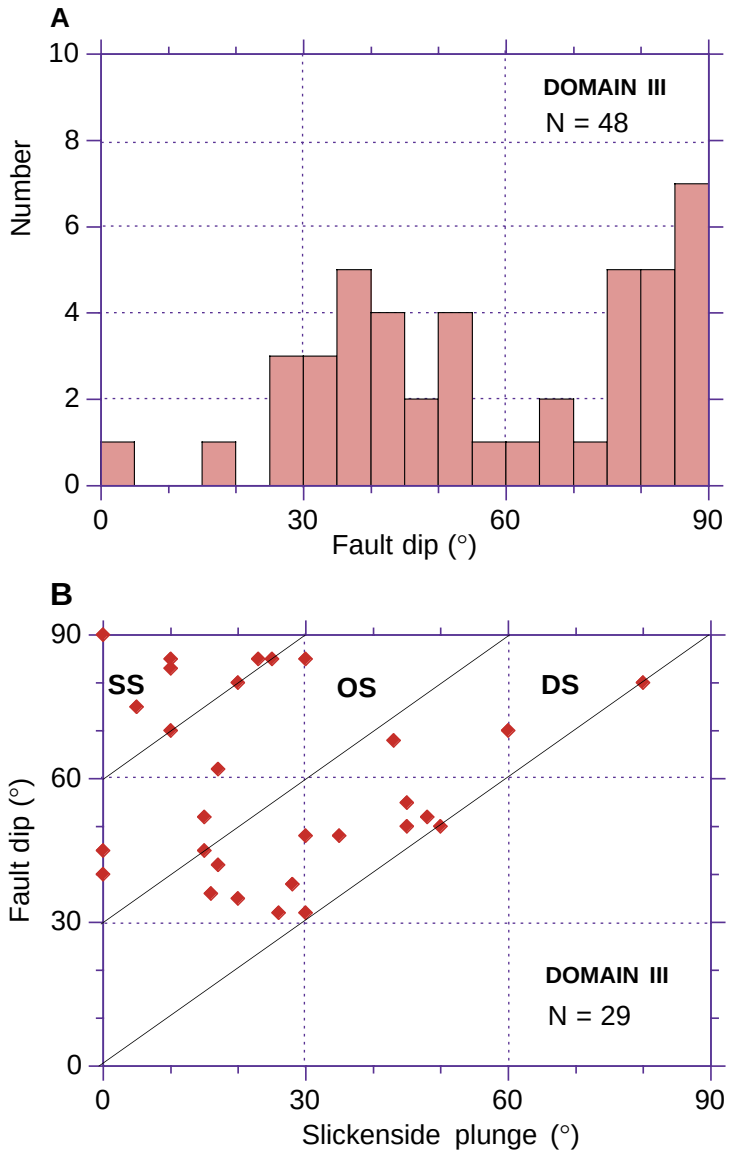

Figure F27. A. Example of steep sigmoidal normal fault locally filled with calcite in a curved relay zone (interval 180-1116A-15R-2, 90–107 cm [122.37–122.56 mbsf]). **B.** Schematic of top portion of the same section to show fault (F) and bedding (B) orientation and dip (in core reference frame).

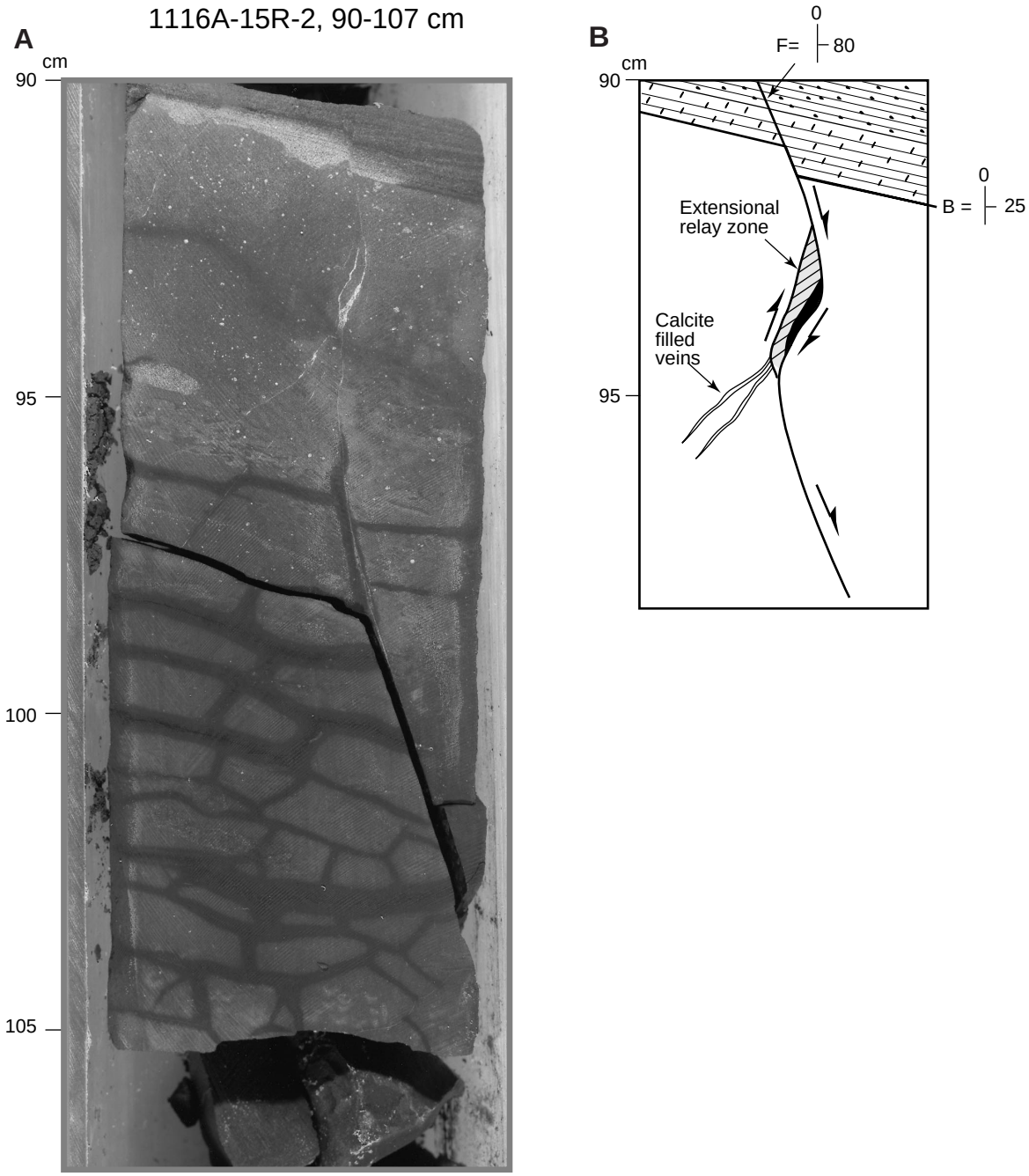

Figure F28. Histogram of bedding dips in Domain IV. N = number of measurements.

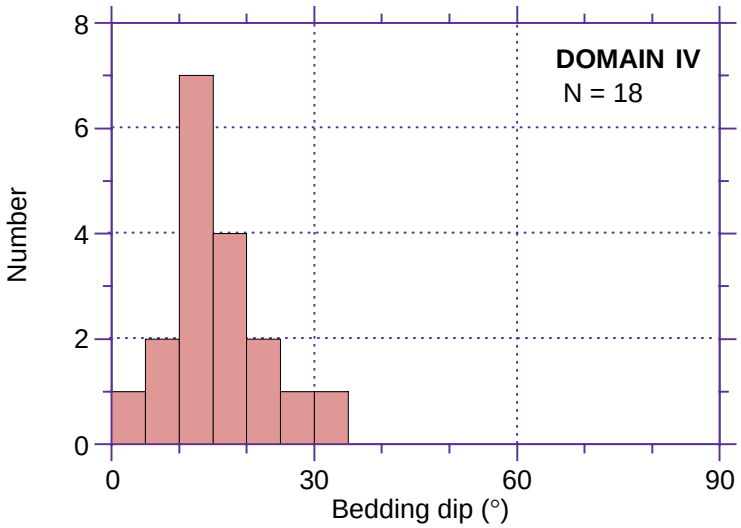

Figure F29. Biostratigraphic units and ages for Hole 1116A. Dashed lines indicate the true zonal boundary may lie above or below the indicated level.

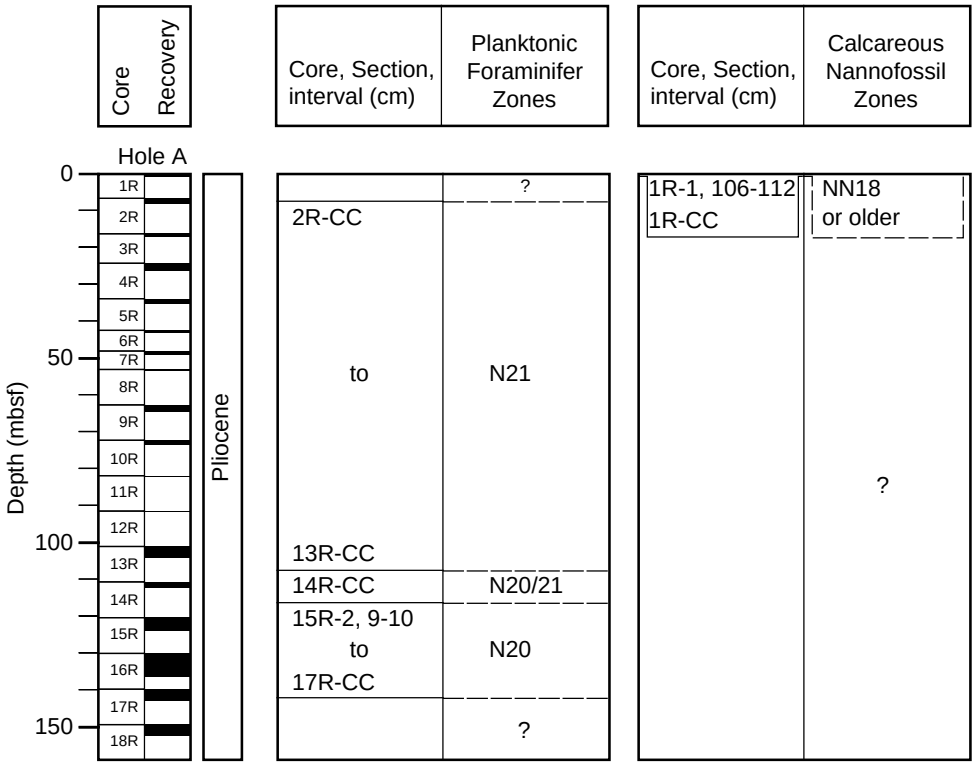

Figure F30. Age-depth relationship at Site 1116, based on nannofossil and planktonic foraminifers.

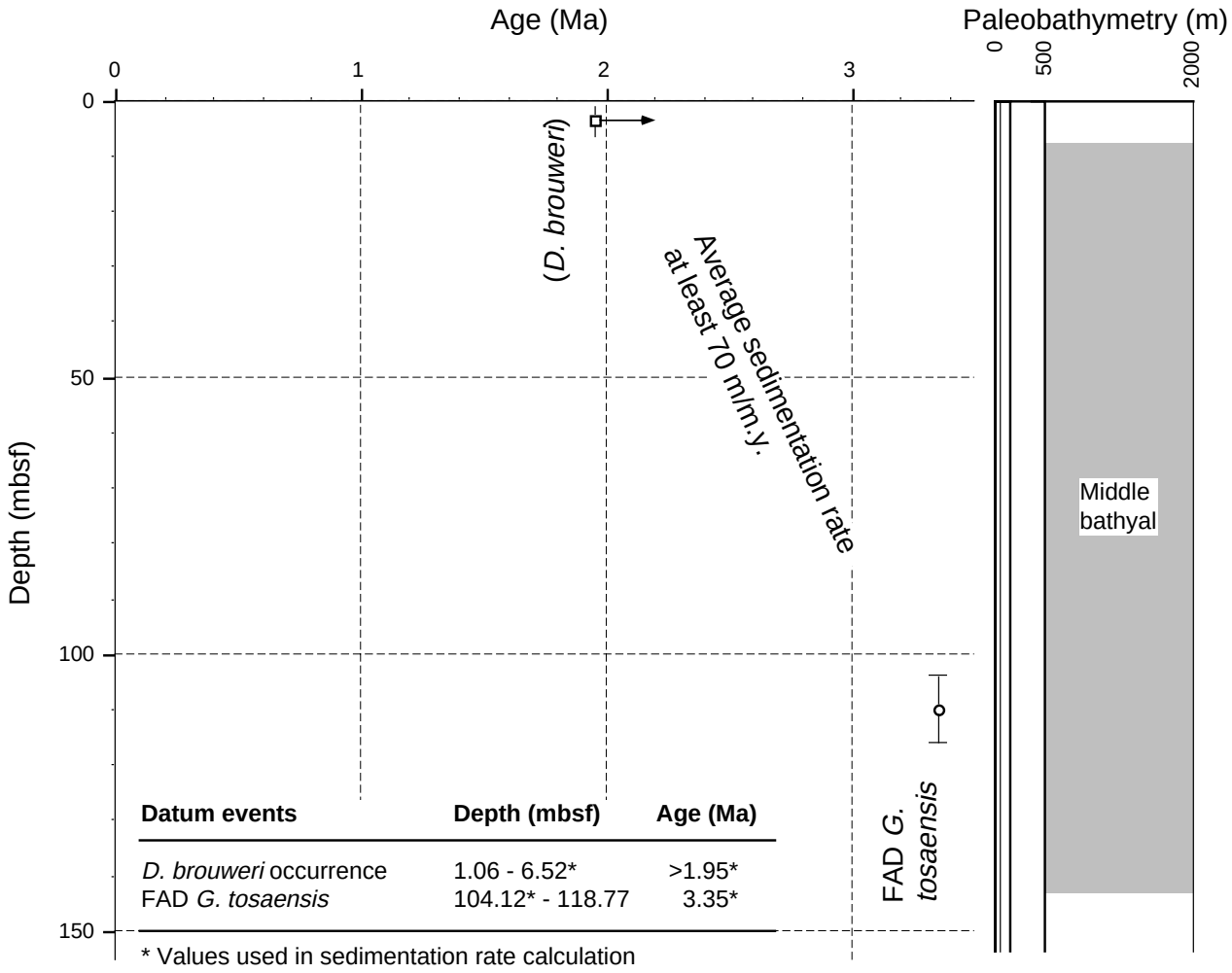

Figure F31. Susceptibility data (uncorrected for volume) from MST and AMST measurements of long cores from Site 1116.

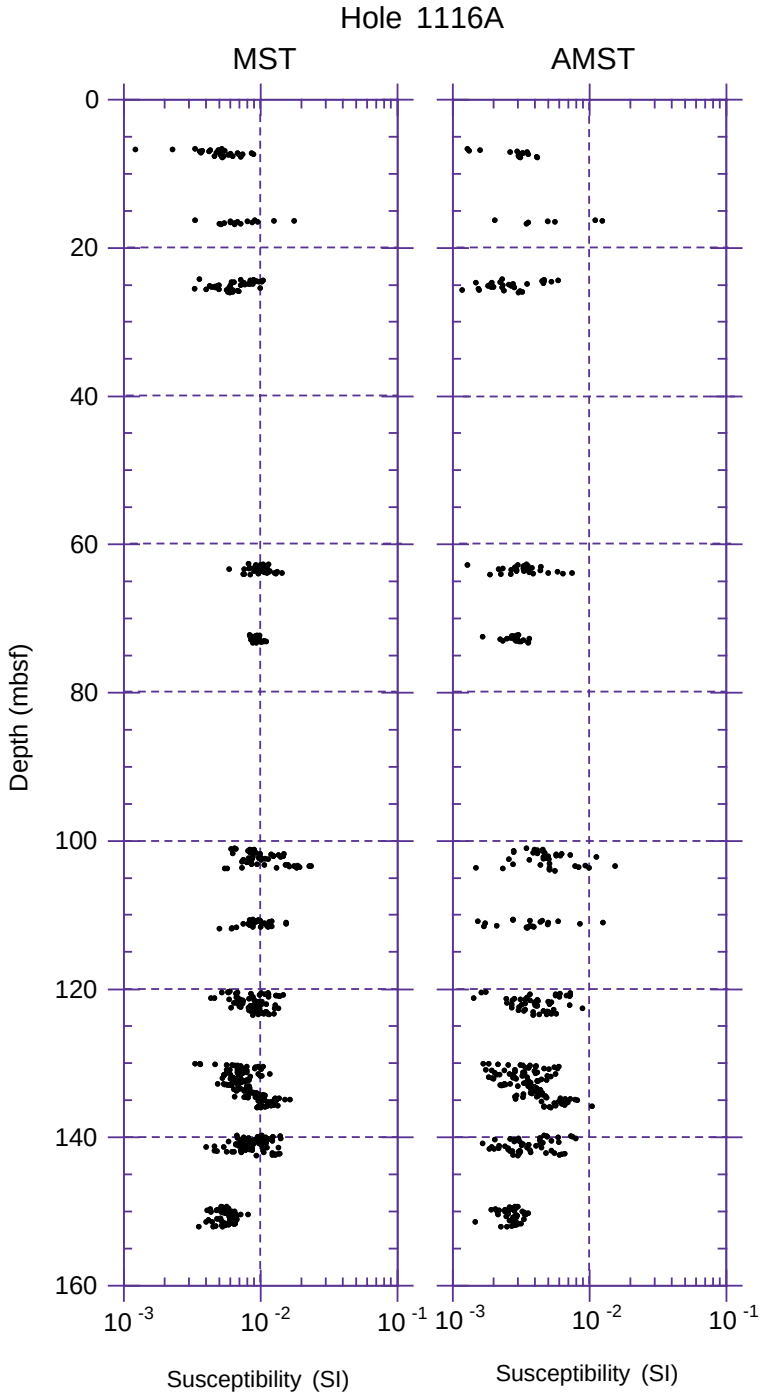

Figure F32. Susceptibility and its anisotropy (AMS) data from discrete sample measurements. **A.** Downhole variation in AMS parameters. Degree of anisotropy (P_j) and shape parameter (T) calculated according to Jelinek (1981). K_{max} and K_{min} are the maximum and minimum axes, respectively, of the susceptibility ellipsoid, and are shown corrected for bedding tilt as solid circles and squares; uncorrected data are shown as open circles and squares. (Continued on next page.)

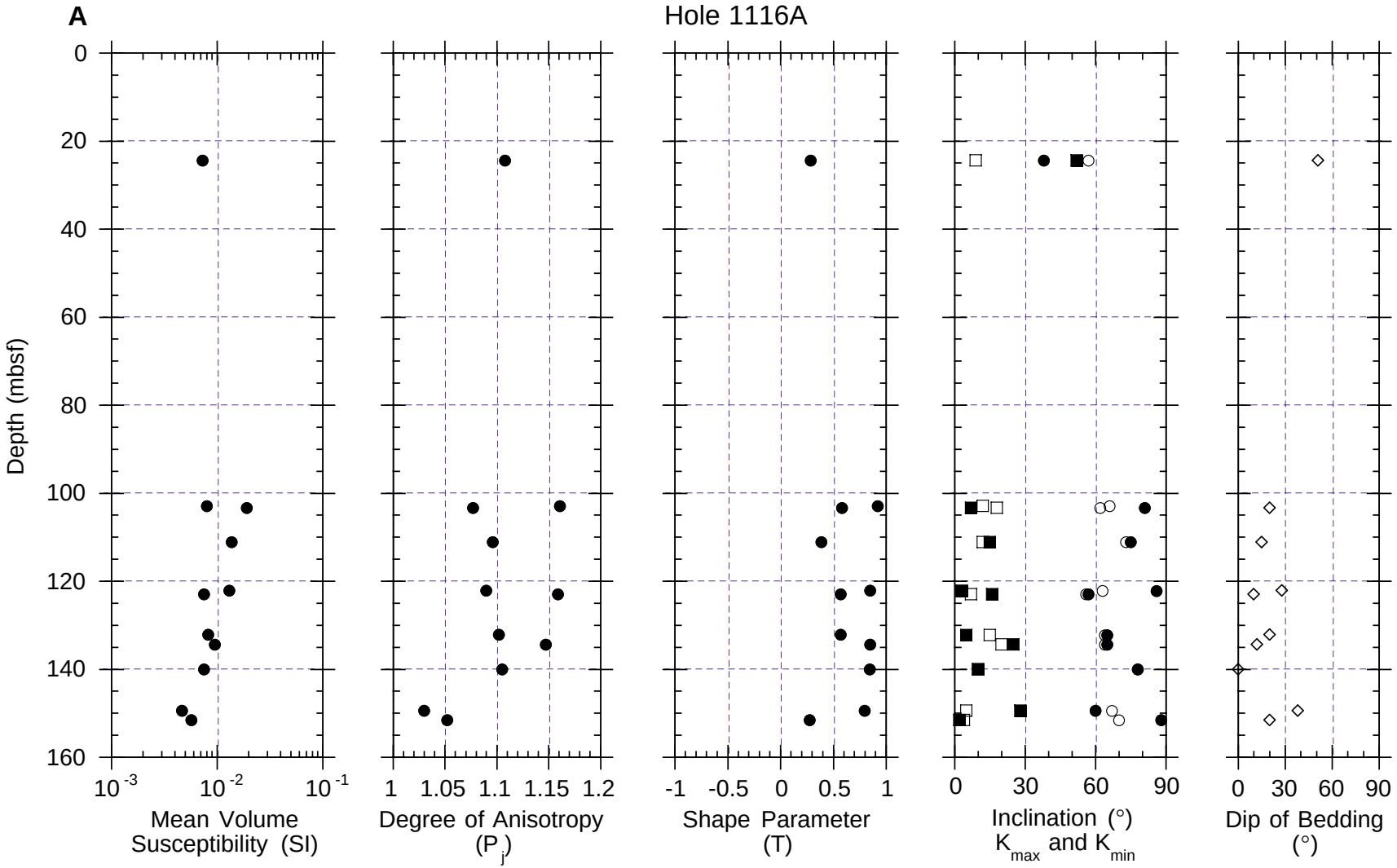

Figure F32 (continued.) B. Stereonet plots of the principal axes of the susceptibility ellipsoids corrected for bedding tilt and for core orientation. All symbols are projections on the lower hemisphere; open symbols used to highlight Sample 180-1116A-4R-1, 24–26 cm, which was the only sample from the upper part of the hole.

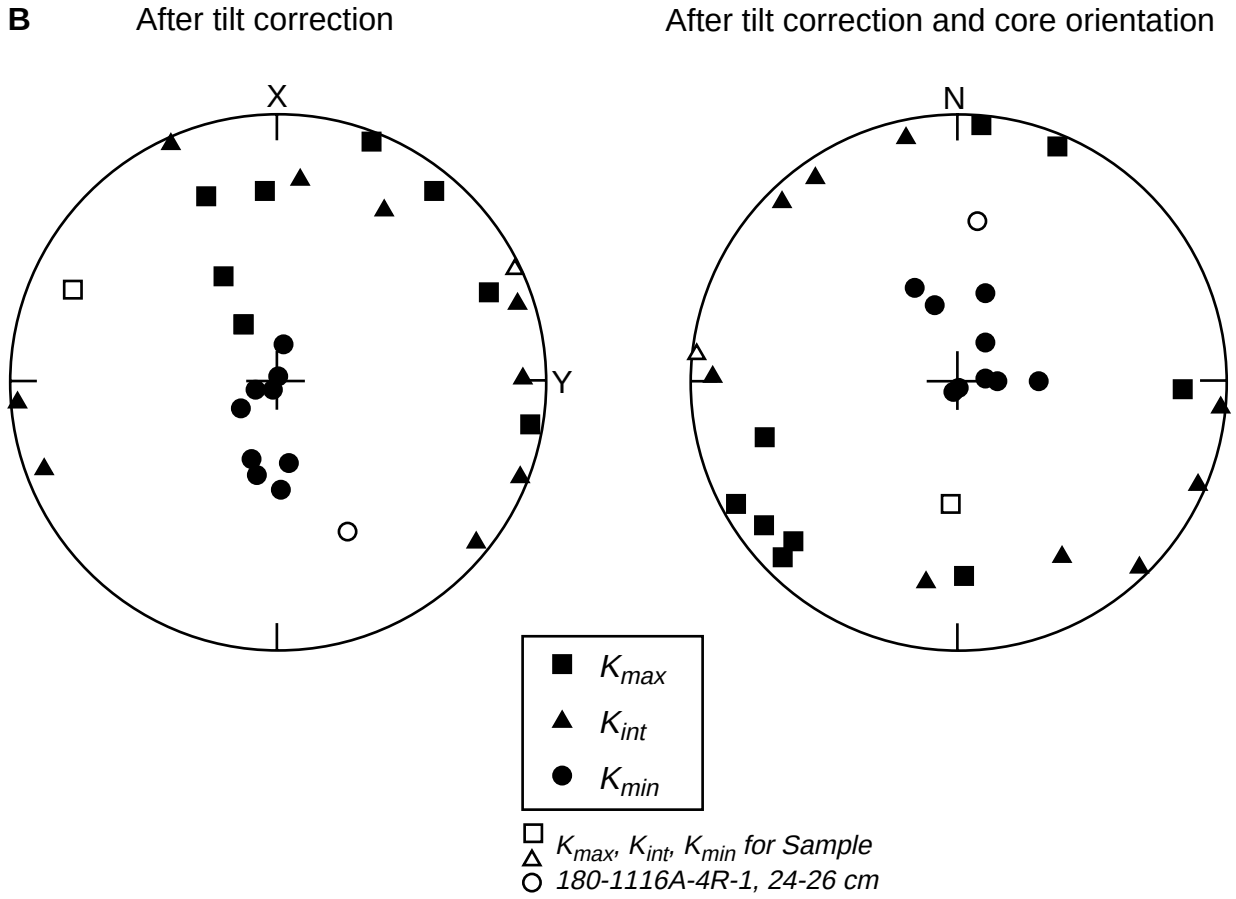

Figure F33. Demagnetization behavior of discrete samples from working halves of core sections. Vector plots: horizontal component = solid circles, vertical component = open circles. Stereonet plots: lower hemisphere = solid circles, upper hemisphere = open circles. **A.** Sample 180-1116A-13R-3, 24-26 cm (102.97–102.99 mbsf). **B.** Sample 180-1116A-18R-1, 15-17 cm (149.46–149.48 mbsf). NRM = natural remanent magnetization; Div. = division; Jo = NRM intensity.

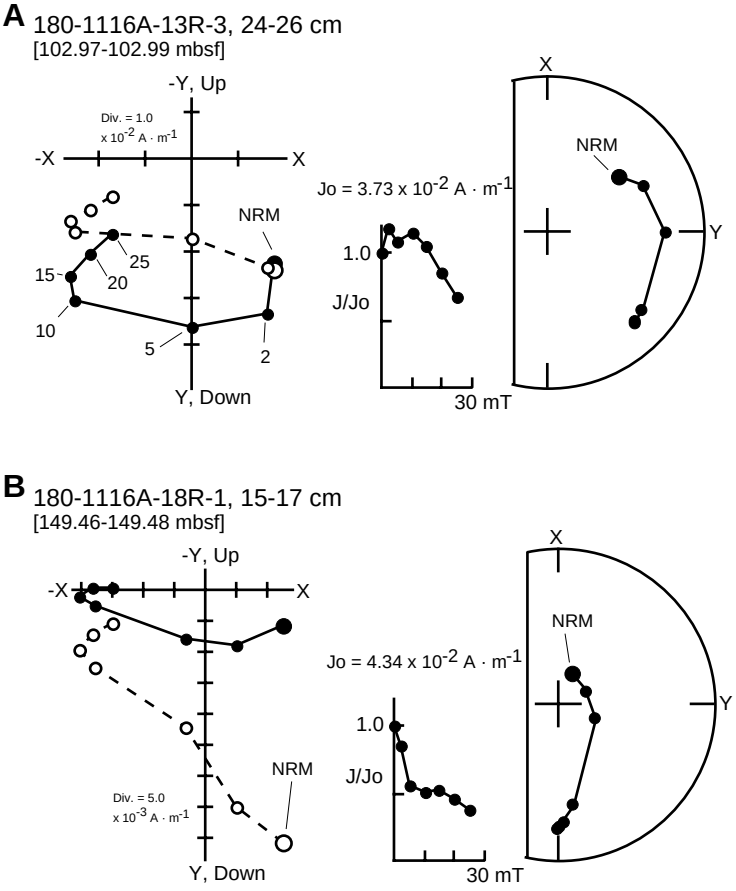

Figure F34. Downhole plots of declination, inclination, and intensity, Hole 1116A. Data from long cores after AF demagnetization at 20 mT are shown as solid circles; data from discrete samples after AF demagnetization at 25 mT are shown as open squares. **A.** Inclinations and declinations are shown uncorrected for bedding tilt. (Continued on next page.)

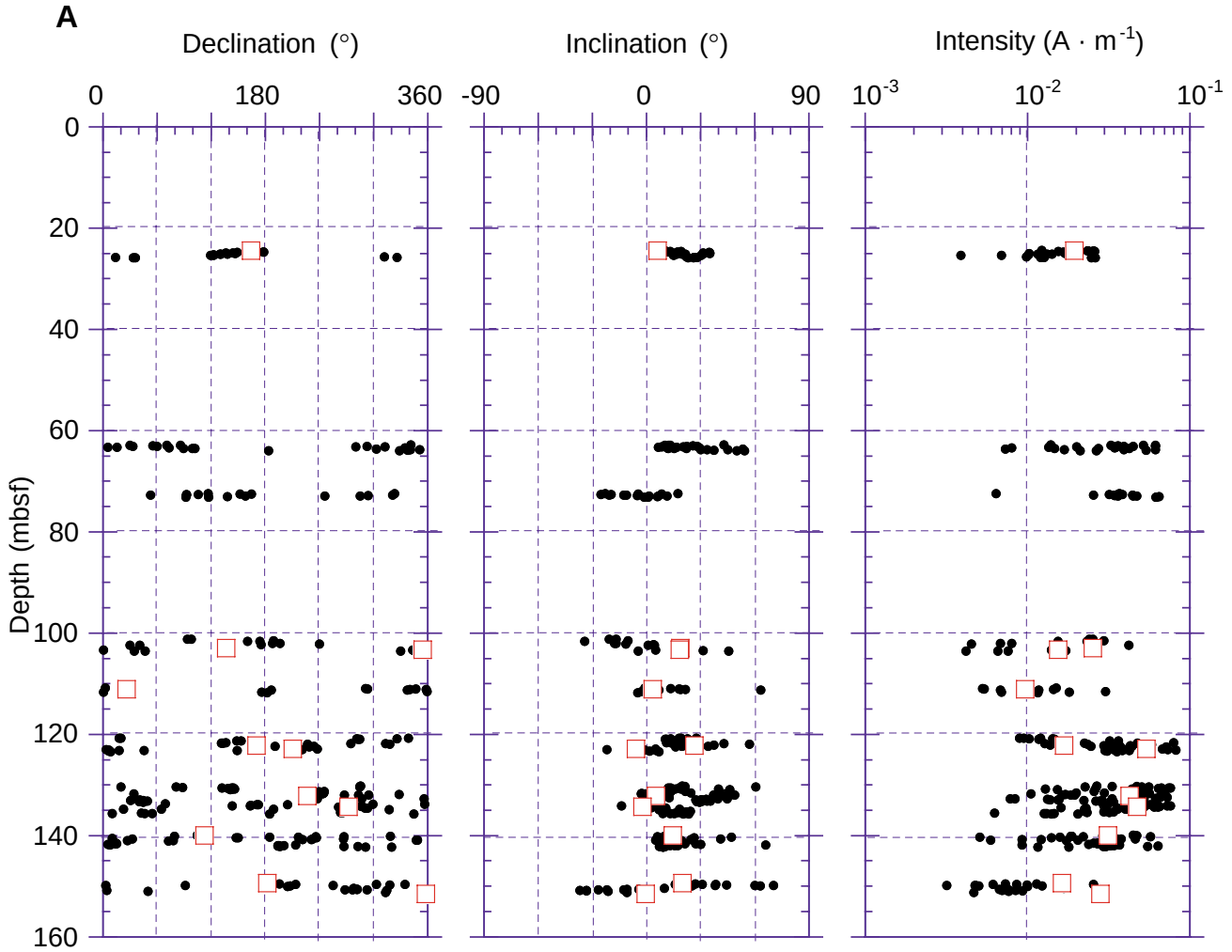

Figure F34 (continued.) B. Inclinations and declinations are shown corrected for bedding tilt.

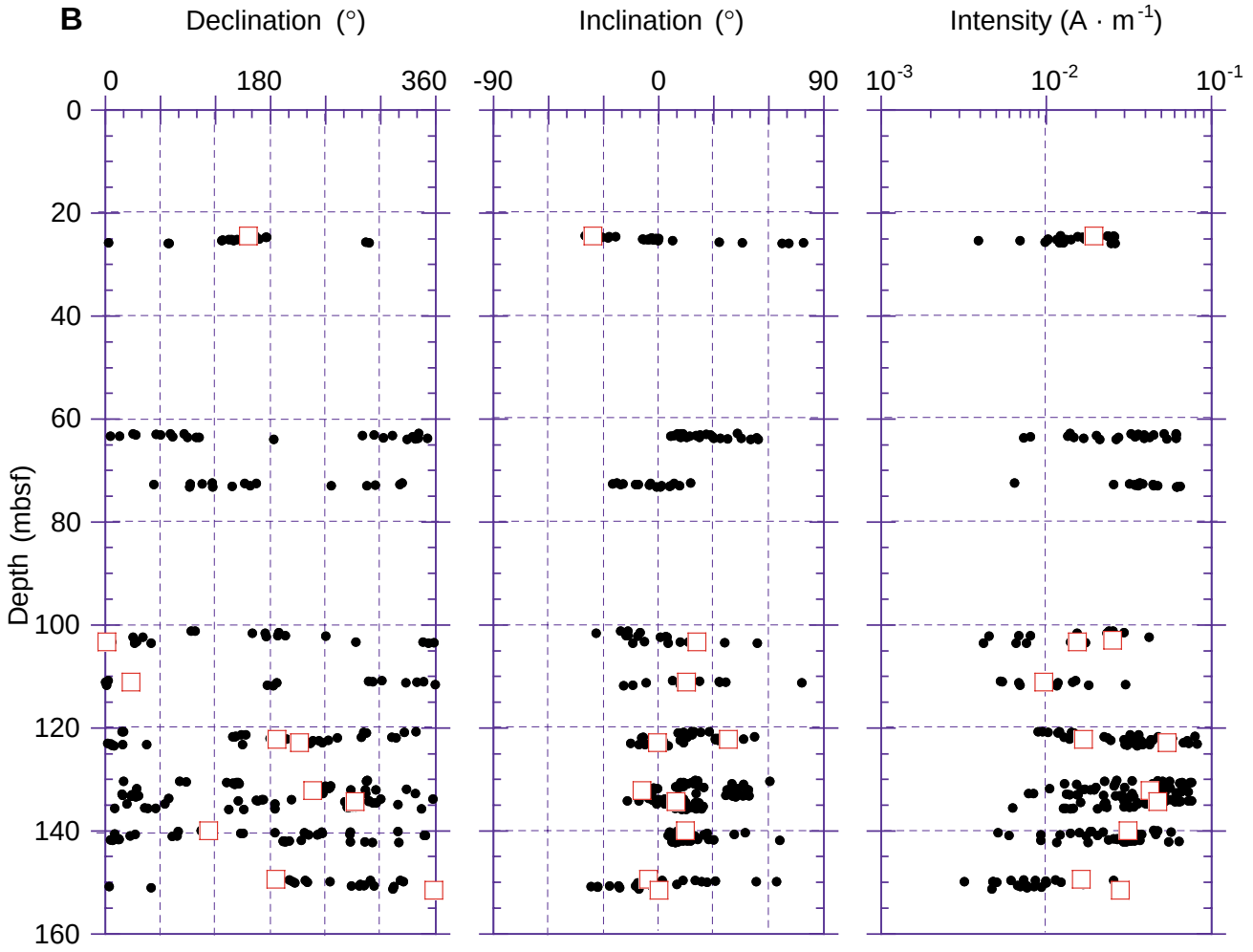

Figure F35. Site 1116 profiles of (**A**) bulk density derived from GRAPE and index property measurements and (**B**) grain density.

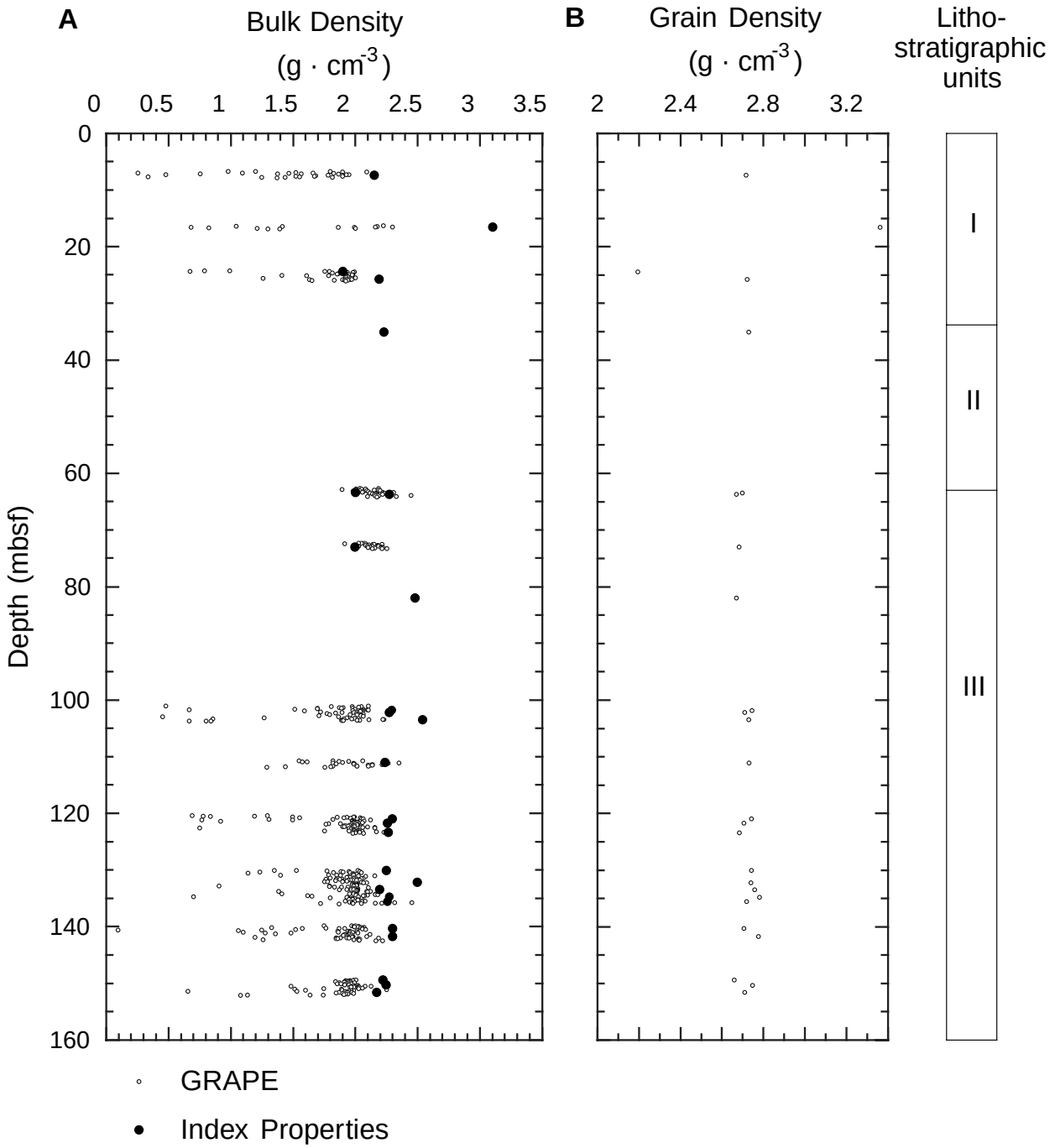

Figure F36. Site 1116 profiles of (**A**) the complete porosity data set and (**B**) the porosity distribution without the carbonate-cemented samples. Superposed is a least-squares exponential curve using the data shown (Φ = porosity; z = depth). The estimated thickness of the removed section is ~960 m. Note that a correlation coefficient (**R**) of 0.3 indicates that the quality of the least-squares regression is poor and that the erosion estimate is preliminary because it is based solely on data from Site 1116.

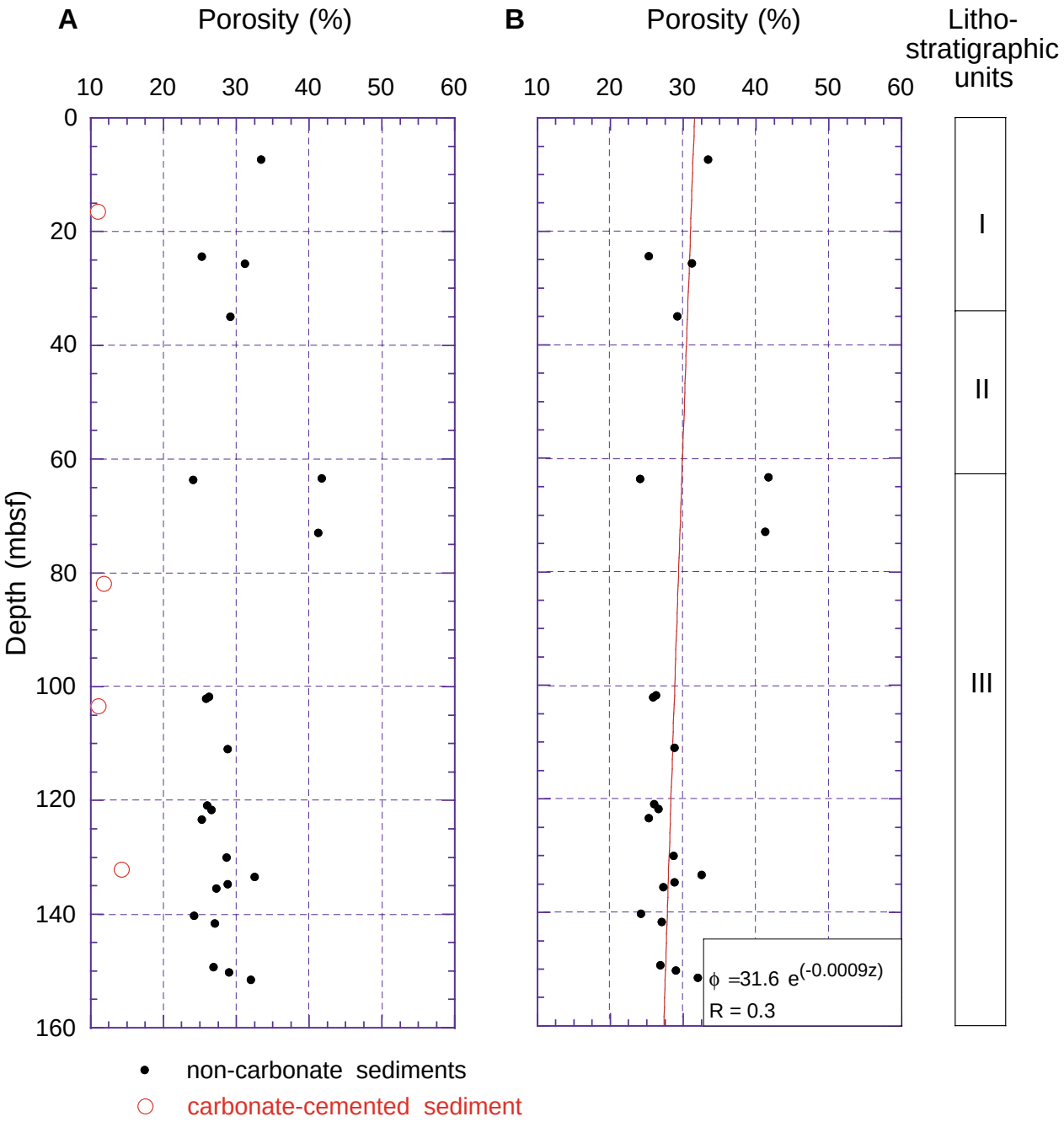

Figure F37. Site 1116 profile of transverse (x and y) and longitudinal (z) velocities. The larger (red) symbols identify the carbonate-cemented samples.

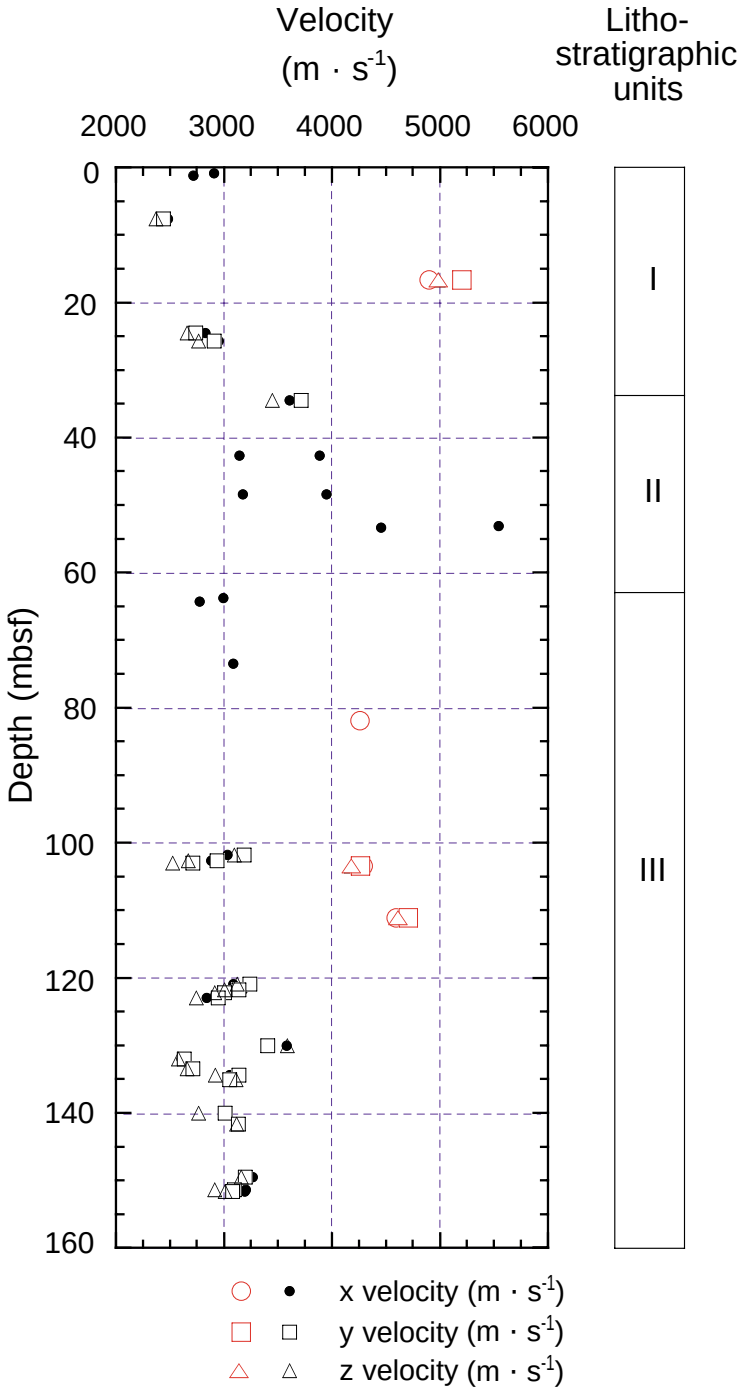

Figure F38. (**A**) Longitudinal velocity vs. the average transverse velocity, and (**B**) *P*-wave anisotropy with depth (see **"Physical Properties,"** p. 28, in the "Explanatory Notes" chapter for method used). A positive anisotropy indicates that the transverse is greater than the longitudinal velocity.

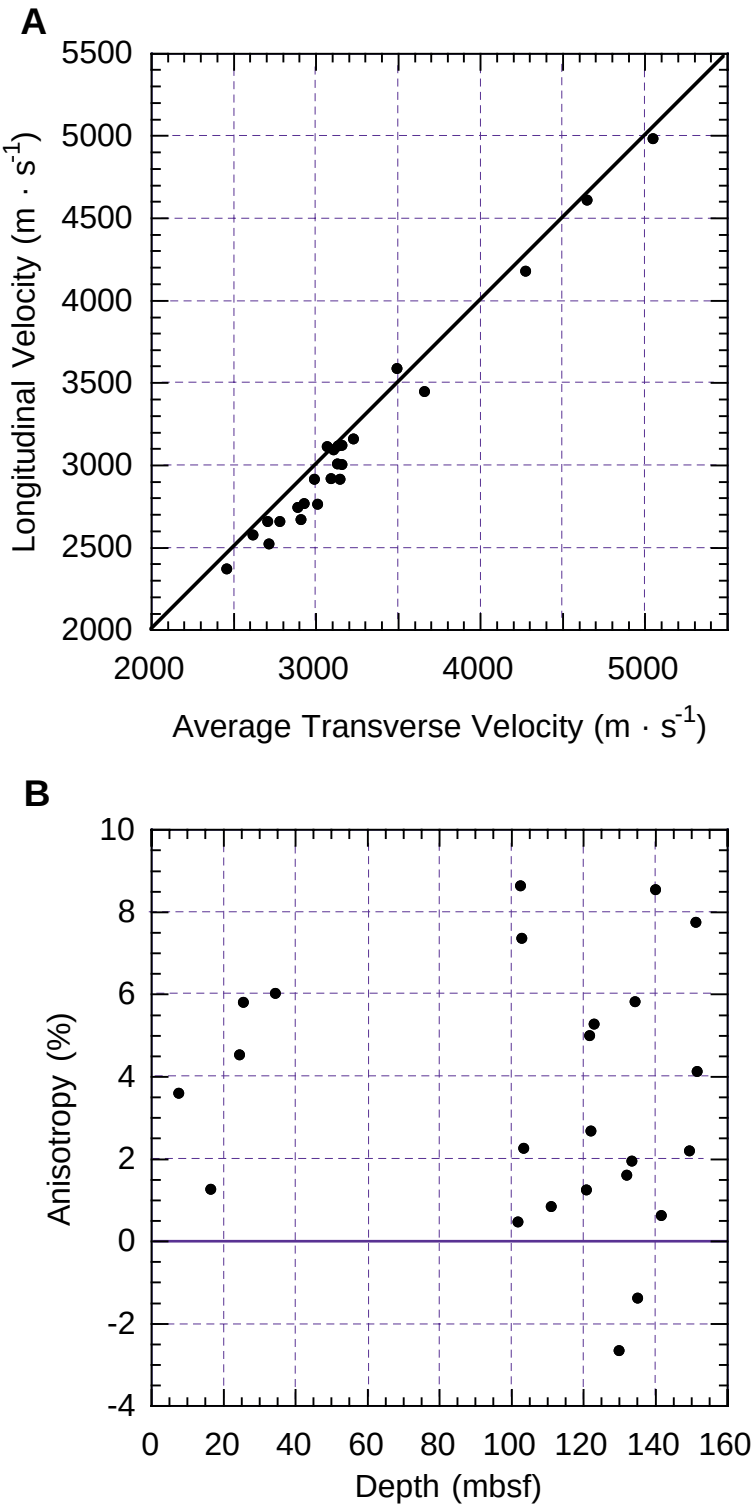

Figure F39. Site 1116 thermal conductivity measurement averages.

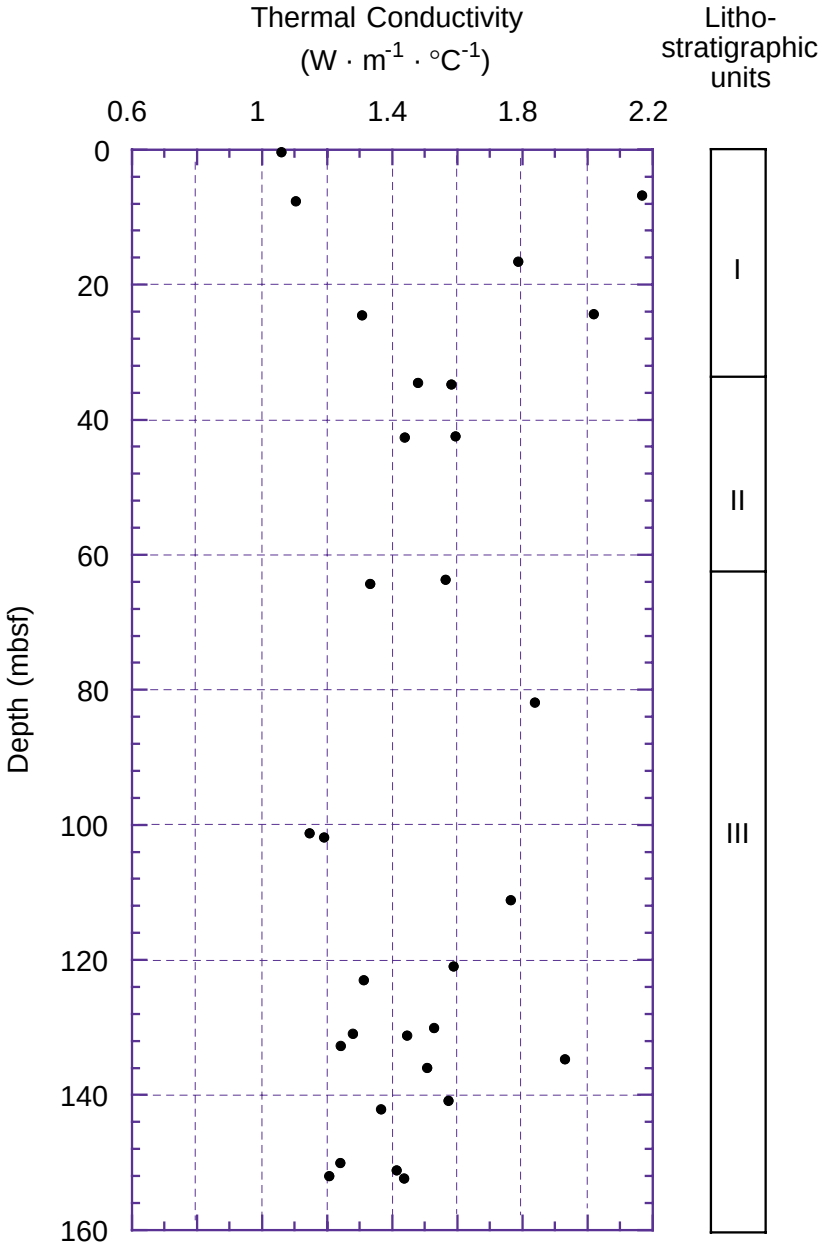

Figure F40. Site 1116 (A) magnetic susceptibility and (B) natural gamma-ray (NGR) data. Examples of the inverse relationship between magnetic susceptibility and NGR are highlighted.

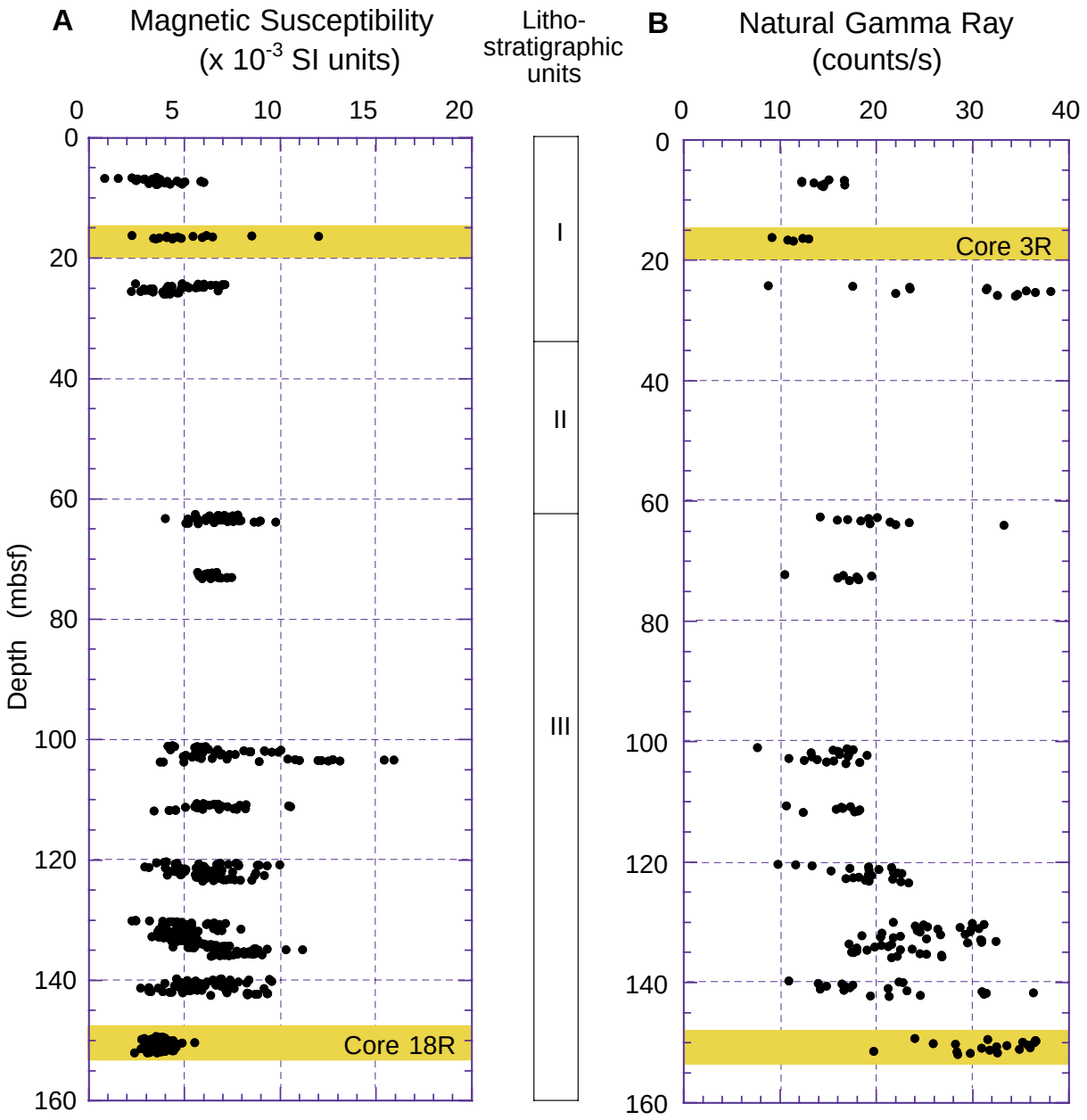

Table T1. Site 1116 coring summary.

Hole 1116A

Latitude: 9°51.934′S
Longitude: 151°34.508′E
Seafloor (drill-pipe measurement from rig floor, mbrf): 1863.00
Distance between rig floor and sea level (m): 11.7
Water depth (drill-pipe measurement from sea level, m): 1851.30
Total depth (from rig floor, mbrf): 2021.90
Total penetration (mbsf): 158.90
Total number of cores: 18
Total length of cored section (m): 158.90
Total core recovered (m): 32.61
Core recovery (%): 21

Core	Date (July 1998)	Time (UTC +10 hr)	Depth (mbsf)	Length cored (m)	Length recovered (m)	Recovery (%)
180-1116A-						
1R	23	2110	0.0-6.6	6.6	0.67	10.2
2R	24	0200	6.6-16.2	9.6	1.49	15.5
3R	24	0515	16.2-24.2	8.0	0.89	11.1
4R	24	0955	24.2-33.8	9.6	2.08	21.7
5R	24	1530	33.8-42.4	8.6	1.35	15.7
6R	24	1830	42.4-48.0	5.6	0.60	10.7
7R	24	2100	48.0-53.0	5.0	0.90	18.0
8R	25	0035	53.0-62.6	9.6	0.39	4.1
9R	25	0255	62.6-72.2	9.6	1.75	18.2
10R	25	0545	72.2-81.8	9.6	1.35	14.1
11R	25	0800	81.8-91.4	9.6	0.21	2.2
12R	25	0935	91.4-101.0	9.6	0.21	2.2
13R	25	1240	101.0-110.6	9.6	3.18	33.1
14R	25	1550	110.6-120.3	9.7	1.53	15.8
15R	25	1845	120.3-130.0	9.7	3.59	37.0
16R	25	2150	130.0-139.7	9.7	6.29	64.9
17R	25	0030	139.7-149.3	9.6	3.00	31.3
18R	26	0430	149.3-158.9	9.6	3.13	32.6
Totals:				158.9	32.61	20.5

Note: UTC = Universal Time Coordinated.

Table T2. Site 1116 coring summary by section. (Continued on next page.)

Core	Date (July 1998)	Time (UTC +10 hr)	Core depth (mbsf) Top	Core depth (mbsf) Bottom	Length (m) Cored	Length (m) Recovered	Recovery (%)	Section	Length (m) Liner	Length (m) Curated	Section depth (mbsf) Top	Section depth (mbsf) Bottom	Catwalk samples	Comment
180-1116A-														
1R	23	2110	0.0	6.6	6.6	0.67	10.2							
								1	0.45	1.31	0.00	1.31	HS, PAL	
								CC	0.22	0.00			PAL	
									0.67	1.31				
2R	24	0200	6.6	16.2	9.6	1.49	15.5							
								1	1.29	1.29	6.60	7.89	HS	
								CC	0.20	0.20	7.89	8.09	PAL	
									1.49	1.49				
3R	24	0515	16.2	24.2	8.0	0.89	11.1							
								1	0.70	0.70	16.20	16.90	HS	
								CC	0.19	0.19	16.90	17.09	PAL	
									0.89	0.89				
4R	24	1055	24.2	33.8	9.6	2.08	21.7							
								1	1.30	1.30	24.20	25.50		
								2	0.55	0.55	25.50	26.05	HS	
								CC	0.23	0.23	26.05	26.28	PAL	Trace to paleontology lab
									2.08	2.08				
5R	24	1530	33.8	42.4	8.6	1.35	15.7							
								1	1.35	1.50	33.80	35.30	PAL, HS	
									1.35	1.50				
6R	24	1830	42.4	48.0	5.6	0.60	10.7							
								1	0.40	0.40	42.40	42.80		
								CC	0.20	0.20	42.80	43.00		
									0.60	0.60				
7R	24	2100	48.0	53.0	5.0	0.90	18.0							
								1	0.62	0.62	48.00	48.62	HS	
								CC	0.28	0.28	48.62	48.90	PAL	
									0.90	0.90				
8R	24	0255	53.0	62.6	9.6	0.39	4.1							
								1	0.39	0.57	53.00	53.57		
									0.39	0.57				
9R	25	0255	62.6	72.2	9.6	1.75	18.2							
								1	1.51	1.51	62.60	64.11	HS	
								CC	0.24	0.24	64.11	64.35	PAL	Trace to paleontology lab
									1.75	1.75				
10R	25	0545	72.2	81.8	9.6	1.35	14.1							
								1	1.12	1.12	72.20	73.32	HS	
								CC	0.23	0.23	73.32	73.55	PAL	
									1.35	1.35				
11R	25	0800	81.8	91.4	9.6	0.21	2.2							
								1	0.21	0.31	81.80	82.11	PAL	Trace to paleontology lab
									0.21	0.31				
12R	25	0935	91.4	101.0	9.6	0.21	2.2							
								1	0.21	0.21	91.40	91.61	PAL, HS	
									0.21	0.21				

Table T2 (continued).

Core	Date (July 1998)	Time (UTC +10 hr)	Core depth (mbsf) Top	Core depth (mbsf) Bottom	Length (m) Cored	Length (m) Recovered	Recovery (%)	Section	Length (m) Liner	Length (m) Curated	Section depth (mbsf) Top	Section depth (mbsf) Bottom	Catwalk samples	Comment
13R	25	1240	101.0	110.6	9.6	3.18	33.1							
								1	0.82	0.82	101.00	101.82	HS	
								2	0.91	0.91	101.82	102.73	IW	
								3	0.31	0.31	102.73	103.04	WRSCR	
								4	0.77	0.77	103.04	103.81		
								CC	0.37	0.37	103.81	104.18	PAL	
									3.18	3.18				
14R	25	1550	110.6	120.3	9.7	1.53	15.8							
								1	1.31	1.31	110.60	111.91	HS	
								CC	0.22	0.22	111.91	112.13	PAL	
									1.53	1.53				
15R	25	1845	120.3	130.0	9.7	3.59	37.0							
								1	1.17	1.17	120.30	121.47	HS	
								2	1.22	1.22	121.47	122.69		
								3	0.86	0.86	122.69	123.55		
								CC	0.34	0.34	123.55	123.89	PAL	
									3.59	3.59				
16R	25	2150	130.0	139.7	9.7	6.29	64.8							
								1	1.08	1.08	130.00	131.08	HS	
								2	1.08	1.08	131.08	132.16		
								3	1.36	1.36	132.16	133.52		
								4	1.50	1.50	133.52	135.02		
								5	1.03	1.03	135.02	136.05		
								CC	0.24	0.24	136.05	136.29	PAL	
									6.29	6.29				
17R	26	0030	139.7	149.3	9.6	3.00	31.3							
								1	1.50	1.50	139.70	141.20		
								2	1.28	1.28	141.20	142.48	HS	
								CC	0.22	0.22	142.48	142.70	PAL	
									3.00	3.00				
18R	26	0430	149.3	158.9	9.6	3.13	32.6							
								1	0.91	0.91	149.30	150.21		
								2	1.15	1.15	150.21	151.36		
								3	0.77	0.77	151.36	152.13	HS	
								CC	0.30	0.30	152.13	152.43	PAL	
									3.13	3.13				
				Totals:	158.9	32.61	20.5							

Note: IW = interstitial water; WRSCR = whole round Screaton; PAL = paleontology; HS = headspace.

Table T3. Results of X-ray diffraction analysis of bulk fine-grained sediments, Site 1116.

Core, section, interval (cm)	Depth (mbsf)	Description	XRD identification: major (minor) minerals
180-1116A-			
1R-1, 106-107	1.06	Claystone	Plagioclase (quartz, calcite, chlorite)
2R-1, 47-49	7.07	Siltstone	Plagioclase, quartz (chlorite, calcite, smectite?, pyroxene, amphibole)
3R-CC, 12-14	17.02	Silty claystone	Plagioclase, quartz, calcite (chlorite, amphibole, smectite?)
4R-1, 39-40	24.59	Siltstone	Plagioclase, quartz (pyroxene, chlorite, smectite?)
4R-CC, 16-17	26.21	Sandstone	Plagioclase, quartz (calcite, chlorite, smectite?, pyroxene)
5R-1, 109-110	34.89	Silty sandstone	Quartz, plagioclase (calcite, pyroxene, chlorite, smectite?)
9R-1, 53.5-56	63.13	Claystone	Plagioclase, quartz (chlorite, smectite?, calcite, pyroxene)
10R-1, 100-102	73.20	Silty claystone	Plagioclase, quartz (calcite, chlorite, smectite?, pyroxene, amphibole)
11R-1, 4-6	81.84	Sandstone	Plagioclase, quartz (chlorite, calcite, smectite?, illite, pyroxene, amphibole)
12R-1, 8-10	91.48	Sandstone	Quartz, plagioclase (calcite, pyroxene, chlorite, smectite?)

Note: See **"Lithostratigraphy,"** p. 4 for discussion.

Table T4. Stratigraphic distribution of planktonic foraminifers, Hole 1116A.

Core, section, interval (cm)	Depth (mbsf)	Abundance	Preservation	*Dentoglobigerina altispira*	*Globigerinella siphonifera*	*Globigerinoides conglobatus*	*Globigerinoides extremus*	*Globigerinoides fistulosus*	*Globigerinoides quadrilobatus*	*Globigerinoides ruber*	*Globigerinoides sacculifer*	*Globigerinoides trilobus*	*Globorotalia crassaformis*	*Globorotalia margaritae*	*Globorotalia menardii*	*Globorotalia tosaensis**	*Globorotalia tumida*	*Neogloboquadrina acostaensis*	*Neogloboquadrina dutertrei*	*Neogloboquadrina humerosa*	*Orbulina universa*	*Pulleniatina obliquiloculata*	*Pulleniatina praecursor*	*Pulleniatina primalis*	*Sphaeroidinella dehiscens*	*Sphaeroidinella dehiscens* s.l.
180-1116A-																										
1R-1, 106-112	1.06	F	M			F				F	R	F					F			F	R	R				
1R-CC, 14-16																										
2R-CC, 16-20	8.05	A	M		R			F	F	R		R	F		F		F		R	A	R	A			F	
3R-CC, 17-19	17.07																									
4R-CC, 22-23	26.27	C	M		F	F	R		F	F	F	F	F		R			A		A	R	A			R	
5R-1, 133-135	35.13	F	M								R	F								F		R			R	
7R-CC, 27-28	48.89	R	P							R								R								
9R-CC, 23-24	64.34	C	P						F			F	R				R			F		R			R	
10R-CC, 20-23	73.52	T	P																							
11R-1, 20-21	82																									
12R-1, 17-21	91.57	R	P				R		R	R		R								F						
13R-CC, 31-33	104.12	C	M			F	F	F	F	F	F	F	R			R	F			F	R		F		F	
14R-CC, 20-22	112.11	F	P				F	R		F		F								F	R				R	
15R-2, 9-10	121.56	A	M	R	F	F		R	A		F	A	F	R			R	F		A	F	A			R	
15R-CC, 31-34	123.86	C	M			R	R			R	F		F				F			F	R			F		R
16R-CC, 9-11	136.14	R	P						R	R							R									
17R-CC, 18-22	142.66	R	P						R			R	R				R								R	

Notes: * = transitional from *Globorotalia crassaformis*. Abundance (number of specimens per field of view): A = abundant (2–9); C = common (lower range of abundant); F = few (0.5–1.0); R = rare (1–3 per tray); T = trace. Preservation: M = moderate; P = poor.

Table T5. Data from discrete sample measurement of remanent magnetization after 25-mT AF demagnetization, Site 1116.

Core, section, interval (cm)	Depth (mbsf)	Declination (°)	Inclination (°)	Intensity ($A \cdot m^{-1}$)
180-1116A-				
4R-1, 24-26	24.45	164.26	6.20	1.95 E–05
13R-3, 24-26	102.98	136.61	18.64	2.53 E–05
13R-4, 33-35	103.38	354.23	18.31	1.54 E–05
14R-1, 52-54	111.13	26.12	3.63	9.63 E–06
15R-2, 72-74	122.20	170.23	26.65	1.68 E–05
16R-3, 6-8	132.23	226.19	5.45	4.23 E–05
16R-4, 86-88	134.39	271.90	–2.34	4.71 E–05
17R-1, 32-34	140.03	112.28	14.56	3.13 E–05
18R-1, 15-17	149.46	181.99	19.84	1.63 E–05
18R-3, 22-24	151.59	358.03	–0.45	2.81 E–05

Table T6. Composition of headspace gas in sediments, Site 1116.

Core, section, interval (cm)	Depth (mbsf)	C_1	n-C_5
180-1116A-			
1R-1, 43-45	0.43	5	
2R-1, 0-2	6.60	3	
3R-1, 0-2	16.20	3	
4R-2, 54-55	26.04	3	
5R-1, 140-141	35.20	1	459
7R-1, 0-2	48.00	1	
9R-1, 0-2	62.60	8	
10R-1, 0-1	72.20	5	
12R-1, 0-1	91.40	6	
13R-1, 0-1	101.00	5	
14R-1, 0-1	110.60	3	
15R-1, 0-1	120.30	6	
16R-1, 0-1	130.00	3	
17R-2, 0-1	141.20	3	
18R-3, 0-1	151.36	3	

Notes: All concentrations are reported in parts per million by volume. Blanks indicate values below detection limit.

Table T7. Calcium carbonate, carbon, nitrogen, and sulfur contents in sediments, Site 1116.

Core, section, interval (cm)	Depth (mbsf)	Inorganic carbon (wt%)	$CaCO_3$ (wt%)	Organic carbon (wt%)	Total nitrogen (wt%)	C/N	Total sulfur (wt%)
180-1116A-							
1R-1, 108-109	1.08	0.39	3.27	0.09			0.14
2R-1, 47-49	7.07	0.36	3.01	0.64	0.01	64	0.24
3R-CC, 12-13	17.02	0.58	4.84	0.45	0.05	9	0.34
4R-1, 39-40	24.59	0.23	1.93	0.33			0.30
4R-CC, 15-16	26.20	0.38	3.21	0.39			0.09
5R-1, 109-110	34.89	0.42	3.53	0.45			0.50
9R-1, 53.5-56	63.13	0.28	2.40	0.84	0.01	84	0.36
10R-1, 100-102	73.20	0.34	2.83	1.03	0.04	26	0.44
11R-1, 4-6	81.84	0.30	2.51	0.99	0.03	33	0.54
12R-1, 8-10	91.48	0.32	2.74	0.71	0.01	71	0.38
13R-1, 65-66	101.65	0.26	2.18	0.65			0.20
14R-1, 115-116	111.75	0.28	2.38	0.71	0.01	71	0.35
15R-2, 104-105	122.51	0.35	2.93	0.56			0.31
16R-4, 45-47	133.97	0.42	3.49	0.72			0.30
17R-2, 85-88	142.05	0.45	3.75	0.43			
18R-1, 78.5-79	150.09	0.37	3.11	0.14			0.28

Note: Blanks indicate values below detection limit, except for C/N ratio where blanks indicate an undefined value.

Table T8. Index properties measured in cores, Site 1116.

Leg	Site	Hole	Core	Type	Section	Top (cm)	Bottom (cm)	Depth (mbsf)	Water content (bulk)	Water content (dry)	Bulk density (g·cm^{-3})	Dry density (g·cm^{-3})	Grain density (g·cm^{-3})	Porosity (%)	Void ratio
180	1116	A	2	R	1	77	79	7.37	15.9	18.9	2.2	1.8	2.7	33.4	0.5
180	1116	A	3	R	1	30	32	16.50	3.6	3.8	3.1	3.0	3.4	11.0	0.1
180	1116	A	4	R	1	19	21	24.39	13.6	15.8	1.9	1.6	2.2	25.3	0.3
180	1116	A	4	R	2	17	19	25.67	14.6	17.1	2.2	1.9	2.7	31.2	0.5
180	1116	A	5	R	1	119	121	34.99	13.4	15.5	2.2	1.9	2.7	29.2	0.4
180	1116	A	9	R	1	80	82	63.40	21.4	27.2	2.0	1.6	2.7	41.7	0.7
180	1116	A	9	R	1	106	108	63.66	10.8	12.2	2.3	2.0	2.7	24.1	0.3
180	1116	A	10	R	1	76	78	72.96	21.2	26.9	2.0	1.6	2.7	41.3	0.7
180	1116	A	11	R	1	10	12	81.90	4.9	5.1	2.5	2.4	2.7	11.8	0.1
180	1116	A	13	R	1	77	79	101.77	11.8	13.3	2.3	2.0	2.7	26.3	0.4
180	1116	A	13	R	2	30	32	102.12	11.7	13.2	2.3	2.0	2.7	25.9	0.3
180	1116	A	13	R	4	40	42	103.44	4.5	4.7	2.5	2.4	2.7	11.1	0.1
180	1116	A	14	R	1	38	40	110.98	13.2	15.2	2.2	1.9	2.7	28.8	0.4
180	1116	A	15	R	1	65	67	120.95	11.6	13.1	2.3	2.0	2.7	26.0	0.4
180	1116	A	15	R	2	27	29	121.74	12.1	13.7	2.3	2.0	2.7	26.6	0.4
180	1116	A	15	R	3	68	70	123.37	11.5	12.9	2.3	2.0	2.7	25.3	0.3
180	1116	A	16	R	1	6	8	130.06	13.0	15.0	2.2	2.0	2.7	28.7	0.4
180	1116	A	16	R	2	105	107	132.13	5.9	6.2	2.5	2.3	2.7	14.3	0.2
180	1116	A	16	R	3	126	128	133.42	15.2	17.9	2.2	1.9	2.8	32.5	0.5
180	1116	A	16	R	4	121	123	134.73	13.0	14.9	2.3	2.0	2.8	28.8	0.4
180	1116	A	16	R	5	51	53	135.53	12.4	14.1	2.3	2.0	2.7	27.3	0.4
180	1116	A	17	R	1	57	59	140.27	10.8	12.1	2.3	2.0	2.7	24.2	0.3
180	1116	A	17	R	2	47	49	141.67	12.1	13.7	2.3	2.0	2.8	27.1	0.4
180	1116	A	18	R	1	4	6	149.34	12.4	14.2	2.2	1.9	2.7	26.9	0.4
180	1116	A	18	R	2	4	6	150.25	13.2	15.2	2.2	1.9	2.7	29.0	0.4
180	1116	A	18	R	3	22	24	151.58	15.1	17.8	2.2	1.8	2.7	32.0	0.5

Note: This table is also available in ASCII format in the **TABLES** directory.

Table T9. Longitudinal (z) and transverse (x and y) velocities for cores, Site 1116.

Leg	Site	Hole	Core	Type	Section	Top (cm)	Bottom (cm)	Depth (mbsf)	x-velocity ($m \cdot s^{-1}$)	y-velocity ($m \cdot s^{-1}$)	z-velocity ($m \cdot s^{-1}$)
180	1116	A	1	R	1	83	83	0.83	2907		
180	1116	A	1	R	1	117	117	1.17	2714		
180	1116	A	2	R	1	97	97	7.57	2478	2436	2370
180	1116	A	3	R	1	38	38	16.58	4894	5199	4983
180	1116	A	4	R	1	25	25	24.45	2824	2736	2657
180	1116	A	4	R	2	14	14	25.64	2952	2907	2765
180	1116	A	5	R	1	67	67	34.47	3608	3713	3446
180	1116	A	6	R	1	23	23	42.63	3140		
180	1116	A	6	R	1	23	23	42.63	3886		
180	1116	A	7	R	1	36	36	48.36	3176		
180	1116	A	7	R	1	36	36	48.36	3945		
180	1116	A	8	R	1	2	2	53.02	5540		
180	1116	A	8	R	1	29	29	53.29	4452		
180	1116	A	9	R	1	108	108	63.68	2993		
180	1116	A	9	R	CC	14	14	64.25	2775		
180	1116	A	10	R	CC	11	11	73.43	3083		
180	1116	A	11	R	1	9	9	81.89	4257		
180	1116	A	13	R	1	81	81	101.81	3033	3184	3093
180	1116	A	13	R	2	81	81	102.63	2884	2933	2667
180	1116	A	13	R	3	25	25	102.98	2720	2709	2522
180	1116	A	13	R	4	34	34	103.38	4287	4260	4178
180	1116	A	14	R	1	53	53	111.13	4592	4703	4608
180	1116	A	15	R	1	61	61	120.91	3080	3236	3118
180	1116	A	15	R	2	73	73	122.2	2976	3004	2911
180	1116	A	15	R	3	29	29	122.98	2838	2943	2742
180	1116	A	15	R	4	25	25	121.72	3175	3138	3003
180	1116	A	16	R	1	3	3	130.03	3578	3404	3585
180	1116	A	16	R	2	94	94	132.02	2602	2631	2575
180	1116	A	16	R	3	131	131	133.47	2707	2710	2657
180	1116	A	16	R	4	86	86	134.38	3050	3136	2918
180	1116	A	16	R	5	5	5	135.07	3084	3053	3111
180	1116	A	17	R	1	32	32	140.02	3007	3010	2762
180	1116	A	17	R	2	43	43	141.63	3137	3132	3115
180	1116	A	18	R	1	16	16	149.46	3263	3196	3159
180	1116	A	18	R	2	112	112	151.33	3199	3096	2913
180	1116	A	18	R	3	24	24	151.6	3187	3079	3007

Note: This table is also available in ASCII format in the **TABLES** directory.

Table T10. Thermal conductivity values in cores, Site 1116. (Continued on next page. See table note.)

Leg	Site	Hole	Core	Type	Section	Top interval (cm)	Bottom interval (cm)	Top depth (mbsf)	Bottom depth (mbsf)	Middle depth (mbsf)	Thermal conductivity ($W \cdot m^{-1} \cdot °C^{-1}$)	Thermal conductivity average ($W \cdot m^{-1} \cdot °C^{-1}$)
180	1116	A	2	R	1	98	99	7.58	7.59	7.59	1.03	
180	1116	A	2	R	1	98	99	7.58	7.59	7.59	1.18	1.10
180	1116	A	3	R	1	40	41	16.60	16.61	16.61	1.84	
180	1116	A	3	R	1	40	41	16.60	16.61	16.61	1.73	1.79
180	1116	A	4	R	1	27	28	24.47	24.48	24.48	1.25	
180	1116	A	4	R	1	27	28	24.47	24.48	24.48	1.37	1.31
180	1116	A	5	R	1	67	68	34.47	34.48	34.48	1.49	
180	1116	A	5	R	1	67	68	34.47	34.48	34.48	1.47	1.48
180	1116	A	6	R	1	6	7	42.46	42.47	42.47	1.60	
180	1116	A	6	R	1	6	7	42.46	42.47	42.47	1.59	1.59
180	1116	A	1	R	1	36	40	0.36	0.40	0.38	1.05	
180	1116	A	1	R	1	36	40	0.36	0.40	0.38	1.07	1.06
180	1116	A	2	R	1	15	20	6.75	6.80	6.78	2.23	
180	1116	A	2	R	1	15	20	6.75	6.80	6.78	2.10	2.17
180	1116	A	4	R	1	10	15	24.30	24.35	24.33	1.87	
180	1116	A	4	R	1	10	15	24.30	24.35	24.33	2.14	
180	1116	A	4	R	1	10	15	24.30	24.35	24.33	1.92	
180	1116	A	4	R	1	10	15	24.30	24.35	24.33	2.14	2.02
180	1116	A	5	R	1	89	94	34.69	34.74	34.72	1.57	
180	1116	A	5	R	1	89	94	34.69	34.74	34.72	1.59	1.58
180	1116	A	6	R	1	16	20	42.56	42.60	42.58	1.50	
180	1116	A	6	R	1	16	20	42.56	42.60	42.58	1.38	1.44
180	1116	A	9	R	1	104	111	63.64	63.71	63.68	2.21	
180	1116	A	9	R	1	104	111	63.64	63.71	63.68	1.56	
180	1116	A	9	R	1	104	111	63.64	63.71	63.68	1.54	
180	1116	A	9	R	1	104	111	63.64	63.71	63.68	1.60	1.56
180	1116	A	9	R	CC	14	19	64.25	64.30	64.28	1.34	
180	1116	A	9	R	CC	14	19	64.25	64.30	64.28	1.33	1.33
180	1116	A	11	R	1	8	13	81.88	81.93	81.91	1.85	
180	1116	A	11	R	1	8	13	81.88	81.93	81.91	1.82	1.84
180	1116	A	13	R	1	20	22	101.20	101.22	101.21	1.18	
180	1116	A	13	R	1	20	22	101.20	101.22	101.21	1.11	1.15
180	1116	A	13	R	1	80	82	101.80	101.82	101.81	1.14	
180	1116	A	13	R	1	80	82	101.80	101.82	101.81	1.24	1.19
180	1116	A	14	R	1	55	56	111.15	111.16	111.16	1.76	
180	1116	A	14	R	1	55	56	111.15	111.16	111.16	1.76	1.76
180	1116	A	15	R	3	31	32	123.00	123.01	123.01	1.31	
180	1116	A	15	R	3	31	32	123.00	123.01	123.01	1.31	1.31
180	1116	A	15	R	1	63	64	120.93	120.94	120.94	1.57	
180	1116	A	15	R	1	63	64	120.93	120.94	120.94	1.61	1.59
180	1116	A	16	R	1	2	10	130.02	130.10	130.06	1.57	
180	1116	A	16	R	1	2	10	130.02	130.10	130.06	1.49	1.53
180	1116	A	16	R	1	87	92	130.87	130.92	130.90	1.27	
180	1116	A	16	R	1	87	92	130.87	130.92	130.90	1.29	1.28
180	1116	A	16	R	2	2	8	131.10	131.16	131.13	1.46	

Table T10 (continued).

Leg	Site	Hole	Core	Type	Section	Top interval (cm)	Bottom interval (cm)	Top depth (mbsf)	Bottom depth (mbsf)	Middle depth (mbsf)	Thermal conductivity ($W \cdot m^{-1} \cdot °C^{-1}$)	Thermal conductivity average ($W \cdot m^{-1} \cdot °C^{-1}$)
180	1116	A	16	R	2	2	8	131.10	131.16	131.13	1.44	
180	1116	A	16	R	2	2	8	131.10	131.16	131.13	1.44	1.45
180	1116	A	16	R	3	56	58	132.72	132.74	132.73	1.21	
180	1116	A	16	R	3	56	58	132.72	132.74	132.73	1.28	1.24
180	1116	A	16	R	4	110	117	134.62	134.69	134.66	1.92	
180	1116	A	16	R	4	110	117	134.62	134.69	134.66	1.94	1.93
180	1116	A	16	R	5	94	98	135.96	136.00	135.98	1.51	
180	1116	A	16	R	5	94	98	135.96	136.00	135.98	1.51	1.51
180	1116	A	17	R	1	114	118	140.84	140.88	140.86	1.60	
180	1116	A	17	R	1	114	118	140.84	140.88	140.86	1.54	
180	1116	A	17	R	1	114	118	140.84	140.88	140.86	1.58	1.57
180	1116	A	17	R	2	88	93	142.08	142.13	142.11	1.33	
180	1116	A	17	R	2	88	93	142.08	142.13	142.11	1.40	1.37
180	1116	A	18	R	1	75	79	150.05	150.09	150.07	1.24	
180	1116	A	18	R	1	75	79	150.05	150.09	150.07	1.24	1.24
180	1116	A	18	R	2	88	97	151.09	151.18	151.14	1.41	
180	1116	A	18	R	2	88	97	151.09	151.18	151.14	1.42	1.41
180	1116	A	18	R	3	65	70	152.01	152.06	152.04	1.27	
180	1116	A	18	R	3	65	70	152.01	152.06	152.04	1.14	1.21
180	1116	A	18	R	CC	23	28	152.36	152.41	152.39	1.46	
180	1116	A	18	R	CC	23	28	152.36	152.41	152.39	1.42	
180	1116	A	18	R	CC	23	28	152.36	152.41	152.39	1.43	1.44

Note: This table is also available in ASCII format in the **TABLES** directory.